2-2017

Line tension and its influence on droplets and particles at surfaces

Bruce M. Law

Sean P. McBride
Marshall University, mcbrides@marshall.edu

Jiang Yong Wang

Haeng Sub Wi

Govind Paneru

See next page for additional authors

Recommended Citation

B.M. Law, S.P. McBride, J.Y. Wang, H.S. Wi, G. Paneru, S. Betelu, B. Ushijima, Y. Takata, B. Flanders, F. Bresme, H. Matsubara. Line tension and its influence on droplets and particles at surfaces. Progress in Surface Science. 92(2017), p. 1-39.

Authors
Bruce M. Law, Sean P. McBride, Jiang Yong Wang, Haeng Sub Wi, Govind Paneru, Santigo Betelu, Baku Ushijima, Youichi Takata, Bret Flanders, Fernando Bresme, Hiroki Matsubara, Takanori Takiue, and Makoto Aratono

Progress in Surface Science 92 (2017) 1–39

Contents lists available at ScienceDirect

Progress in Surface Science

journal homepage: www.elsevier.com/locate/progsurf

Review article

Line tension and its influence on droplets and particles at surfaces

Bruce M. Law [a,*], Sean P. McBride [b,c], Jiang Yong Wang [d], Haeng Sub Wi [e], Govind Paneru [f], Santigo Betelu [g], Baku Ushijima [h], Youichi Takata [i], Bret Flanders [a], Fernando Bresme [j], Hiroki Matsubara [h], Takanori Takiue [h], Makoto Aratono [h]

[a] Department of Physics, Kansas State University, Manhattan, KS 66506-2601, USA
[b] James Franck Institute, University of Chicago, Chicago, IL 60637, USA
[c] Department of Physics and Physical Science, Marshall University, Huntington, WV 25755-2570, USA
[d] Department of Physics, Shantou University, 243 Daxue Rd, Shantou, Guangdong, China
[e] Korea Research Institute of Standards & Science, Taejon 305600, Republic of Korea
[f] Center for Soft and Living Matter, Institute for Basic Science (IBS), Ulsan 44919, Republic of Korea
[g] Department of Mathematics, General Academics Building 435, University of North Texas, 1155 Union Circle #311430, Denton, TX 76203-5017, USA
[h] Department of Chemistry, Faculty of Sciences, Kyushu University, 744 Motooka, Nishi-ku, Fukuoka 819-039, Japan
[i] Department of Chemical and Biological Engineering, National Institute of Technology, Ube College, 2-14-1 Tokiwadai, Ube, Yamaguchi 755-8555, Japan
[j] Department of Chemistry, Imperial College, SW7 2AZ London, United Kingdom

ARTICLE INFO

Article history:

Keywords:
Line tension
Wettability
Interfacial potential
Surface phase transitions
Contact line instability

ABSTRACT

In this review we examine the influence of the line tension τ on droplets and particles at surfaces. The line tension influences the nucleation behavior and contact angle of liquid droplets at both liquid and solid surfaces and alters the attachment energetics of solid particles to liquid surfaces. Many factors, occurring over a wide range of length scales, contribute to the line tension. On atomic scales, atomic rearrangements and reorientations of submolecular components give rise to an atomic line tension contribution τ_{atom} ($\sim$1 nN), which depends on the similarity/dissimilarity of the droplet/particle surface composition compared with the surface upon which it resides. At nanometer length scales, an integration over the van der Waals interfacial potential gives rise to a mesoscale contribution $|\tau_{vdW}| \sim 1$–100 pN while, at millimeter length scales, the gravitational potential provides a gravitational contribution $\tau_{grav} \sim +1$–10 μN. τ_{grav} is always positive, whereas, τ_{vdW} can have either sign. Near wetting, for very small contact angle droplets, a negative line tension may give rise to a contact line instability. We examine these and other issues in this review.

Contents

* Corresponding author.
E-mail address: bmlaw@phys.ksu.edu (B.M. Law).

http://dx.doi.org/10.1016/j.progsurf.2016.12.002
0079-6816/

1. Introduction

Two bulk phases, *i* and *j*, intersect at a surface. This surface possesses an associated surface tension, or, energy per unit area σ_{ij}. Similarly, three bulk phases meet at a line, the three-phase contact line. This contact line possesses an associated line tension, or, energy per unit length τ. In this review we summarize our views on the line tension associated with a three-phase contact line. Thus, the ideas in this review are directly applicable to liquid droplets at a solid (Fig. 1a) or liquid (Fig. 1b) surface, particles at a liquid surface (Fig. 1c), as well as, thin films or foams in contact with a bulk liquid phase (Fig. 1d). The term "line tension" is also used to describe the two-dimensional surface discontinuity for an (insoluble) surface monolayer at a liquid surface [1,2] (Fig. 1e), however, this review is restricted solely to the line tension at three-phase contact lines (Fig. 1a–d).

The line tension plays an important role in governing the statics, dynamics, and stability of numerous soft matter systems. For example, the line tension determines droplet contact angles around fibers [3], at liquid [4], solid [5], and heterogeneous solid [6,7] surfaces, as well as, strongly influencing droplet behavior in the vicinity of wetting transitions [8–12]. When considering surface nucleation [13–17] and vaporization [18] phenomena, line tension contributions should be included. Surface dynamics, such as, droplet spreading [19,20] and droplet fragmentation [21,22] are both influenced by line tension effects. The stability of films [23], foams [24,25], liquid filaments [26,27], spherical droplets [28,29], and nanobubbles [30] are all governed by line tension effects. Line tension contributions are important in determining the depletion interaction between nanoparticles adsorbed at liquid surfaces [31], as well as, nanoparticle adsorption to [32] and deattachment from [33,34] these surfaces. Hence, the line tension plays a role in mineral separation via the flotation process [35].

Despite the importance that the line tension plays in many surface related phenomena, line tension studies have often proven controversial. This controversy stems mainly from discrepancies in the line tension *magnitude* between mean field theories ($|\tau_{theory}| \sim 10^{-12}$–$10^{-10}$ N), computer simulations ($|\tau_{MD}| \sim 10^{-12}$–$10^{-11}$ N), and experimental measurements ($|\tau_{expt}| \sim 10^{-12}$–$10^{-6}$ N) [36,37]. The experimental range for the line tension magnitude is very broad where, although a number of experiments agree with theory and computer simulations, there are many other experiments (usually for large millimeter-sized liquid droplets at surfaces [38]) which differ by many orders of magnitude from mean field theoretical predictions. An added complication, originally pointed out by Gibbs [39], is that the line tension may be of either sign and, in fact, both positive and negative line tensions have been determined via theory, computer simulations, and experiment. Thus, the line tension has sometimes been characterized as being ill-defined, both in magnitude and in sign, where the reliability of many experimental measurements have been called into question. This has led to the rather unfortunate situation where the concept of the line tension is sometimes completely ignored in situations where it plays an important role. The origin of the wide range in experimental line tension magnitudes $|\tau_{expt}|$ is addressed in a number of sections in this review (Sections 2.3,3.1.1,4, and 5).

There are other less contentious controversies in this field, some of which have now been resolved, while others are still generating significant discussion. In the partial wetting region a droplet on a solid surface will possess a finite, non-zero contact angle ($\theta > 0°$) where the three-phase solid-liquid-vapor contact line (Fig. 1a) possesses an associated line tension τ. As a wetting transition is approached (eg. by increasing the temperature) the contact angle θ decreases and becomes equal to zero at and above the wetting transition. The solid surface is now covered by a thick wetting film. Thus, the three-phase contact line disappears at a wetting transition. This disappearance of the three-phase contact line gives rise to many questions. What is the functional behavior of the line tension as the wetting transition is approached? Is the line tension zero, finite, or infinite at the wetting transition? If the line tension is finite at the wetting transition, what is the sign of the line tension? Questions such as these generated significant theoretical discussion where differing groups arrived at differing answers. Much of this debate now appears to have been resolved [8]. The answers depend upon the order of the wetting transition (first or second order), as well as, the range of the surface interactions. These issues, including the origin of the sign of the line tension, will be discussed briefly in Section 2.3.

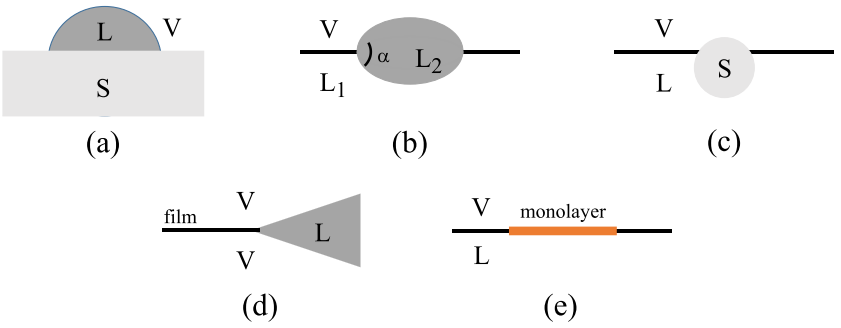

Fig. 1. Examples of three-phase contact lines, possessing line tension τ, where three bulk phases meet: (a) liquid (L) droplet at a solid(S)-vapor(V) surface, (b) liquid droplet at a liquid-vapor surface, (c) solid particle at a liquid-vapor surface, and (d) thin film meeting a bulk liquid phase. Example of a two-dimensional discontinuity: (e) insoluble monolayer at a liquid-vapor surface.

An additional controversy is still ongoing. A number of years ago Clarke [40,41], as well as, Steigmann and Li [28,42] claimed that the three-phase contact line of a liquid droplet would be unstable if this contact line possesses a negative line tension. A number of groups examined this issue theoretically and found, on the contrary, that the three-phase contact line remains stable even for droplets possessing a negative line tension [43,44]. This issue of the contact line stability for droplets possessing a negative line tension has been re-examined recently. The latest findings indicate that such droplets possess regions of stability and instability to contact line fluctuations [26,27,29]. These issues are discussed in more detail in Sections 3.2.2 and 3.2.3.

There have been many excellent reviews of the line tension at three-phase contact lines [36,37,45–49]. The purpose of the current line tension review is multifold:

(a) Provide a pedagogical description of the line tension, aimed at the level of a senior undergraduate student, with sufficient details so that the reader can understand how the theoretical and computer simulation predictions arise (Section 2), which will provide a perspective on their range of validity.
(b) Develop the theory used to deduce the line tension from experimental measurements (Section 3). Thus, the range of validity of the experimental line tension measurements can also be assessed. The experiments considered in this section are taken from our published work where interrelated work, by others, is also discussed. Inevitably the theory for determining the line tension from experimental measurements involves considerations of the equilibrium mechanical energy E of an object at a surface including both surface and line tension terms. Therefore, a governing theme throughout this review that a student should keep in mind is that the equilibrium position of an object is just determined by its minimum mechanical energy. Thus, it is a matter of simple calculus where, for equilibrium, $dE/d\theta = 0$ and $d^2E/d\theta^2 > 0$. Sufficient details are provided in this review so that an undergraduate student can reproduce the results, however, if the calculations are deemed too complicated or tedious, then a broad outline is given and the interested reader is directed to the relevant literature.
(c) With this perspective on the theoretical, computer simulation, and experimental estimates of the line tension it will then be possible to address current topics and controversies within the line tension field including the wide range in experimental line tension magnitudes $|\tau_{expt}| \sim 10^{-12}$–$10^{-6}$ N (Sections 4 and 5), as well as, the conditions under which a negative line tension leads to a three-phase contact line instability (Sections 3.2.2 and 3.2.3).

This review is set out as follows. It is divided into three major sections: Sections 2, 3, and 4. Sections 2 and 3 provide, respectively, a theoretical and experimental perspective on the line tension, in the absence of any gravitational effects. Section 4 considers the issue of large millimeter-sized droplets of order the capillary length, or larger, where gravity will play a role and contribute to the line tension. An important component of this review is our critique and personal assessment of the validity and reliability of each of the line tension measurements (Sections 3.1.3,3.2.3, and 3.3.2). In these critiques, as a service to the reader, we additionally point out what we perceive as misconceptions or errors in the literature. Sec. 5 provides a summary, discussion, and assessment of the line tension at three-phase contact lines.

2. Theoretical perspectives on the line tension

Two length scales play a prominent role in this field:

(i) The capillary length [50]

$$\kappa^{-1} = \sqrt{\frac{\sigma_{LV}}{\rho g}} \sim 1 \text{ mm} \tag{1}$$

where ρ is the liquid density (relative to air if we are considering a liquid droplet on a solid surface in air) while g is the acceleration due to gravity. For small liquid droplets, much less than the capillary length, surface tension effects play the dominant role. Droplets in this regime exhibit a spherical cap shape and, in most cases, gravity can be ignored; however, see Eq. (63) and the associated discussion. For liquid droplets of the order of the capillary length and larger, gravitational effects must always be considered (Section 4).

(ii) The total energy of an object, residing at a surface, is determined by its surface energies σ (an energy per unit area) and its line tension τ (an energy per unit length). Thus, the ratio of these two quantities defines the "line tension length"

$$\xi = |\tau/\sigma| \tag{2}$$

below which the line tension plays a prominent role, and above which the surface tension plays a prominent role. Ascertaining the correct line tension magnitude is therefore very important. If mean field estimates for the line tension are correct ($|\tau_{theory}| \sim 10^{-12}$–$10^{-10}$ N), as the surface tension for many organic liquids is $\sigma \sim 20$ mJ/m^2, then the maximum value for ξ would be

$$\xi_{theory}(\max) \sim 5 \text{ nm} \tag{3}$$

and for most surface phenomena, except at nanometer length scales, one could safely ignore the issue of the line tension. However, if $|\tau| \gg 10^{-10}$ N, as reportedly observed in many experiments, then ξ could be considerably larger. This reasoning is strictly valid only far from a wetting transition. Near a wetting transition (eg. a liquid wetting a solid surface), one must compare the solid/vapor surface, of surface energy σ_{SV}, with the same surface when covered by a (macroscopic) liquid layer, of surface energy $\sigma_{SL} + \sigma_{LV}$. The relevant quantity to consider is, therefore, the spreading coefficient defined as

$$S = \sigma_{SV} - (\sigma_{SL} + \sigma_{LV}), \tag{4}$$

where, in the partial wetting regime, $S < 0$. The spreading coefficient S should be compared with the line tension τ because what is of interest is "Does the line tension assist in advancing this (partially wetting) droplet across the solid surface?" For very large droplets (i.e. in the absence of line tension effects) the macroscopic droplet contact θ_∞ is determined by Young's equation [51]

$$\cos\theta_\infty = \frac{\sigma_{SV} - \sigma_{SL}}{\sigma_{LV}} \tag{5a}$$

$$= 1 + \frac{S}{\sigma_{LV}} \tag{5b}$$

where Eq. (4) has been used in deducing Eq. (5b). Hence, the relevant length scale should be the spreading pressure line tension length [40]

$$\xi_S = \left|\frac{\tau}{S}\right| = \left|\frac{\tau}{\sigma_{LV}(\cos\theta_\infty - 1)}\right|. \tag{6}$$

See Eq. (75) and the accompanying discussion. Near a wetting transition ξ_S can become very large, for example, if $\theta_\infty = 1^\circ$ then $\xi_S \sim 50$ μm and line tension effects are very important near wetting transitions.

A comment on notation. θ_∞ represents the contact angle of a *macroscopic* droplet determined by the surface energies σ_{ij}, as described by Young's equation [Eq. (5a)]. By contrast, θ describes the contact angle of a *finite-sized* object of line tension τ at a surface. θ differs from θ_∞ due to the presence of the line tension τ and due to the object's finite-size. The dependence of θ on line tension τ and object size is described by the modified Young's equation. For example, the modified Young's equation for a spherical particle at a liquid surface [derived later in Eq. (29)] is

$$\cos\theta = \cos\theta_\infty[1 - \tau/b\sigma_{LV}]^{-1}, \tag{7a}$$

whereas, the modified Young's equation for a liquid droplet at a solid surface [derived in Eq. (56a)] is

$$\cos\theta = \cos\theta_\infty - \frac{\tau}{\sigma_{LV} r}. \tag{7b}$$

In these equations b and r are, respectively, the lateral radius of the particle and droplet defined in Sections 3.1.1 and 3.2.1. These modified Young's equations [Eqs. (7a) and (7b)] help to clarify the difference between θ and θ_∞. One readily observes that in the limit that either $\tau \to 0$ or the object becomes infinitely large ($b \to \infty$ or $r \to \infty$) then $\theta \to \theta_\infty$.

2.1. Theoretical and computer simulation estimates for the line tension magnitude

Many different groups have theoretically estimated the magnitude and sign of the line tension for a variety of the configurations depicted in Fig. 1. For example, De Feijter and Vrij [52], as well as, Rowlinson and Widom [53] (RW) have estimated the line tension for a soap film (or Newton black film) of thickness s in contact with a bulk liquid phase (Fig. 1d). For symmetric systems where the two vapor phases are equal ($V1 = V2$) then RW demonstrate that the line tension is negative, which is the same sign determined by de Feijter and Vrij. If the system is asymmetric ($V1 \neq V2$) then the line tension may be positive. In the RW calculation the line magnitude $|\tau| \sim \sigma s$ where σ is the surface tension and, therefore, for a Plateau border

$|\tau| \sim 10^{-12}$ to 10^{-10} N. Getta and Dietrich [54] and Koch, Dietrich and Napiórkowski [55] have used mean field microscopic Density Functional Theory to study the line tension of liquid films at, respectively, homogeneous and chemical structured substrates where they have taken into account the interactions between the fluid and the substrate. They find that $|\tau| \sim \varepsilon/\sum \sim 10^{-11}$ N where ε and $\sum$ are, respectively, the interaction strength and well depth. The Density Functional Theory approach has also been used to calculate line tensions for electrolytic solutions adsorbed on solid substrates. The line tensions are of order 1 pN and increase with the ionic strength of the solution [56]. The small values for the line tension are consistent with the estimates from dimensional analysis, where $\tau \sim \frac{k_B T}{a} = 10^{-11} N$ [53], with a being an atomic length scale ~0.1 nm. Such small values are expected for simple fluids far from critical conditions.

Computer simulations of 1–5 nm diameter spherical colloidal particles at either a liquid-vapor [57,58] or liquid-liquid [59] interface determined line tension magnitudes of $|\tau| \sim 10^{-12}$ to 10^{-11} N in agreement with these theoretical estimates. Negative line tensions were observed at the liquid-vapor surface, whereas, at the liquid-liquid surface negative (positive) line tensions were observed for the smallest (largest) particles. In these early computer simulations, colloidal particles were represented by structureless spheres possessing a diameter as well as a Lennard-Jones interaction potential between the fluid molecules and the colloidal sphere. The line tension of nanoparticles at interfaces can also be estimated from an analysis of the depletion forces of particle pairs adsorbed at fluid interfaces. This approach predicts line tensions that agree in sign and magnitude with those extracted from the analysis of single particles [31]. In a later computer simulation [60], a colloidal particle at the air-water surface was represented by a more realistic all atom simulation where the gold core was surrounded by a passivating alkyl-like ligand shell. The ligand shell deformed at the interface. Line tension estimates were not attempted in this later simulation. The line tension of nanodroplets adsorbed on solid substrates has also been considered in the context of computer simulations [61–64]. These simulations focused on simple fluids modeled using the Lennard-Jones potential. Computation of the line tension involved simulation of spherical and cylindrical droplets possessing different curvatures. It has been observed that the spherical droplets feature a linear dependence with curvature, consistent with the corrected Young's equation predictions, while such dependence is not observed, as would be expected, for cylindrical droplets. The line tensions obtained from this simulation analysis vary in the range 1–10 pN, are negative and depend upon the wettability of the substrate [61]. These observations are broadly consistent with those inferred from simulations of nanoparticles [57–59]. The line tension magnitude is also consistent with the estimates of Density Functional Theory [61] using the sharp kink approximation [54]. Very large values of the line tension in the range 10–100 pN (positive) have been reported for water droplets adsorbed on graphite [65–67]. In one of these studies it has been shown that quantum nuclear degrees of freedom do not influence the value of the contact angle [67].

The line tension has also been computed using Monte Carlo simulations [68,69], which can also provide a direct route to the free energy, and hence do not rely on computations of the contact angle. This approach has been applied to the calculation of the line tension for models of ternary mixtures [68], as well as, for the Ising model [69]. For the ternary mixtures negative line tensions of $\frac{\tau a}{k_B T} \sim -0.1$ were obtained. For atomic length scales of 0.1 nm and a temperature $T \sim 300$ K, this value corresponds to line tensions of the order of pN.

Overall, theoretical and computational approaches predict line tension values that fit broadly in the interval 1–10 pN. Both positive and negative values have been reported. The estimates of water-graphite are on the higher side, and values of up to 100 pN have been reported. The origin of these very large values warrant further investigation.

2.2. Wetting and phase diagrams

In order to better understand both the sign of the line tension and its variation with temperature in the vicinity of a surface phase transition, it is necessary to describe wetting phenomena and how wetting is influenced by the interfacial potential. We begin by considering a liquid droplet L in the partial wetting region on a molecularly smooth and homogeneous substrate S in vapor phase V (Fig. 2a). This droplet, of lateral radius r, makes a contact angle θ with the solid substrate. If this droplet is sufficiently large (i.e. r large but less than the capillary length $\kappa^{-1} \sim 1$ mm, so that gravitational effects can be ignored) the contact angle is determined to a good approximation solely by surface energy effects and θ is now denoted by θ_∞ (the macroscopic contact angle). By balancing the forces per unit length (or surface energies) along the substrate, one obtains Young's equation [Eq. (5a)], which relates θ_∞ to the surface energies σ_{ij} between adjacent phases i and j. Alternatively, θ_∞ can be expressed in terms of the spreading coefficient S as given in Eq. (5b). The spreading coefficient compares the surface energy difference between the solid substrate in contact with a vapor phase (of surface energy σ_{SV}) and the same substrate covered by a macroscopic liquid layer (of surface energy $\sigma_{SL} + \sigma_{LV}$). In the partial wetting regime $\sigma_{SV} < \sigma_{SL} + \sigma_{LV}$, hence, $S < 0$ and the droplet possesses a finite, non-zero contact angle with the solid substrate ($\theta_\infty > 0$).

As the droplet radius r decreases, the line tension τ associated with the three-phase solid-liquid-vapor contact line of circumference $2\pi r$ must become more important and cause the contact angle θ to deviate from its macroscopic value θ_∞, as described by the modified Young's equation [Eq. (7b)]. In the partial wetting regime where $\theta_\infty < 90°$, a positive (negative) line tension tends to decrease (increase) the size of the droplet circumference in order to minimize the total droplet energy, hence, the contact angle θ will increase above (decrease below) θ_∞ for a non-zero line tension. In the partial drying regime, where $\theta_\infty > 90°$, analogous considerations apply.

In order to estimate the line tension theoretically, the microscopic surface structure and surface interactions in the immediate vicinity of the three-phase contact line must be taken into account. One can idealize the three-phase solid-liquid-vapor

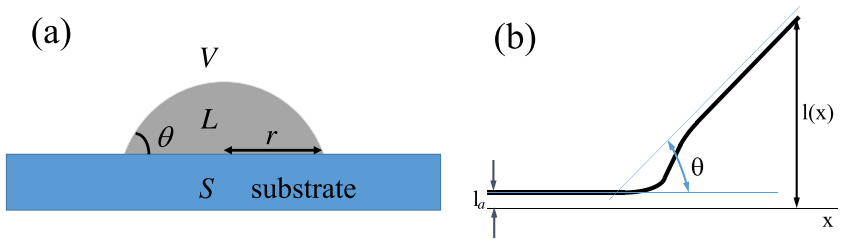

Fig. 2. (a) Liquid droplet (L) of lateral radius r and contact angle θ at a substrate (S) – vapor (V) surface. (b) In the immediate vicinity of the three-phase SLV contact line, the liquid thickness $l(x)$ varies with distance x along the substrate, from an adsorption thickness l_a on the vapor side ($x \ll 0$), to a "liquid wedge" of contact angle θ and thickness variation $l(x)$ on the liquid side ($x \gg 0$).

contact line as consisting of a liquid wedge which makes an angle θ with the solid substrate, as shown in Fig. 2b, where we assume that the three-phase contact line is situated in the vicinity of the origin $x = 0$. The thickness of the liquid layer on the solid substrate $l(x)$ will therefore be a function of distance x where, well away from the liquid droplet ($x \to -\infty$) the solid substrate is covered by an adsorbed film of thickness l_a and surface energy σ_{SV}. Within the macroscopic liquid droplet ($x \to +\infty$), the film thickness approaches a thick liquid wedge possessing a contact angle θ and surface energy $\sigma_{SL} + \sigma_{LV}$ for sufficiently large film thicknesses ($l \gg 100$ nm). At intermediate values of the liquid film thickness ($l_a < l < 100$ nm) the surface energy [or surface interaction potential $V(l)$] is determined by the long range and short range forces that act upon the liquid film of thickness l. The forces that are present in a system are determined by the molecular constituents of the liquid, solid, and vapor phases. The interfacial potential $V(l)$ takes the following approximate form

$$V(l) \sim \sigma_{SV}[1 + (l - l_a)^2], \quad l \sim l_a \tag{8a}$$

$$\sim V_{vdW}(l) + V_C(l) + V_{cx}(l) + \sigma_{SL} + \sigma_{LV}, \quad l >> l_a. \tag{8b}$$

At small $l \sim l_a$, we assume a harmonic potential for $V(l)$ [Eq. (8a)]. At larger l [Eq. (8b)], numerous terms may contribute to $V(l)$, depending upon the circumstance, including the van der Waals V_{vdW}, screened Coulombic V_C, and off-coexistence V_{cx} surface potentials. We briefly describe each of these terms and when they are applicable. The surface energies $\sigma_{SL} + \sigma_{LV}$ are always present in Eq. (8b) if a mesoscopic liquid layer covers the solid substrate. The van der Waals surface potential $V_{vdW}(l)$ arises from an integration over pair interactions between molecules in the wetting layer, solid substrate, and vapor phase. Pairs of molecules experience a van der Waals interaction, due to fluctuating dipole moments, where the van der Waals force between two molecules varies as $\sim 1/d^6$ at small separations d and $\sim 1/d^7$ at large d where the finite speed of light has been accounted for. These force laws at small and large d give rise to, respectively, the non-retarded [Eq. (9a)] and retarded [Eq. (9b)] van der Waals potential $V_{vdW}(l)$ which have the approximate forms [70]

$$V_{vdW}(l) \sim \frac{A}{l^2}, \quad l \sim 10 \text{ nm} \tag{9a}$$

$$\sim \frac{B}{l^3}, \quad l > 50 \text{ nm}. \tag{9b}$$

Eq. (9b) takes into account the "retardation" experienced by the dispersion forces due to the finite speed of light. In many situations, seen in practice, it is sufficient to assume a non-retarded van der Waals potential [Eq. (9a)] where the Hamaker constant A can be approximated as the sum of a zero frequency $A_{v=0}$ and an optical frequency $A_{v>0}$ contribution [70]

$$A \approx A_{v=0} + A_{v>0} \tag{10}$$

$$A_{v=0} \sim -(\varepsilon_L - \varepsilon_V)(\varepsilon_L - \varepsilon_S)k_BT \tag{11a}$$

$$A_{v>0} \sim -(n_L^2 - n_V^2)(n_L^2 - n_S^2)h\nu_e \tag{11b}$$

where ε_i (n_i) is the static dielectric constant (optical refractive index) of phase i, k_BT is the thermal energy and $h\nu_e$ a characteristic electronic excitation energy at frequency ν_e. The zero frequency term is only important for highly polar components (eg. water). In many cases, $A_{v=0}$ can be neglected and the Hamaker constant is therefore determined by the optical refractive indices of the various components.

Eq. (9) represents only an approximation for the complete van der Waals or dispersion potential. The dispersion potential should, in reality, be described by the Dzyaloshinskii-Lifshitz-Pitaevskii (DLP) theory for dispersion interactions [71], which takes into account the summation over the frequency dependent dielectric constant of the liquid layer (of thickness l), sub-

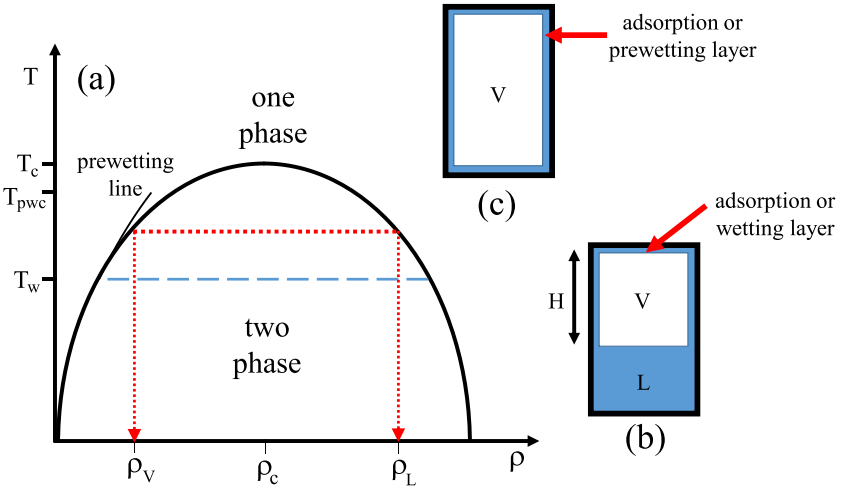

Fig. 3. (a) Liquid-vapor phase diagram where the coexistence curve (heavy solid line) separates the two-phase region from the one-phase region. At a given temperature (horizontal red dotted line), the two vertical red dotted lines determine the liquid (ρ_L) and vapor (ρ_V) densities. As the temperature is increased towards the critical temperature T_c, ρ_V and ρ_L approach each other and become identical and equal to the critical density ρ_c at T_c. The critical point (ρ_c,T_c) therefore represents a second-order phase transition where one can pass continuously from the two-phase region into the one-phase region. For any other point on the coexistence curve, the system undergoes a first-order phase transition in passing from the two-phase region into the one-phase region. The horizontal blue dashed line corresponds to the wetting temperature T_w, below (above) which a macroscopic droplet of contact angle θ_∞ on a solid substrate is greater than (equal to) zero. In the one-phase region a prewetting line (light solid line) joins onto the coexistence curve at T_w. The prewetting line terminates at a prewetting critical point at the prewetting critical temperature T_{pwc}. (b) Two-phase system, below the coexistence curve, with liquid (L) and vapor (V) phases of densities ρ_L and ρ_V in coexistence. The interfacial potential $V(l)$ may stabilize an adsorption or wetting layer on the container walls at height H. (c) One-phase system, above the coexistence curve, at low density (i.e. vapor phase). The interfacial potential $V(l)$ may stabilize an adsorption or prewetting layer on the container walls, as described in the text. (For interpretation of the references to color in this figure legend, the reader is referred to the web version of this article.)

strate, and vapor phase. A good description of the approximate theory, as given in Eqs. (9)–(11), can be found in the well-known book by Israelachvili [70]. A simple and clear description of the DLP theory, along with a description of how to calculate this interaction from experimental dielectric data, can be found in Hough and White [72].

The van der Waals surface potential V_{vdW} is always present in Eq. (8b) for finite l, whereas, the other terms (V_C and V_{cx}) may or may not be present depending upon the circumstance. The screened Coulombic potential $V_C(l)$ is only present for ionized systems, for example, in electrolytic solutions or for surfaces which have undergone surface dissociation [70]. $V_C(l)$ possesses the approximate form of a Yukawa potential,

$$V_C(l) \sim \sigma_o \exp(-l/l_C) \tag{12}$$

where σ_o is a constant that measures the interaction strength. This potential is sometimes called a short-ranged potential because of its exponential decay over a screening length l_C.

A number of different physical processes can remove the substrate liquid layer (of thickness l) away from bulk two-phase coexistence, in which case, the off-coexistence term $V_{cx}(l)$ in Eq. (8b) will be non-zero. In order to obtain a better physical understanding of this statement, we first discuss two-phase liquid-vapor coexistence. Fig. 3a depicts a typical liquid-vapor phase diagram. The heavy solid black line represents the two-phase coexistence curve, which separates the one-phase region from the two-phase region. In the two-phase region (below the coexistence curve), at a particular temperature T (horizontal red dotted line), the two vertical red dotted lines determine the liquid (ρ_L) and vapor (ρ_V) densities, which are in coexistence (Fig. 3b). Above the coexistence curve, in the one-phase region, only a single vapor or liquid phase exists (Fig. 3c). On this phase diagram ρ_c and T_c represent the critical density and critical temperature, respectively; the liquid and vapor phases are indistinguishable at this critical point. If the system is prepared at the critical density ρ_c one can pass continuously from the two-phase region into the one-phase region (i.e. via a second-order phase transition). For any point, other than (ρ_c,T_c), on the coexistence curve the system undergoes a first-order phase transition, with its associated latent heat, in passing from the two-phase region into the one-phase region. The precise shape of the coexistence curve, especially in the vicinity of the critical point (ρ_c,T_c), is a complex topic which will not be discussed here and interested readers should consult other sources [73]. The presence of an interfacial potential $V(l)$ may stabilize an adsorption or wetting (Fig. 3b)/prewetting (Fig. 3c) layer on the container walls.

Whenever a liquid layer on a substrate (or container wall) is removed from bulk liquid coexistence the off-coexistence term

$$V_{cx}(l) = \Delta\mu l \tag{13}$$

will be non-zero. Here $\Delta\mu = \mu - \mu_{cx}$ is the difference in chemical potentials (an energy per unit volume) between the liquid layer (μ) and bulk liquid (μ_{cx}). $\Delta\mu$ can take many different forms.

(i) For example, in Fig. 3b, the system is in two-phase coexistence where the bulk liquid and vapor phases are in equilibrium. At height H the van der Waals attraction has caused a liquid layer to form on the container wall. The chemical potential (μ) of this liquid layer differs from the chemical potential of the bulk liquid (μ_{cx}) due to an additional gravitational potential energy where

$$\Delta\mu \equiv \Delta\mu_{grav} = \Delta\rho g H \tag{14a}$$

and the density difference $\Delta\rho = \rho_L - \rho_V$.

(ii) In Fig. 3c, we consider a situation in the one-phase region (above the coexistence curve) in the vapor phase at fixed temperature T. The liquid phase is not a stable bulk phase. The system has been removed from bulk liquid-vapor coexistence by the vapor pressure p relative to the saturated vapor pressure p_{sat}. (At p_{sat}, vapor condenses to a bulk liquid.) For this situation

$$\Delta\mu \equiv \Delta\mu_p = -\frac{k_B T}{v}\log_{10}\left(\frac{p}{p_{sat}}\right). \tag{14b}$$

where v is the liquid phase molecular volume. As depicted in Fig. 3c an adsorbed layer or a pre-wetting layer may form on the container walls, in the one phase region, due to the interfacial potential $V(l)$ as discussed below.

(iii) In Fig. 3b and c we have assumed that the system is at constant temperature T. There are practical difficulties in achieving a constant temperature throughout a system. For example, in configuration Fig. 3b there may exist an intentional or unintentional temperature difference $\Delta T = T - T(bulk)$ between the wetting layer and the bulk liquid phase. If $\Delta T > 0$ this temperature difference thins the wetting layer and contributes to the chemical potential difference [74,75]

$$\Delta\mu \equiv \Delta\mu_{grav} + \Delta\mu_T = \Delta\rho g H + \frac{n\Delta T L}{T} \approx \frac{n\Delta T L}{T} \tag{14c}$$

where L is the latent heat per molecule, and n is the number density of molecules in the wetting layer. In most practical cases $\Delta\mu_T$ dominates $\Delta\mu_{grav}$. For example, for $\Delta\mu_{grav} \gg \Delta\mu_T$ we require that $\Delta T \ll 10^{-4}$ °C where we have assumed that $\Delta\rho = 1$ g/cm^3, $H = 1$ cm, $T = 300$ K, $L = 5 \times 10^{-20}$ J/molecule and $n = 5.5 \times 10^{27}$ molecules/m^3. This level of temperature uniformity (0.1 mK/cm) is extremely difficult to achieve in practice. Therefore, in most practical cases, $\Delta\mu_T \gg \Delta\mu_p$. This could explain why the van der Waals surface potential on occasion does not describe the adsorption or wetting layer thickness very well [76]. Unintentional temperature differences could be present in the system under study. Despite these concerns regarding thermal uniformity, in the following, we assume that $\Delta\mu_T = 0$, as is normal. However, situations may arise where $\Delta\mu_T$ may play a dominant role.

Thus far we have only described individual terms which enter Eq. (8) but not how these individual terms interact and control the shape of $V(l)$ which, in turn, influence the wetting behavior of droplets on a surface. As a prelude to understanding $V(l)$, we first examine the wetting behavior of droplets. Let us reconsider Fig. 3b. If we decrease the amount of liquid or increase the container size, eventually we will end up with a liquid droplet residing on the bottom of the container or, equivalently, a droplet residing on a solid substrate (Fig. 2a). The liquid and vapor phases are still in coexistence. If the temperature is now increased, σ_{LV} decreases faster than the difference $\sigma_{SV} - \sigma_{SL}$ because the thermal expansion coefficient of liquids are, in general, larger than solids. Hence, according to Young's equation [Eq. (5a)], the contact angle θ_∞ decreases with increasing temperature where both θ_∞ and S [Eq. (5b)] are equal to zero at the wetting transition temperature T_w. Fig. 4a provides an example of this decrease in θ_∞ with increasing temperature. At and above T_w the solid substrate is covered by a macroscopically thick wetting film (complete wetting). Below T_w, where $S < 0$ and $\theta_\infty > 0$, the solid surface around the liquid droplet is preferentially covered by an adsorbed film of thickness l_a and energy σ_{SV}. The horizontal blue dashed line in Fig. 3a represents the wetting temperature T_w, below which one finds partial wetting ($\theta_\infty > 0$) and above which one finds complete wetting ($\theta_\infty = 0$). The wetting of the solid substrate, above T_w, also surprisingly influences the surface behavior in the one-phase region (where the bulk liquid is no longer a stable phase). A prewetting line (light solid line, Fig. 3a) adjoins the coexistence curve at T_w [77–79]. Consider a fixed vapor density ρ_V in the one phase region (Fig 3c) where one decreases the temperature and crosses the prewetting line. Above the prewetting line an adsorbed layer covers the solid substrate (or container walls). As one crosses the prewetting line, the film thickness on the solid substrate undergoes a first-order jump and the solid substrate is covered by a prewetting layer, the thickness of which approaches the wetting layer thickness on the coexistence curve. The prewetting line ends at a prewetting critical point at temperature T_{pwc} (Fig. 3a), as discussed later.

How is the physics of this liquid-solid wetting transition captured within the temperature variation of the interfacial potential $V(l)$? Let us consider a specific example, namely, the wetting of a hexadecyltrichlorosilane (HTS) coated silicon wafer by an n-octane droplet. (Such a silicon wafer is coated by an alkane-like layer, which is sixteen carbons long.) Two parameters control this wetting transition due to, respectively, the short-range and long-range interactions at the surface. The short-ranged interaction is controlled by the hexadecyltrichlorosilane layer, which coats the silicon wafer, more specifically, the methyl terminal group ($-CH_3$) of this monolayer determines the short-ranged interactions. The critical surface tension for a methyl terminal group is $\sigma_{crit} \sim 19$–21 mN/m where this range in values originates from slight variations in the surface density of the alkyl silane coating layer (governed by the surface preparation). Liquids with $\sigma_{LV} < \sigma_{crit}$ completely wet the solid substrate with $\theta_\infty = 0$, whereas, liquids with $\sigma_{LV} > \sigma_{crit}$ partially wet the solid substrate with $\theta_\infty > 0$ [80]. Hence, $\sigma_{LV} = \sigma_{crit}$ is equivalent to $S = 0$, namely,

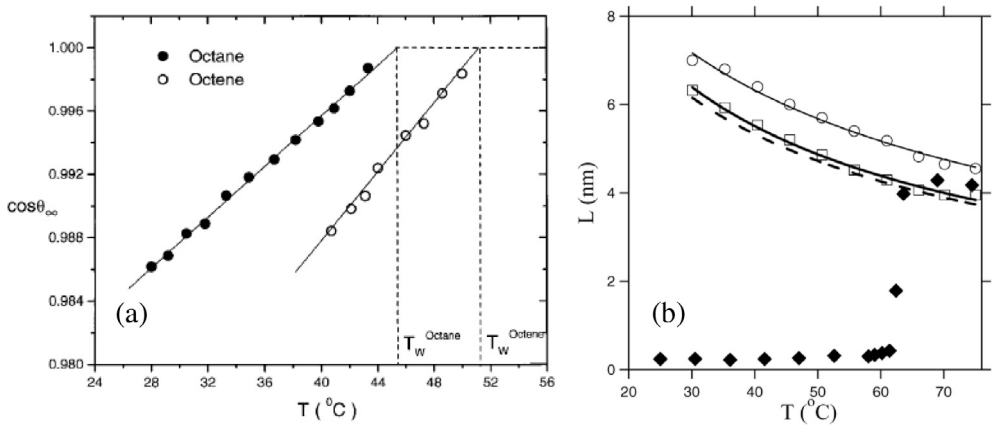

Fig. 4. (a) Variation of $cos\theta_\infty$ with temperature T for an octane and octene droplet on a hexadecyltrichlorosilane coated silicon wafer. At T_w $cos\ \theta_\infty = 1$. Reprinted (adapted) with permission from [9], © (1999) American Physical Society. (b) Thermal variation of wetting layer thickness on a hexadecyltrichlorosilane coated silicon wafer at a height $H \sim 5$ mm above n-hexane (circles), n-heptane (squares) and n-octane (diamonds) liquid. Reprinted (adapted) with permission from [81], © (2003) American Chemical Society.

$$\sigma_{crit} = \sigma_{SV} - \sigma_{SL} \tag{15}$$

according to Eq. (4).

As $\sigma_{LV}(octane) = 21.8$ mN/m, an n-octane droplet will be partially wetting this HTS coated solid substrate at room temperature, however, as σ_{LV} decreases with increasing temperature the octane droplet will undergo a wetting transition at some higher temperature (Fig. 4a). For an octane droplet on a HTS coated silicon wafer, as this system is uncharged ($V_C = 0$) and at liquid-vapor coexistence ($V_{cx} = 0$), the non-retarded van der Waals potential [Eq. (9a)] determines the long-range interaction where the optical contribution primarily determines the Hamaker constant (as octane is non-polar). Therefore, $A > 0$ because $n_S(silicon) > n_L(octane)$ in Eq. (11b). These short- and long-range interactions imply that the interaction potential $V(l)$ [Eq. (8)] possesses the form depicted in Fig. 5a for $T < T_w$ where $S < 0$ and $\theta_\infty > 0$ according to Eq. (5b) in the partial wetting regime. For this situation, a finite contact angle droplet is surrounded by an adsorbed layer of thickness l_a. With increasing temperature, $|S|$ decreases and therefore θ_∞ decreases until, at the (first-order) wetting transition temperature T_w, $S = 0$ and therefore $\theta_\infty = 0$ and the liquid completely wets the solid substrate. Fig. 5 documents how the interaction potential $V(l)$ varies as a function of temperature below, at and above the wetting transition T_w. Fig. 4a shows the temperature dependence of $cos\theta_\infty$ for an n-octane or octene droplet on a hexadecyltrichlorosilane coated silicon wafer where θ_∞ approaches zero at the wetting transition where $T_w \sim 46$ °C for n-octane [9].

According to Fig. 5 an alternative signature of a first-order wetting transition is a jump in the liquid layer covering the solid substrate from an adsorption thickness l_a, below T_w, to a wetting layer thickness l_w, above T_w determined by the minimum in the interfacial potential [$l_w \to \infty$ at liquid-vapor coexistence ($\Delta\mu = 0$)]. This jump in layer thickness is readily observed away from liquid-vapor coexistence where $\Delta\mu l > 0$ [Eq. (13)], for example, by examining the variation in liquid layer thickness on a substrate (or on the container wall Fig. 3b) at a height H above the liquid-vapor surface as a function of temperature. As V_{cx} varies linearly with l, the presence of this term changes the shape of $V(l)$ as shown by the dashed-dotted line in Fig. 5b. Thus, when this term is present, the wetting transition temperature T_w is expected to move to higher temperature where additionally the wetting thickness l_w is now finite, as described below. For this situation Eq. (8b) becomes

$$V(l) \sim \frac{A}{l^2} + \Delta\mu l + \sigma_{SL} + \sigma_{LV}, \quad l \gg l_a. \tag{16}$$

at large layer thickness and the wetting layer thickness can be determined from the minimum in this energy, namely,

$$\left.\frac{dV}{dl}\right|_{lw} = 0, \tag{17a}$$

hence,

$$l_w = \left(\frac{2A}{\Delta\mu}\right)^{1/3} \tag{17b}$$

where, as expected, $l_w \to \infty$ as $\Delta\mu \to 0$. The wetting transition is determined from the condition that

$$V(l_a) = V(l_w) \tag{18a}$$

at T_w, namely, from Eqs. (16), (18a), and (4)

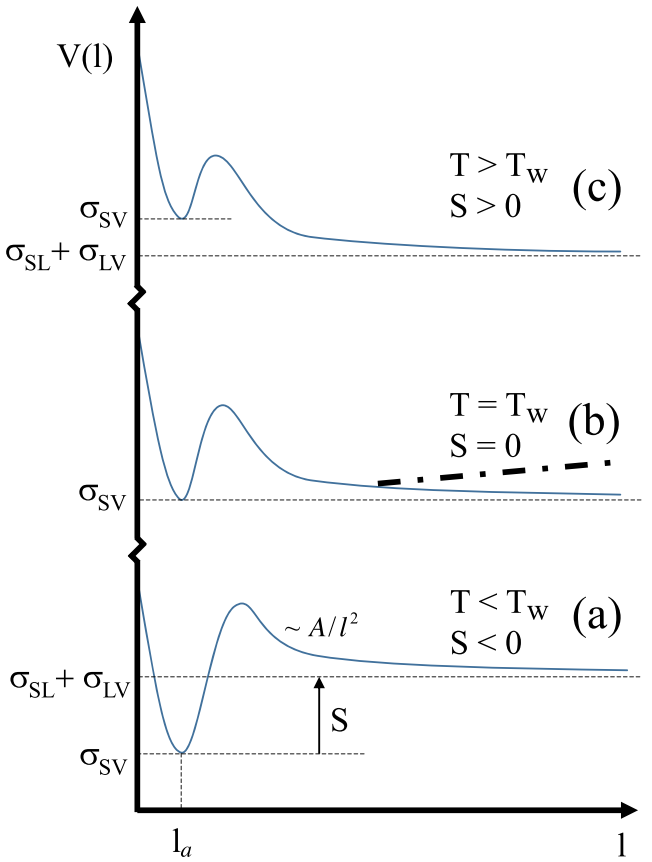

Fig. 5. Interaction potential $V(l)$ as a function of liquid film thickness l on a solid substrate for Hamaker constant $A > 0$ for temperatures (a) below, (b) at, and (c) above the first-order wetting transition temperature T_w. This interaction potential is applicable for an n-octane droplet on an alkyl-silane coated silicon wafer, as described in the text. For $T < T_w$, in the vicinity of the three-phase *SLV* contact line, the film thickness varies as shown in Fig. 2b. The droplet is surrounded by an adsorbed film of thickness l_a and energy σ_{SV} on the vapor side of the 3-phase contact line. On the liquid side of the 3-phase contact line, l progressive thickens and approaches an energy of $\sigma_{SL} + \sigma_{LV}$. In (b) above the dashed-dotted line indicates the change in shape for $V(l)$ due to the presence of an off-coexistence term $V_{cx} = \Delta\mu l > 0$.

$$S = \frac{A}{l_w^2} + \Delta\mu l_w \tag{18b}$$

which reduces to $S = 0$ when $\Delta\mu = 0$ and $l_w \to \infty$, as expected.

Fig. 4b shows the variation in wetting layer thickness for n-hexane (open circles), n-heptane (open squares) and n-octane (solid diamonds) vapor wetting a hexadecyltrichlorosilane coated silicon wafer [81]. This silicon wafer is suspended at a height $H \sim 5$ mm above each liquid. n-Hexane and n-heptane, which possess a lower surface tension than n-octane, completely wet the silicon wafer. n-Octane vapor exhibits a first-order wetting transition, indicated by the jump in thickness at a temperature $T_w \sim 60$ °C. This n-octane vapor wetting transition is about 15 °C higher than that observed for a macroscopic n-octane droplet wetting a hexadecyltrichlorosilane coated silicon wafer determined from contact angle measurements (Fig. 4a).

Thus far, we have used the interfacial potential $V(l)$ [Eq. (8)] to describe the first-order wetting transition. This equation must necessarily also describe more exotic wetting transitions, such as, the prewetting transition [77–79] and the critical wetting transition [82]. As mentioned earlier, the blue horizontal dashed line in Fig. 3a denotes a (first-order) wetting transition temperature T_w where, for $T < T_w$, a droplet partially wets the substrate with finite non-zero contact angle $\theta_\infty > 0$ while, for $T > T_w$, the substrate is completely wetted by the liquid with $\theta_\infty = 0$. In the one phase region of the phase diagram a prewetting line joins the bulk coexistence curve at T_w (Fig. 3a, light solid line). The presence of an interfacial potential Eq. (8b) stabilizes a prewetting film (e.g., on the container walls, Fig. 3c) even though the bulk liquid phase is not yet a stable phase. For example, in the gaseous phase at a fixed density ρ_v, which intersects the prewetting line, the temperature T can be varied above and below the prewetting line. Assuming we are not too near the critical point the vapor pressure p, in the gaseous phase, will be approximately ideal and given by

$$p = \rho_v RT. \tag{19}$$

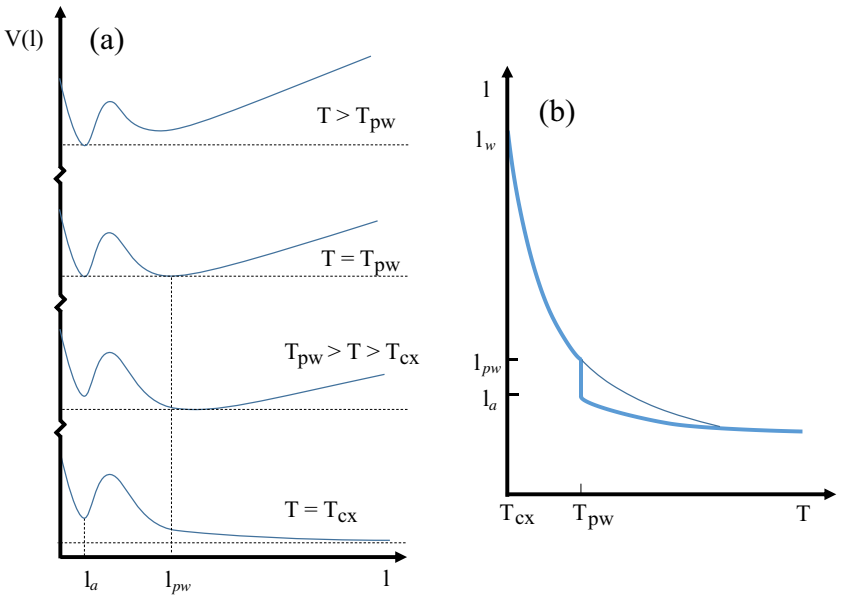

Fig. 6. (a) Variation in the interfacial potential $V(l)$ in the vicinity of the pre-wetting (T_{pw}) and coexistence (T_{cx}) temperatures. (b) Corresponding variation in the pre-wetting thickness as a function of temperature. Heavy solid line: pre-wetting thickness at absolute minimum in $V(l)$ for each temperature where a discontinuous jump in thickness is observed at T_{pw} with decreasing temperature. Light solid line: thicker pre-wetting film (l_{pw}) may become metastable with increasing temperature.

At temperatures above the prewetting line, the container wall will be coated with an adsorption film thickness l_a. If the temperature is dropped below the prewetting line, there will be a first-order jump in film thickness (Fig. 6) dictated by Eqs. (17a) and (17b). During this transition, the chemical potential difference $\Delta\mu$ is removed from bulk liquid-vapor coexistence according to Eq. (14b) where the saturated vapor pressure that appears in this equation is at temperature T, namely, $p_{sat} \equiv p_{sat}(T)$. The prewetting line in Fig. 3a represents a line of first-order surface wetting transitions given by Eq. (18b). This prewetting line ends at a prewetting critical point with prewetting temperature T_{pwc}. The prewetting critical point corresponds to a saddle point in the interfacial potential, namely, at this point

$$\left.\frac{d^2V}{dl^2}\right|_{lw} = 0 \tag{20}$$

along with Eqs. (17a) and (17b).

Other more exotic wetting transitions must also follow from Eq. (8). For example, at bulk liquid-vapor coexistence $\Delta\mu = 0$ with $S > 0$, $B > 0$ [Eq. (9b)] and if the Hamaker constant A in Eq. (9a) changes sign from negative to positive with increasing temperature then the system will undergo a continuous or critical wetting transition (Fig. 7) at temperature T_{cw} where the wetting layer thickness diverges continuously at T_{cw} according to [82]

$$l_w \sim \frac{1}{T_{cw} - T}. \tag{21}$$

2.3. Interface displacement model for the line tension

With this prelude to wetting, and its interrelationship to the interfacial potential $V(l)$ completed, we now return to the subject of calculating the line tension. Here we follow the discussion of Indekeu [83] for calculating the line tension τ using the interface displacement model. The line tension $\tau[l(x)]$, at the three-phase contact line of a droplet on a substrate, is a functional of the interfacial film thickness $l(x)$, which varies with distance x in the vicinity of the contact line (Fig. 2b). Specifically,

$$\tau[l(x)] = \int_{-\infty}^{\infty} dx \left[\frac{1}{2}\sigma_{LV}\left(\frac{dl}{dx}\right)^2 + V(l(x))\right] + const. \tag{22}$$

where the first and second terms in the integrand account for, respectively, the energy cost due to the surface tension σ_{LV} and interfacial potential $V(l)$ in the vicinity of the surface. At equilibrium, the functional $\tau[l(x)]$ must be minimized with respect to $l(x)$, which leads to

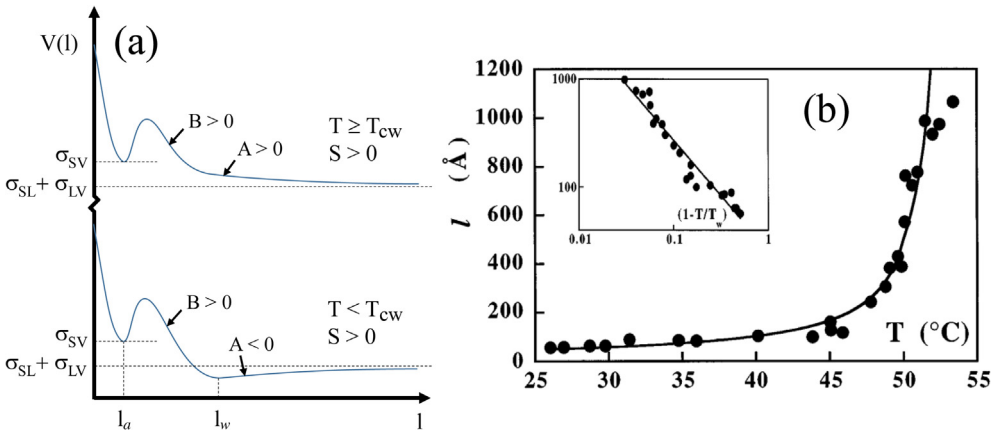

Fig. 7. (a) Interfacial potential $V(l)$ for a second-order wetting transition where the Hamaker constant A changes sign with temperature. (b) Experimental measurements of thickness variation with temperature. Reprinted (adapted) with permission from [82], © (1996) American Physical Society.

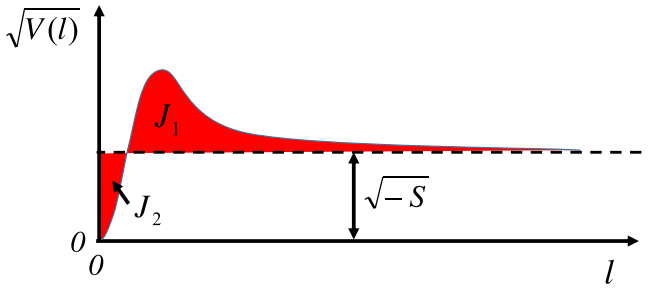

Fig. 8. Plot of $\sqrt{V(l)}$ versus thickness l, in the partial wetting regime (Fig. 5a), where the origin has been displaced to the adsorption thickness l_a. The areas J_1 and J_2 that appear in Eq. (23b) are shown in this figure.

$$\tau = \sqrt{2}\sigma_{LV}\xi \int_0^\infty dL\left[\sqrt{V(L)/\sigma_{LV}} - \sqrt{-S/\sigma_{LV}}\right] \tag{23a}$$

$$= \sqrt{2\sigma_{LV}}\xi[J_1 - J_2] \tag{23b}$$

In Eq. (23a), the correlation length ξ is a characteristic length along the substrate, while L is a dimensionless film thickness where the origin in L has been shifted to the adsorption minimum at $l = l_a$. Indekeu derived this equation for a partially wetting liquid droplet on a solid surface. Eq. (23a) possesses the same functional form as an equation derived earlier by de Feijter and Vrij [52] for a soap film in contact with a bulk liquid phase (Fig. 1d), which suggests that Eq. (23a) is rather general and relates the interfacial potential to the line tension for any three-phase contact line configuration. A plot of $\sqrt{V(l)}$ versus l, in the partial wetting regime (Fig. 5a), allows a simple geometric interpretation of the line tension where the areas J_1 and J_2 that appear in Eq. (23b) are shown in Fig. 8. (J_1 (J_2) is the area above (below) $\sqrt{-S}$.) One can readily see from Fig. 8 that for sufficiently large $|S|$ the area J_1 must be small and therefore the line tension $\tau < 0$. With decreasing $|S|$ the area J_1 increases while J_2 decreases. The line tension $\tau = 0$ when $J_1 = J_2$ while, at the first-order wetting transition temperature T_w, $J_2 = 0$ and hence $\tau > 0$.

Figs. 5, 6a and 7a show the variation of $V(l)$ with temperature T for, respectively, a first-order, pre-wetting, and critical wetting transition. Eq. (23a) can be used to predict the variation of the line tension τ with temperature T for each of these surface phase transitions. Dodds [84] modeled pentane droplets on water and calculated the variation in the line tension τ as a function of dimensionless temperature T/T_c using the interface displacement model where a first-order wetting transition occurs at $T/T_c = 0.5$ and T_c is the critical temperature for this system. As expected, from the qualitative arguments above, the line tension τ changes from a negative to a positive value on approaching a first-order wetting transition ($T/T_c \leqslant 0.5$, Fig. 9) where the line tension magnitude $|\tau| \sim 1$–8 pN. Similar considerations allow one to calculate the boundary tension τ_b between an adsorbed film and a pre-wetting film in the one-phase region (Fig. 9, $T/T_c \geqslant 0.5$) where the qualitative behavior of $V(l)$ with T was shown in Fig. 6a.

Indekeu [83] has examined how the line tension varies as a function of temperature on approaching a continuous or critical wetting transition. For this particular situation the line tension is predicted to be negative and then approach zero at T_{cw} (Fig. 10).

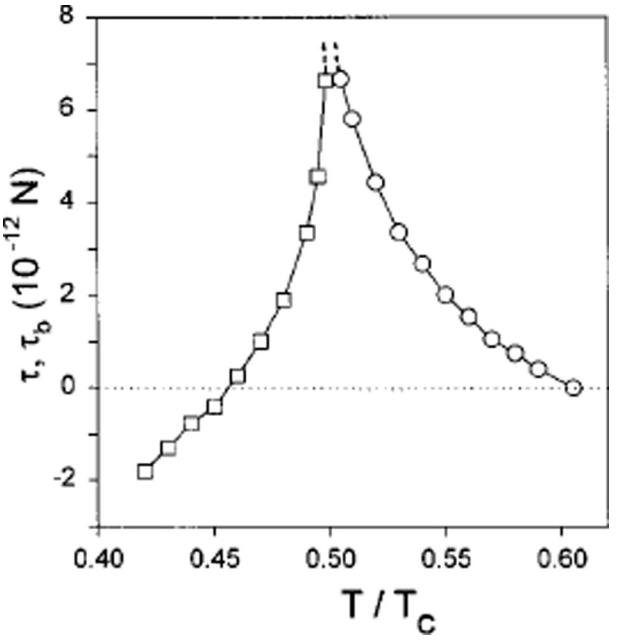

Fig. 9. Variation in line tension τ with temperature for a pentane droplet on water on approaching (from below) a first-order wetting transition at $T/T_c = 0.5$. The variation in the boundary tension τ_b with temperature between an adsorbed film and a pre-wetting film is also shown in the one phase region ($T/T_c \geqslant 0.5$). Reprinted (adapted) with permission from [84], © (1999) American Chemical Society.

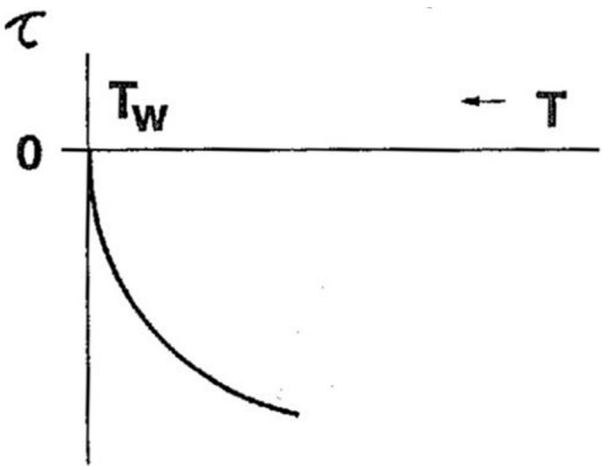

Fig. 10. Variation in line tension τ on approaching a critical wetting transition. Reprinted (adapted) with permission from [8], © (1994) World Scientific Publishing Co., Inc.

Experiments which examine the variation of the line tension τ on approaching a first-order wetting transition will be described in Section 3.2.1. The predicted variations in boundary tension τ_b on approaching a first-order wetting transition (Fig. 9, $T/T_c \geqslant 0.5$) and the line tension τ on approaching a critical wetting transition (Fig. 10) still remain to be observed.

3. Experimental perspectives on the line tension

Numerous experimental techniques have been proposed for and applied to measuring the line tension. How the line tension is extracted from each of these experimental techniques is dependent upon the specific experimental geometry. We consider a number of different geometries, specifically,

(i) spherical colloidal particles at liquid surfaces (Section 3.1),
(ii) liquid droplets at either solid or liquid surfaces (Section 3.2), and
(iii) the nucleation route to measuring the line tension (Section 3.3).

In each section the theory associated with measuring the line tension, for that geometry, is first derived. A number of experimental measurements are then reviewed. Each section ends with a critique or commentary which compares line tension measurements with theory, discusses any experimental limitations, and attempts to resolve any discrepancies between theory and experiment.

In prior sections of this review we observed that wetting behavior is determined by considering the energy minima of the interfacial potential $V(l)$ [Eq. (8)] while the line tension τ [Eq. (23a)] is determined by minimizing the line tension functional $\tau[l(x)]$ [Eq. (22)] with respect to the interfacial displacement profile $l(x)$. For mesoscopic objects (particles or liquid droplets at surfaces), considered in this section, with associated surface energies σ_{ij} and line tension τ, the behavior of this object at a surface is determined by its mechanical stability at this surface, namely, the energy minima of this object. Mathematically, the easiest situation to understand is the behavior of spherical colloidal particles at liquid surfaces, hence, we consider this situation first in Section 3.1. Insights gleamed from spherical particles at liquid surfaces will enable us to understand the mathematically more complex situations of liquid droplets at solid or liquid surfaces (Section 3.2), as well as, the nucleation route for determining the line tension (Section 3.3).

3.1. Spherical colloidal particles at liquid surfaces

The physics of colloidal particles at liquid interfaces actually differs depending upon the colloidal particle size [32,85]. In the absence of any hydrodynamic flow or colloidal mixing in the bulk solution, the gravitational potential energy of a particle (relative to the thermal energy) determines how large a particle can be *suspended in solution*. The probability distribution of particles of radius R at height H is given by

$$p \sim \exp(-4\pi R^3 \Delta\rho g H/3k_B T) \tag{24}$$

where $\Delta\rho$ is the density difference between the particle and the liquid medium. For typical liquid-solid density differences ($\Delta\rho \sim 1$–18 g/cm^3), at typical sample container heights ($H = 0.2$–1 cm), by equating the gravitational potential energy to the thermal energy, one determines the particle size limit where a change in behavior occurs. Specifically, for typical liquids and solids, this particle size limit occurs at a particle radius of $R_{grav} \sim 20$ nm (Fig. 11). For particles with $R \gg R_{grav}$ any particles in solution settle to the bottom of the sample container. Particles can still be kinetically trapped at the liquid-vapor (LV) surface by surface tension and line tension forces [85], as shown in the right hand side of Fig. 11. These large colloidal particles ($R \gg R_{grav}$) are in *mechanical equilibrium* at the liquid-vapor surface as discussed in Sec. 3.1.1 [85]. By contrast, when $R \ll R_{grav}$ particles at the liquid-vapor surface are in thermodynamic equilibrium with particles *suspended* in the bulk liquid solution, as depicted in the left hand side of Fig. 11. Small colloidal particles ($R \ll R_{grav}$), or "nanoparticles" (NPs), are therefore in *mechanical equilibrium* at the liquid-vapor surface, as well as, in *thermodynamic equilibrium* with NPs dissolved in the bulk liquid solution as discussed in Section 3.1.2 [32].

3.1.1. Large spherical colloidal particles at liquid surfaces

Fig. 12 shows a large spherical colloidal particle of radius R ($\gg R_{grav}$) at the liquid-vapor surface. It protrudes a distance h above the surface and makes a contact angle θ with the liquid-vapor surface. The three-phase solid-liquid-vapor contact line possesses a lateral radius b, circumference $2\pi b$, and line tension τ. Therefore, the energy of this colloidal particle at the liquid-vapor surface is given by

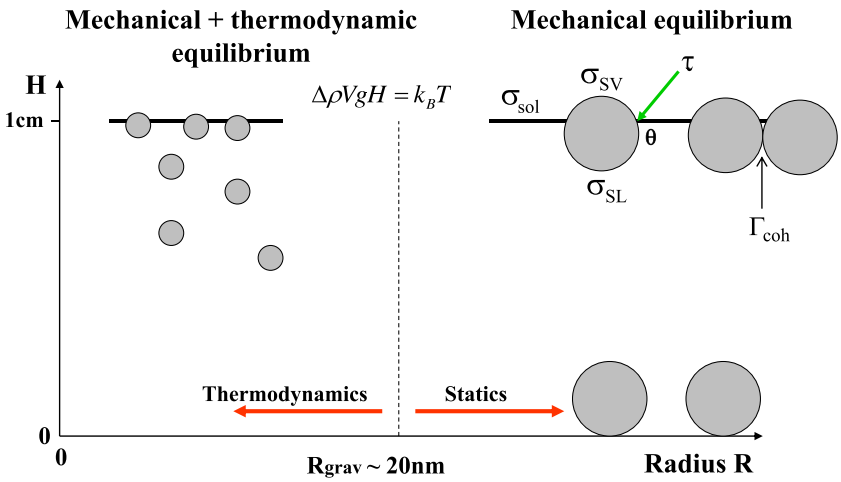

Fig. 11. Schematic of size-dependent colloidal particle behavior at liquid-vapor surfaces. When $R \gg R_{grav}$ ($R \ll R_{grav}$), described in Section 3.1.1 (Section 3.1.2), colloidal particles sediment out of solution (remain suspended in solution).

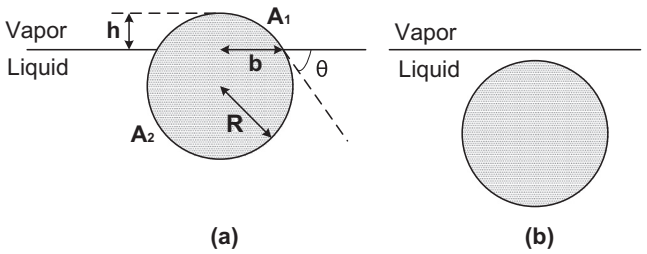

Fig. 12. (a) Spherical colloidal particle of radius R, at a liquid-vapor surface, with protrusion height h, lateral radius b, and contact angle θ. A_1 (A_2) is the particle area above (below) the liquid-vapor surface. (b) Same particle submerged below the liquid-vapor surface.

$$E_s = \sigma_{SV}A_1 + \sigma_{SL}A_2 + 2\pi b\tau \tag{25}$$

where the surface areas $A_1 = 2\pi Rh$ and $A_2 = 4\pi R^2 - A_1$. One must compare E_s with the energy if this particle is completely submerged beneath the liquid surface, namely,

$$E_b = \sigma_{SL}(A_1 + A_2) + \pi b^2\sigma_{LV} \tag{26}$$

where the last term in this expression represents the energy generated in the creation of an additional liquid-vapor surface of area πb^2.

From geometry $b = R\sin\theta$ and $h = R(1 - \cos\theta)$ and, therefore, the energy difference $E = E_s - E_b$

$$E = \sigma_{LV}\cos\theta_\infty 2\pi R^2(1 - \cos\theta) + \tau 2\pi R\sin\theta - \sigma_{LV}\pi R^2\sin^2\theta \tag{27}$$

where Young's equation [Eq. (5a)] has been used in obtaining this equation. As the particle height h, above the liquid-vapor surface, (or correspondingly contact angle θ) is varied the energy E changes. The minimum in this energy is found from the condition that

$$\frac{dE}{d\theta} = \sigma_{LV}\cos\theta_\infty 2\pi R^2\sin\theta + \tau 2\pi R\cos\theta - \sigma_{LV}\pi R^2 2\sin\theta\cos\theta = 0, \tag{28}$$

corresponding to the particle being in mechanical equilibrium. Eq. (28) gives rise to the modified Young's equation

$$\cos\theta = \cos\theta_\infty[1 - \tau/b\sigma_{LV}]^{-1} \tag{29}$$

which describes how the contact angle θ varies due to the presence of the line tension τ where this equation necessarily reduces to $\theta = \theta_\infty$ in the absence of a line tension ($\tau = 0$).

Fig. 13a provides a picture of how the energy E varies as a function of particle radius R and contact angle θ for specific surface tension σ_{LV}, line tension τ, and macroscopic contact angle θ_∞. The solid line on this figure indicates a line of energy minima corresponding to the modified Young's equation [Eq. (29)]. This figure is more readily understood by considering cross-sections through this figure, at fixed particle radius R, as shown in Fig. 13b. The modified Young's minimum occurs at $\theta \sim 1$ rad. For $R > 124$ nm, this minimum is a global minimum. If 124.0 nm > $R >$ 81.6 nm then this modified Young's minimum is a local minimum as E possesses a lower value (=0) at $\theta = 0°$ (i.e. complete wetting of the colloidal particle). A colloidal particle residing in this local minimum will remain in this metastable state because the height of the energy barrier (compared with the lowest energy state at $\theta = 0°$) is tens of thousands of k_BT. For a sufficiently small colloidal particle, defined by a minimum radius $R_{min} = 81.6$ nm, the local modified Young's minimum disappears and E exhibits saddle-point behavior where the colloidal particle will slip below the surface into the liquid phase. The saddle-point is defined by $(d^2E/d\theta^2)\big|_{\theta_{\min}} = 0$ where

$$\frac{d^2E}{d\theta^2} = \frac{2\pi R^2\sigma_{LV}}{\cos\theta}[\cos\theta_\infty - \cos^3\theta]. \tag{30}$$

This leads to a minimum contact angle θ_{min}, below which colloidal particles will slip below the surface, where

$$\cos\theta_{\min} = [\cos\theta_\infty]^{1/3}. \tag{31}$$

Combining Eqs. (29) with (31) leads to a minimum colloidal particle radius R_{min} given by

$$R_{\min} = \tau[\sigma_{LV}\sin\theta_{\min}(1 - \cos\theta_\infty/\cos\theta_{\min})]^{-1}. \tag{32}$$

Single isolated colloidal particles with $R < R_{min}$ are unstable at the liquid surface and disappear beneath the surface. Eqs. (29) and (31) have been derived earlier, via other methods, by Scheludko, Toshev and Bojadjiev [33] and Aveyard and Clint [86].

In Fig. 13b for $R = 140$ nm, the particle adsorption $\Delta E_a \sim 30{,}000\ k_BT$ (i.e. energy to move the particle from bulk liquid onto the surface), desorption $\Delta E_d \sim 50{,}000\ k_BT$ (i.e. energy to remove the particle from the surface into bulk liquid), and attach-

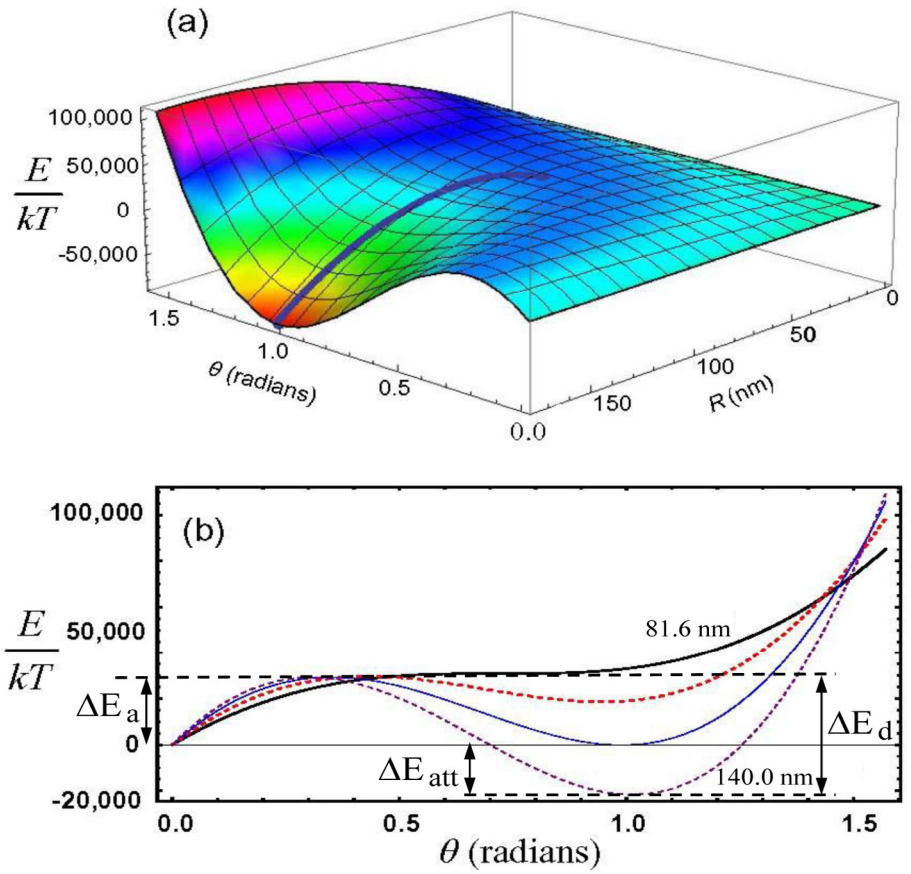

Fig. 13. (a) Energy E/k_BT [Eq. (27)] for σ_{LV} = 39.9 mN/m, τ = 0.93 nN, and θ_∞ = 64.8°. Modified Young's equation [Eq. (29)], solid line. (b) Energy cross-sections at fixed R = 81.6, 105.0, 124.0 and 140.0 nm where R_{min} = 81.6 nm [Eq. (32)], heavy solid line. For R = 140.0 nm, particle adsorption ΔE_a, desorption ΔE_d and attachment ΔE_{att} energies are shown. Reprinted (adapted) with permission from [85], © (2012) American Physical Society.

ment $\Delta E_{att} = \Delta E_a - \Delta E_d$ energies are shown. The particle adsorption ΔE_a and desorption ΔE_d energies play an important role in NP phase transfer kinetics from one liquid phase into another liquid phase which is usually initiated via ligand exchange on the NP. The ligand exchange manipulates and lowers the heights of ΔE_a and ΔE_d so that this phase transfer is readily achieved. In this transfer process the NP must first be transferred from one liquid to the liquid surface (ΔE_a) and then this NP is transferred from the liquid surface into the other liquid phase [i.e. ΔE_d appropriately modified for transfer into the "vapor" phase where σ_{SV} replaces σ_{SL} in Eq. (26)]. ΔE_a, ΔE_d, and ΔE_{att} are discussed in more detail in Section 3.1.3.

The analysis above suggests three alternative methods for determining the line tension τ:

(i) Measure the contact angle θ and deduce τ from the modified Young's equation [Eq. (29)].
(ii) Estimate τ from R_{min} [Eq. (32)], below which single isolated colloidal particles are no longer stable at the liquid/vapor surface.
(iii) Deduce τ from an estimate of the desorption energy ΔE_d for removing a particle from the liquid surface into the bulk liquid phase.

Early studies obtained estimates for the line tension τ using all three methods by employing optical microscopy and Langmuir trough pressure isotherms. Optical microscopy measurements [87] of the contact angle θ versus fluorinated silica particle radii (for $R > 10$ μm) at the dodecane/air surface placed an upper limit on the line tension $\tau < 10^{-7}$ N (Fig. 14a), however, this study possessed insufficient resolution to determine the precise magnitude of τ. Optical microscopy estimates for R_{min}, for large silica particles ($R \sim 50$ μm), obtained line tension values of $\tau \sim 10^{-11}$ N [88]. For such large particles, the weight and buoyancy force on the particles must be included in the governing equations. As observed in a later discussion [Eq. (63)], these weight and buoyancy contributions add a significant degree of complexity to these equations. By comparing the collapse pressure of a densely packed layer of particles, at the surface of a Langmuir trough, to $N\Delta E_d$ where N is the areal number density of particles for a closely packed layer the line tension was estimated to be $\tau \sim 10^{-11}$ N [89]. Computer simulations [90,91] and experiments [92], however, indicate that the Langmuir trough collapse pressure may not necessarily

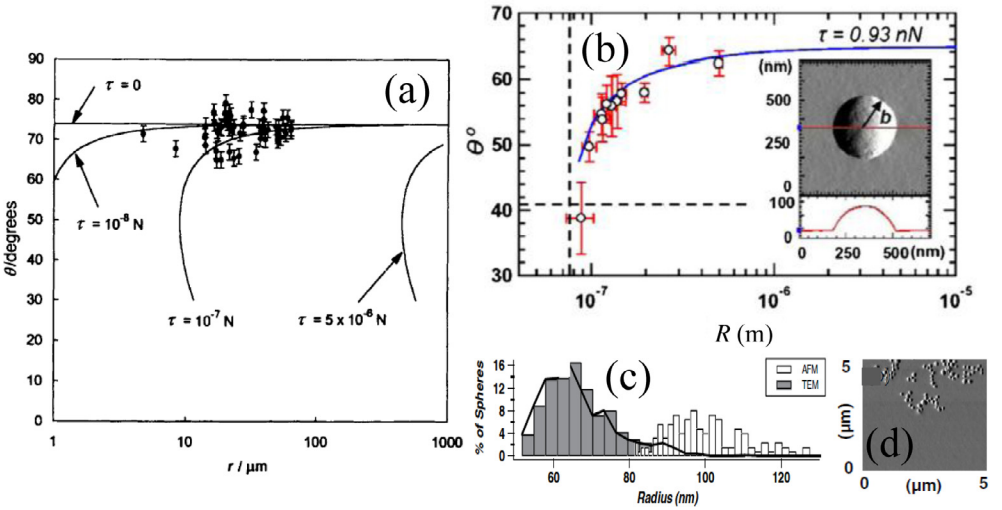

Fig. 14. (a) Optical microscopy contact angle θ vs particle radius for fluorinated silica particles at dodecane-air surface. Reprinted (adapted) with permission from [86], © (1996) Royal Society of Chemistry. (b)–(d) Results for dodecyltrichlorosilane coated silica particles at PS-air surface. Reprinted (adapted) with permission from [85], © (2012) American Physical Society. (b) AFM contact angle θ vs radius R. Vertical (horizontal) dashed line R_{min} (θ_{min}). Inset: AFM phase image and cross-sectional height. (c) Polydisperse sample of average radius ~65 nm measured via TEM (solid rectangles and solid line), surface distribution of this sample at PS-air surface measured via AFM (open rectangles). (d) AFM image of NPs at PS-air surface.

be a good measure of the line tension. Associating $N\Delta E_d$ with a collapse pressure assumes complete expulsion of a close-packed NP layer into the bulk liquid phase, whereas, the collapse pressure may be more indicative of the buckling and folding of a close-packed NP layer.

Clearly, in order to measure the line tension with high precision, an accurate estimate of the contact angle θ of the NP with the liquid surface is necessary. Grigoriev et al. [93] and, more recently, Maestro et al. [94] and Zanini and Isa [95] provide an extensive review along with a critique of the many differing experimental techniques to estimate the contact angle of NPs at liquid surfaces. A number of the experimental methods suggested for measuring θ (ellipsometry, reflectometry, Langmuir trough) do not measure θ directly and instead require some interpretation of these measurements (a model for the surface packing) in order to extract θ. Additionally, these measurements extract an average $\langle\theta\rangle_{ave}$ from a layer of particles at the liquid surface, whereas, the energy difference E [Eq. (27)] is strictly valid only for single isolated colloidal particles. It is not known whether the average $\langle\theta\rangle_{ave}$ depends upon the particle cluster size, as clusters of particles possess an additional cohesive energy Γ_{coh} (see Fig. 11) between adjacent particles, which is not present in energy E. This question has been examined recently in a combined neutron reflectivity and computer simulation investigation of gold nanoparticles coated with an alkanethiol layer [96]. Neutron reflectivity provides a route to measure the contact angle of nanoparticle monolayers in situ. Simulation and experimental contact angles exhibit good agreement. The simulations indicate that the contact angles of particles within a monolayer are ~3° larger compared with the contact angle for isolated particles. Using the energy, $\Delta E = -\pi R^2 \sigma_w (1 - cos\theta_\infty)^2$ (Eq. (41), where line tension effects are ignored, as a first approximation), for the detachment of a particle into water, the nanoparticle radius (R = 7 nm), and the water surface tension σ_w, we estimate that a variation in the contact angle of ~3° reflects changes in the adsorption energy of about 100 k_BT (T = 300 K), which corresponds to ~10% of the adsorption energy for a hydrophobic particle possessing a contact angle of θ_∞ = 121°. This amount can be considered a small correction to the actual energy, and we therefore expect that measurements of monolayers to provide a good approximation to the adsorption energy for isolated particles. Finally we note that if there is any buckling of the layer, or, if multilayers of particles form on the liquid surface then the methods discussed above will lead to an erroneous determination for θ.

Nanoscopic techniques, which directly measure the contact angle θ of particles at liquid surfaces are likely to provide a more reliable measure of the line tension τ. A number of novel experimental techniques have been developed. Paunov [97,98] developed a novel gel trapping technique where spherical colloidal particles are trapped at the aqueous-air or aqueous-oil surface by gelling the aqueous phase using a non-adsorbing hydrocolloid polymer. A replica of the colloidal particles, embedded in this gelled aqueous surface, is then made using a poly-dimethylsiloxane silicone elastomer (PDMS). The PDMS replica of the surface can then be studied using either scanning electron microscopy (SEM) [97] or AFM [98]. This technique has been used extensively to measure particles at liquid surfaces [94]. An assumption in this gel trapping technique is that additives (e.g., spreading solvent, non-adsorbing hydrocolloid polymer, PDMS) do not influence the contact angle that the colloidal particle makes with the liquid surface. Recently Maestro et al. [99] noted a spreading solvent dependence to the contact angles measured via this technique, which they attributed to the porosity/surface roughness of the particles that they used.

Isa and coworkers [100,101] developed a freeze/fracture shadowing technique to study colloidal particles at liquid/liquid surfaces. In this technique NPs are rapidly frozen at a liquid/liquid interface (eg. water/decane). This interface acts as a weak fracture plane. NPs embedded in the fractured surface are shadow cast using tungsten at an oblique angle. Cyro-SEM can then be used to image the shadow pattern from which the contact angle of the NP with the surface can be determined.

For both the gel trapping technique, as well as, the freeze/fracture shadowing technique it is difficult to assess if mechanical stress, applied to the interface, in peeling the PDMS replica off or in fracturing the liquid-liquid surface perturbs the heights h with which the NPs protrude out of the surface. Any perturbation would lead to a wider distribution in contact angles θ than is naturally present for an unfractured liquid/liquid interface.

McBride and Law developed a new experimental technique, which quantitatively tests the predictions of the modified Young's equation, as well as, associated equations [Eqs. (29), (31) and (32)]. The difficulty in the past has been to precisely measure the contact angle θ of NPs at the *LV* surface with high precision without perturbing these particles away from their equilibrium position. These authors achieve this aim by preparing dodecyltrichlorosilane ligated silica particles at a polystyrene(PS)-air surface in the liquid PS phase. The PS is then allowed to cool slowly below the glass transition temperature so that these NPs are embedded and protrude above the PS solid-air surface. Atomic Force Microscopy (AFM) then enables these embedded particles to be imaged with nanometer spatial resolution (Fig. 14b, inset). From a measurement of the lateral radius b and protrusion height h one can determine the NP radius R and contact angle θ for single isolated NPs at this PS-air surface. Eleven different groups of NPs with differing average radii in the range $R \sim 80$ nm–1 μm were made. Fig. 14b summarizes their measurements. The horizontal and vertical dashed lines on this figure represent, respectively, θ_{min} [Eq. (31)] and R_{min} [Eq. (32)] below which single isolated NPs are no longer stable at the *LV* surface. The solid line through the experimental data represents a best fit to the modified Young's equation [Eq. (29)] with $\tau = 0.93$ nN. Hence, the experimental data in Fig. 14b are in precise agreement with the predictions, which arise from the modified Young's equation, where the experimental data indicates that $R_{min} \sim 80$ nm for this system.

As a further check on the reliability of $R_{min} \sim 80$ nm, McBride and Law also studied a polydisperse NP sample possessing an average particle radius $R_{ave} \sim 65$ nm and a broad size distribution, as shown by the TEM size distribution in Fig. 14c (solid rectangles and solid line). When this polydisperse sample adsorbed at the PS-air surface only large NPs, larger than ~80 nm, remained at this surface [Fig. 14c, AFM size distribution (open rectangles)], thus confirming the value for R_{min}. It is somewhat surprising that, for the AFM size distribution exhibited in Fig. 14c, even rafts of particles on the interface (Fig. 14d) did not contain any particles smaller than R_{min}. The equations in this section are strictly valid only for single isolated particles. These equations do not preclude small particles, less than R_{min}, within clusters. The absence of these small particles, within clusters, suggests that the particle-particle cohesive energy (Γ_{coh} in Fig. 11) is much, much smaller than E [Eq. (27)].

$\tau \sim 1nN$ (Fig. 14b) is an order of magnitude larger than theoretical expectations arising from van der Waals contributions to the line tension (Sections 2.1 and 2.3). This disagreement with theory is discussed in Section 3.1.3 together with a potential explanation.

X-ray and neutron reflectivity techniques have also been employed to investigate the adsorption of nanoparticles at the air-water and water-hexane interfaces, and investigate the monolayer structure [102,103]. X-ray reflectivity has also been applied to measure the contact angle of iron oxide nanoparticles coated with poly(ethylene glycol) [104]. Recently, Reguera et al. [96] presented an experimental method based upon neutron reflectivity. This method, as mentioned above, provides a route to the "in situ" measurement of the contact angle of small particles. In this way it circumvents problems associated with indirect methods, which rely on the transport of monolayers to solid substrates for later analysis. The method was illustrated to measure the contact angles of 7 nm diameter gold nanoparticles coated with octanethiol (OT) layers and mixtures of OT mercaptohexanol. The interpretation of the neutron reflectivity profiles requires a fitting to a geometrical model, which can be validated using atomistic computer simulations.

3.1.2. Small spherical colloidal particles at liquid surfaces

As mentioned in Section 3.1, if the NPs are sufficiently small ($R < R_{grav} \sim 20$ nm), then NPs adsorbed at the surface are in thermodynamic equilibrium with NPs suspended in the bulk liquid solution. For thermodynamic equilibrium, the chemical potential of a colloidal particle at the liquid surface must equal the chemical potential of a colloidal particle in the bulk liquid phase. Hence, according to Prigogine and Marechal [105],

$$\frac{\varphi_s}{1-\varphi_s} = \frac{\varphi_b}{1-\varphi_b} \exp(-E/k_BT) \tag{33}$$

where φ_s (φ_b) is the surface (bulk) volume fraction of colloidal particles and E is given by Eq. (27). Additionally, the adsorbed NPs must also be in mechanical equilibrium at the surface, i.e. the modified Young's equation [Eq. (29)] is valid.

Wi et al. [32] used surface tension measurements to test the concepts implicit in Eq. (33). In this study the surface tension σ of the NP solution was measured as a function of bulk NP concentration in the liquid for various n-alkane solvents, from n-nonane to n-octadecane at a temperature of 30 °C. The NPs used in these experiments were 5 nm diameter Au NPs ligated with dodecanethiol. Fig. 15a shows this functional dependence for a selection of n-alkane solvents. The surface tension results are complex. For pure n-alkanes, the surface tension increases with increasing n-alkane chain length ($\sigma_{C18} > \sigma_{C16} > \sigma_{C12} > \sigma_{C10} > \sigma_{C9}$), as expected. However, at sufficiently high NP concentration (0.25 mg/mL) the surface tension dependence is disordered, specifically, $\sigma_{C12} > \sigma_{C16} > \sigma_{C10} > \sigma_{C18} > \sigma_{C9}$.

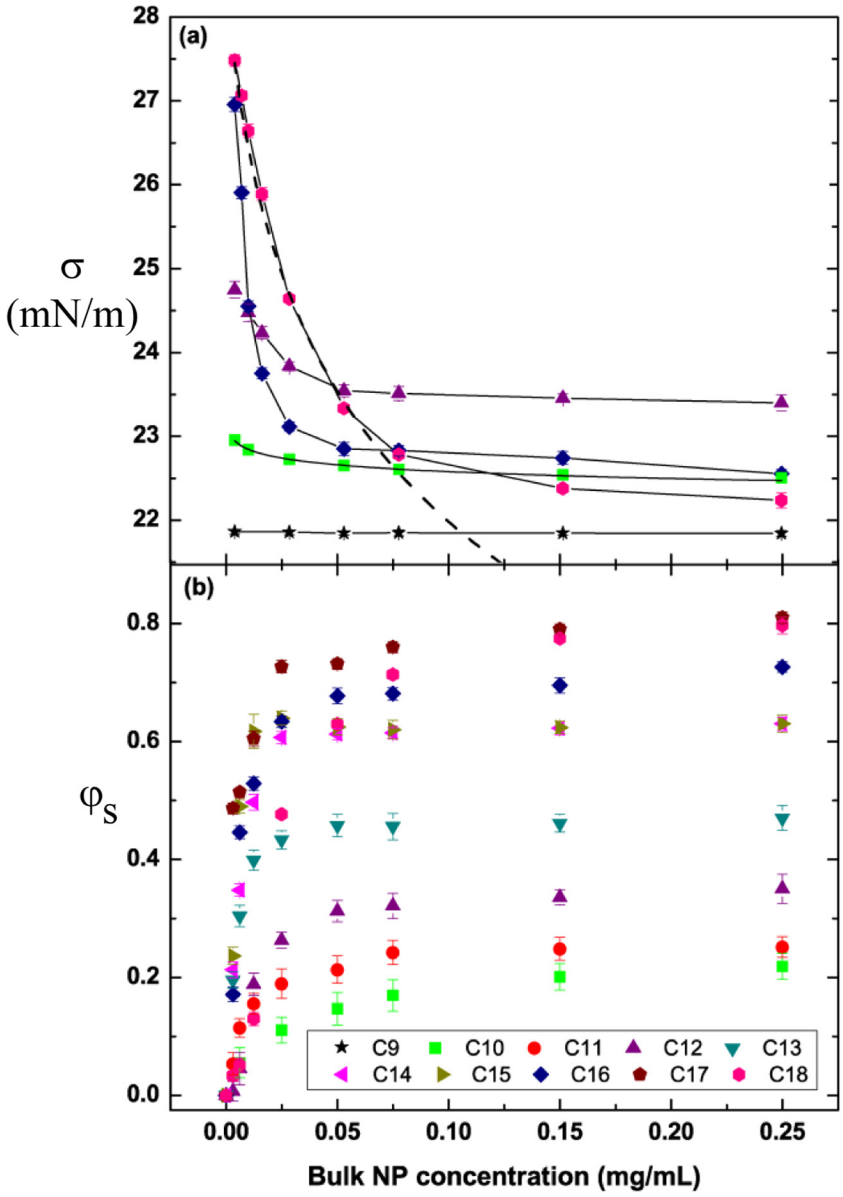

Fig. 15. (a) Liquid-vapor NP solution surface tension σ as a function of bulk dodecanethiol ligated Au NP concentration for selected n-alkane solvents. Solid line: guide to eye. (b) Surface concentration φ_s, deduced from Eq. (34), as a function of bulk NP concentration. Reprinted (adapted) with permission from [32], © (2011) American Chemical Society.

To deduce whether or not these surface tension results are consistent with Eq. (33) one must first relate the NP surface volume fraction φ_s to the solution surface tension σ. The most straightforward assumption is to assume the following constitutive equation

$$\sigma = \varphi_s \sigma_{NP} + (1 - \varphi_s)\sigma_{sol} \tag{34}$$

where the NP surface energy

$$\sigma_{NP} = \sigma_{SV} - \sigma_{SL} = \sigma_{crit} \sim 20.9 \text{ mN/m} \tag{35}$$

and σ_{sol} is the solvent (i.e. pure n-alkane) surface tension. The critical surface tension, σ_{crit}, defines a property of the terminal ligand group that coats the solid surface [80], specifically, the methyl terminal group ($-CH_3$) for the current situation. Solvents with $\sigma_{sol} < \sigma_{crit}$ ($\sigma_{sol} > \sigma_{crit}$) completely wet (partially wet) the solid surface with $\theta_\infty = 0$ ($\theta_\infty > 0$). Eq. (34) allows one

to convert each σ value to φ_s; thus, converting Fig. 15a into Fig. 15b. Figure 15b exhibits a much more systematic trend, with increasing n-alkane chain length, than does Fig. 15a.

In order to understand how Eq. (33) may be used to interpret Fig. 15b, this equation can be rewritten more explicitly as

$$\frac{\varphi_s}{1-\varphi_s} = \frac{\varphi_b}{1-\varphi_b} \exp\left[\frac{\pi b^2 \sigma_{sol} - 2\pi R h \sigma_{NP} - 2\pi b \tau}{k_B T}\right]. \tag{36}$$

Additionally

$$h = R(1-\cos\theta), \tag{37}$$

$$\cos\theta = \sqrt{1-\left(\frac{b}{R}\right)^2}, \tag{38}$$

and, according to Eq. (29),

$$\tau = b\sigma_{sol}(1-\cos\theta_\infty/\sqrt{1-(b/R)^2}). \tag{39}$$

Hence, when Eqs. (37)–(39) are substituted into Eq. (36) each (φ_s, φ_b) pair is a function solely of the lateral radius b. Thus, for each (φ_s, φ_b) pair in Fig. 15b one can determine the lateral radius b, or, equivalently the surface area $\alpha = \pi b^2$. Fig. 16a shows a plot of α versus bulk NP concentration. Similarly, once b is known then θ and τ can be determined from, respectively, Eqs. (38) and (39). τ and θ are plotted as a function of bulk NP concentration for each n-alkane solvent in, respectively, Fig. 16b and c. Fig. 16a–c indicate that α, τ, and θ are independent of the bulk NP concentration, thus, average values for each n-alkane solvent are displayed in Fig. 16d–f. α, τ, and θ are characteristic parameters, which define the positioning of individual NPs at the liquid-vapor surface and, therefore, these three parameters are not expected to be a function of the bulk NP concentration, at least, for dilute NP concentrations. At higher NP concentrations, NPs will exhibit surface clustering and the NP-NP cohesive energy Γ_{coh} (Fig. 11) will play a role. The independence of α, τ, and θ on bulk NP concentration (Fig. 16a–c) may indicate that Γ_{coh} plays a minor role relative to E [Eq. (27)].

We note that $\tau \sim 1$ pN and changes sign at C14 (Fig. 16e). The line tension magnitude found in this study agrees well with theoretical expectations, but is a thousand times smaller than the line tension determined in Section 3.1.1. This difference in line tension magnitudes found in these two studies is discussed in the next section.

3.1.3. Critique on spherical colloidal particles at liquid surfaces

In this section we provide a critique on our views on the line tension associated with NPs at liquid surfaces. In Section 3.1.2, the line tension was deduced from surface tension measurements for the adsorption of dodecanethiol ligated Au NPs at the alkane-air surface. These results will be dependent upon the accuracy of the constitutive equation [Eq. (34)]. Additionally, at high NP surface coverage, the single NP energy E [Eq. (27)], used in Eq. (33), will require modification due to the cohesive energy between adjacent NPs (i.e. Γ_{coh} in Fig. 11). Despite these deficiencies in the modeling, we believe that the magnitude of the line tension $|\tau| \sim 1$ pN is approximately correct. An additional estimate for τ can be obtained from the equation for R_{min} [Eq. (32)]. The surface tension results in Fig. 15a indicate that dodecanethiol ligated Au NPs do not adsorb at the nonane-air surface. From Wi et al. [32], σ_{sol} = 21.86 mN/m for n-nonane while θ_∞ = 16.3° for a n-nonane droplet on a dodecylsilane coated silicon wafer. Hence, θ_{min} = 9.45° from Eq. (31). Therefore, from Eq. (32) τ = 0.4 pN where we have used R_{min} = (2.5 + 1.7) nm, namely, the sum of the Au core radius and ligand length. These line tension results for dodecanethiol ligated Au NPs at the alkane-air surface therefore agree with the line tension estimates from theory and from computer simulations (Sec. 2.1). This agreement should be contrasted with the line tension results in Sec. 3.1.1 for

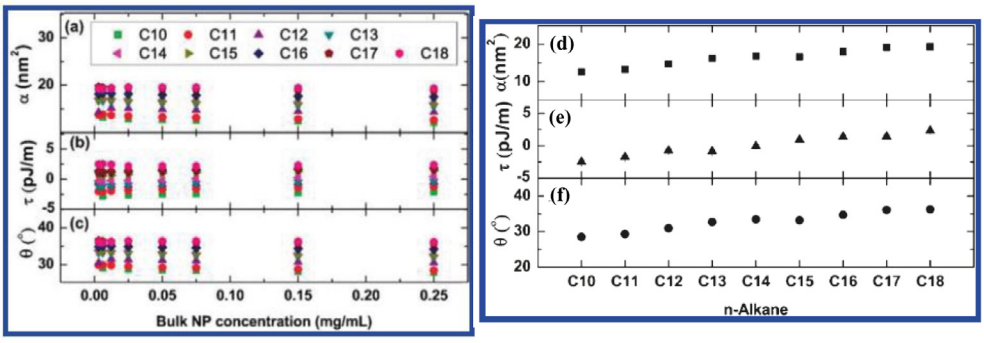

Fig. 16. (a) $\alpha = \pi b^2$, (b) τ, and (c) θ versus bulk NP concentration for various n-alkane solvents deduced from Eqs. (36)–(39). Average values for (d) α, (e) τ, and (f) θ for each n-alkane solvent. Reprinted (adapted) with permission from [32], © (2011) American Chemical Society.

dodecyltrichlorosilane ligated silica NPs at the PS-air surface where $\tau \sim 1$ nN, which is at least an order of magnitude larger than the largest theoretical estimate. This line tension value is thought to be very accurate in both magnitude and sign because all of the experimental results in Fig. 14b and c agree precisely with all of the predictions arising from the modified Young's analysis in Sec. 3.1.1 [Eqs. (29), (31), and (32)]. Why should the line tension results for Au NPs at an alkane-air surface differ so significantly from the line tension results for silica NPs at a PS-air surface? We believe that the explanation arises from the difference in the ligand and solvent structure. In Sec. 3.1.2 the Au NPs were coated with an alkyl-like ligand (12 carbons long), which is very similar in nature to the alkane solvents in which these particles were dissolved in. Thus, the primary contributions to the line tension are expected to arise from the surface tension and van der Waals contributions included in the theory (denoted τ_{vdW}), hence, the good agreement with theory. This should be contrasted with the silica NPs at a PS-air surface studied in Sec. 3.1.1. The silica NPs were coated with an alkyl-like ligand (12 carbons long), whereas, the PS ($[C_8H_8]_n$) consists of a long linear carbon chain where a benzene ring is attached to every odd numbered carbon along this chain. Thus, the NP ligand coating and PS solvent possess rather different chemical structures. It is thought that an additional point contact contribution to the line tension (denoted τ_{atom}), not accounted for within the mean field calculations, is responsible for the large line tension $\tau \sim 1$ nN observed in Sec. 3.1.1. This point contact line tension contribution is expected to be important when the ligand and solvent are dissimilar in chemical nature. The magnitude of τ_{atom} will be dependent upon the atomic structure of both ligand and solvent and how this atomic structure is able to reorient and reconfigure at the three-phase contact line in order to minimize the total free energy.

Matsubara et al. have found evidence for a point contact line tension contribution, in the vicinity of an n-alkane surface freezing transition, for n-tetradecane droplets on an aqueous surfactant-air surface [106]. In this case, there is a discontinuity in surface structure at the air-water and air-oil surfaces which gives rise to this point contact line tension contribution. Du et al. [107] studied the Brownian diffusion of negatively charged carboxylate-modified polystyrene particles with diameters 24 nm–2000 nm at the water-silicone oil surface. Their results could only be explained if a line tension $\tau \sim -1.4$ nN was present; such a line tension would arise from τ_{atom}. The line tension significantly changes the contact angle of the very smallest particles at the liquid/liquid surface and hence influences the Brownian diffusive motion of these particles.

Rusanov, Shchekin, and Tatyanenko [108] and Schimmele, Napiórkowski and Dietrich [109] have criticized using the modified Young's equation [Eq. (29)] to deduce the line tension τ. They demonstrate for a liquid droplet on a solid substrate [108,109], as well as, for a liquid droplet on a liquid surface [109] that, as all interfaces are diffuse, how one defines the placement of the "Gibb's dividing surface", which separates phases (e,g., the solid phase from the liquid phase, etc.) gives rise to additional terms in the modified Young's equation, specifically, the "notional derivatives" $\frac{d\tau}{d\theta}\big|$ and $\frac{d\tau}{db}\big|$. The line tensions inferred from the modified Young's equation may therefore be affected by the notional shifts in the interface location. The good agreement between the experiments for silica NPs at a PS-air surface and the modified Young's equation and associated equations (Fig. 14b and c), in the absence of any notional derivatives, suggests that the changes associated with these notional derivatives are small, at least, for this particular experiment.

For ligated NPs, computer simulations have demonstrated that the ligated layer may under certain circumstances, for large ligand length to core diameter ratio, acquire liquid-like properties and deform at a surface [60] or, alternatively, exhibit clustering of adjacent ligands thus leading to a patchy ligand layer [110]. However, not all computer simulations display evidence for patchiness or liquid-like properties of the ligand layer [111]. If the ligand layer exhibited patchiness or liquid-like properties then one might expect the experimental data for silica NPs at the PS-air surface to deviate from the predictions arising from the modified Young's equation for a spherical NP at a liquid surface. No deviations were observed (Fig. 14b and c) thus indicating that the assumption of a spherical NP is most probably valid. The modified Young's equation is known to depend upon shape. For example, the modified Young's equation for a spherical colloidal particle at a liquid surface [Eq. (29)] differs from the modified Young's equation for a liquid droplet at a solid surface [Eq. (7b)]. Faraudo and Bresme [112–114] have used computer simulations to examine the stability of nonspherical NPs at liquid surfaces and found that oblate particles are far more stable than prolate particles, indicating the sensitive nature of the free energy to particle shape for particles at liquid surfaces. The thermodynamic model of Faraudo and Bresme has been used to estimate the line tension of PS and PMMA micrometer size ellipsoids at liquid-liquid interfaces [115]. It was found that the contact angle of the particles increased with particle aspect ratio. This effect was interpreted in terms of an effective line tension. Line tension values of order *nN* were reported in line with the observations for silica nanoparticles at the PS-air surface in Fig. 14b.

The adsorption of NPs at *LV* surfaces, as described by the modified Young's equation, exhibits a very distinctive shape (solid lines in Fig. 14a and b). The contact angle θ. that the NP makes with the *LV* surface, only deviates significantly from the macroscopic Young's contact angle θ_∞ for particle radii very close to R_{min}. For particle radii $R > 2R_{min}$, to a good approximation, $\theta \approx \theta_\infty$ to within about ~5%. θ is only a sensitive function of R for particle radii $R_{min} < R < 2R_{min}$. Of course, if $R < R_{min}$, single isolated NPs are unstable at the *LV* surface and sink below this surface into the bulk liquid phase. As R_{min} scales directly with τ [Eq. (32)], the use of small particles in computer simulations ($R \sim 1$–2.5 nm) necessarily means that these studies are only able to detect very small line tension magnitudes in the range found by theory. Namely, the detection of larger line tensions via computer simulations requires using larger particles because small particles, with $R < R_{min}$, are unstable at the *LV* surface.

As mentioned in the preceding paragraph, for $R > 2R_{min}$ to a good approximation $\theta \approx \theta_\infty$ therefore from Eq. (27) one obtains for the attachment energy of the particle to the surface

$$\Delta E_{att} \approx -\sigma_{LV}\pi R^2(1-\cos\theta_\infty)^2 + \tau 2\pi R \sin\theta_\infty,\ R > 2R_{\min}. \tag{40}$$

In the absence of a line tension, this reduces to the often quoted attachment energy (except for the negative sign)

$$\Delta E_{att} = -\sigma_{LV}\pi R^2(1-\cos\theta_\infty)^2 \tag{41}$$

which has a minimum when $\theta_\infty = 90^o$ [116]. Occasionally, Eq. (41) is misinterpreted to imply that all particles at a liquid surface possess a contact angle $\theta_\infty = 90^o$. This is incorrect. θ_∞ is not a variable in Eq. (41). Instead, θ is a variable in Eq. (27) and, for $\tau = 0$, E possesses a minimum energy when $\theta = \theta_\infty$ [see Eq. (28)]. In other words, when $\tau = 0$, particles in equilibrium at a liquid surface possess a contact angle $\theta = \theta_\infty$, determined by Young's equation [Eq. (5a)]. ΔE_{att} is the difference between the modified Young's energy minimum and the bulk energy and one must supply at least this energy to remove the particle from the surface into the bulk liquid phase. [If a particle at the surface is removed into the bulk gaseous phase then $-cos\theta_\infty$ is changed to $+cos\theta_\infty$ in Eq. (41).] In reality one must supply more than this energy $|\Delta E_{att}|$ to remove this particle from the surface into the bulk liquid phase. According to Fig. 13b, one must supply a desorption energy

$$\Delta E_d = \Delta E_a - \Delta E_{att} \tag{42}$$

to remove a particle from the surface, which is larger than $|\Delta E_{att}|$ because of the presence of the energy barrier. From Fig. 13b, the height of the energy barrier ΔE_a is almost independent of the particle radius. One can obtain an estimate of ΔE_a by noting that this energy barrier occurs at approximately $\theta_\infty/3$ for $R > 2R_{min}$, namely, in this region $\theta \approx \theta_\infty$ and then the 140 nm curve in Fig. 13b is approximately sinusoidal up to θ_∞ at the modified Young's minimum. Therefore, from Eq. (27), to a good approximation

$$\Delta E_a \approx \sigma_{LV}\cos\theta_\infty 2\pi R^2(1-\cos(\theta_\infty/3)) + \tau 2\pi R\sin(\theta_\infty/3) - \sigma_{LV}\pi R^2\sin^2(\theta_\infty/3),\ R > 2R_{\min}. \tag{43}$$

These estimates for the adsorption ΔE_a [Eq. (43)] and desorption ΔE_d [Eq. (42)] energies to adsorb or desorb a particle from a liquid/vapor surface should provide reasonable estimates for most particles provided that $R > 2R_{min}$. In the narrow particle range $R_{min} > R > 2R_{min}$ one should return to Eq. (27) to more carefully estimate these adsorption and desorption energies.

3.2. Liquid droplets at surfaces

The ideas set out in Sec. 3.1.1, for spherical colloidal particles at liquid surfaces, can also be applied to liquid droplets at a surface with only slight modifications. In this case, the energy of the liquid droplet is minimized by changing the droplet shape at constant droplet volume. The essential ideas are analyzed in detail for liquid droplets at a solid surface in Sec. 3.2.1. The more complex situation of liquid droplets at liquid surfaces is considered in a more cursory fashion in Sec. 3.2.2.

3.2.1. Liquid droplets at solid surfaces

In this section the influence of the line tension on a small droplet situated on a flat solid surface is considered, where the droplet dimensions are less than the capillary length κ^{-1} [Eq. (1)], thus, gravity can be ignored. This liquid droplet (Fig. 17a) possesses a contact angle θ, lateral radius r, height h, liquid-vapor radius of curvature and area denoted, respectively, by R and A. {The results in this section are also approximately correct for liquid droplets at liquid-vapor surfaces [e.g., oil droplets at the water-air surface (Fig. 17b) in the presence of a surfactant [117], Sec. 3.2.2] provided that the liquid-vapor surface is approximately flat.}

Following the analysis in Sec. 3.1.1, the energy of the liquid droplet at the solid-vapor surface is

$$E_s = \sigma_{LV}A + \sigma_{SL}\pi r^2 + \tau 2\pi r \tag{44}$$

while the energy of this droplet when completely removed from the solid surface (into the vapor phase) is

$$E_b = \sigma_{LV}A_1 + \sigma_{SV}\pi r^2 \tag{45}$$

where A_1, the area of the LV surface, is related to the total oil droplet volume V via

$$A_1 = (36\pi V^2)^{1/3}. \tag{46}$$

Geometry provides the following interconnections between V, A, h, r, and R.

$$V = \pi h^2(3R-h)/3 = \pi h(h^2+3r^2)/6, \tag{47}$$

$$A = 2\pi Rh\ = \pi(h^2+r^2) \tag{48}$$

and

$$R = (h^2+r^2)/2h. \tag{49}$$

As in Sec. 3.1.1 the important quantity to consider is the energy difference $E = E_s - E_b$

$$E = \sigma_{LV}(A-A_1) + \sigma_{SL}\pi r^2 + \tau 2\pi r - \sigma_{SV}\pi r^2 \tag{50}$$

which can be transformed to

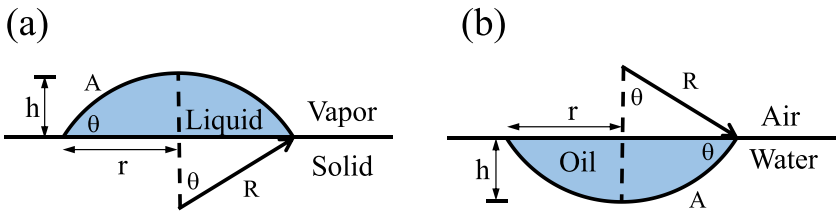

Fig. 17. (a) Liquid droplet on a flat solid substrate. Contact angle θ, liquid-vapor radius of curvature R and area A, lateral radius r, and height h. (b) Oil droplet at the water-air surface, which is assumed to be flat.

$$E = -S\pi r^2 + \sigma_{LV}\pi h^2 + \tau 2\pi r - \sigma_{LV}A_1 \tag{51}$$

with spreading coefficient S [Eq. (4)].

For the colloidal particle at a liquid surface (Fig. 12a) one examined how the energy E of the particle [Eq. (27)] varied as a function of the height h (or correspondingly contact angle θ) of the particle above the surface. For a droplet at a solid surface one needs to consider the energy E [Eq. (51)] as a function of the contact angle θ where the volume V of the droplet is fixed (i.e. $dV = 0$). For this situation the energy minimum is given by

$$\frac{dE}{dr} = 0 = -S2\pi r - \sigma_{LV}\frac{4\pi h^2 r}{h^2 + r^2} + 2\pi\tau \tag{52}$$

where, in deriving this equation, we have used the fact that

$$dV = 0 = \frac{\pi}{2}[(h^2 + r^2)\,dh + 2hr\,dr] \tag{53}$$

and $dA_1 = 0$.

As

$$r/R = \sin\theta \tag{54}$$

and

$$h = r(1 - \cos\theta)/\sin\theta \tag{55}$$

the modified Young equation given in Eq. (52) can be transformed into the better known equation

$$\cos\theta = \cos\theta_\infty - \frac{\tau}{\sigma_{LV}r} \tag{56a}$$

for the situation shown in Fig. 17a or, alternatively,

$$\cos\theta = \cos\theta_\infty - \frac{\tau}{\sigma_{OW}r} \tag{56b}$$

for the situation shown in Fig. 17b. This modified Young's equation describes how the droplet contact angle θ changes, relative to its macroscopic value θ_∞, due to the presence of a line tension τ. Of course, in the limit of zero line tension ($\tau = 0$) or infinitely large droplet ($r \to \infty$) $\theta \to \theta_\infty$. This modified Young's equation [Eq. (56a)] was first suggested without proof by Pethica [118] before subsequently being confirmed by Scheludko, Toshev, and Bojadjiev [33] and Pethica [119].

As in Sec. 3.1.1, one should also examine the second energy derivative, in order to deduce the stability of the droplet at the solid surface where [22]

$$\frac{d^2E}{dr^2} = 2\pi\left[-S + \frac{2\sigma_{LV}h^2(5r^4 - h^4)}{(h^2 + r^2)^3}\right] \tag{57a}$$

$$\approx \frac{2\pi}{r}[5\tau - 6S\,r] \tag{57b}$$

The second approximate equality [Eq. (57b)] is valid for flat droplets (i.e. $h \ll r$), near wetting, where we have used Eq. (52).

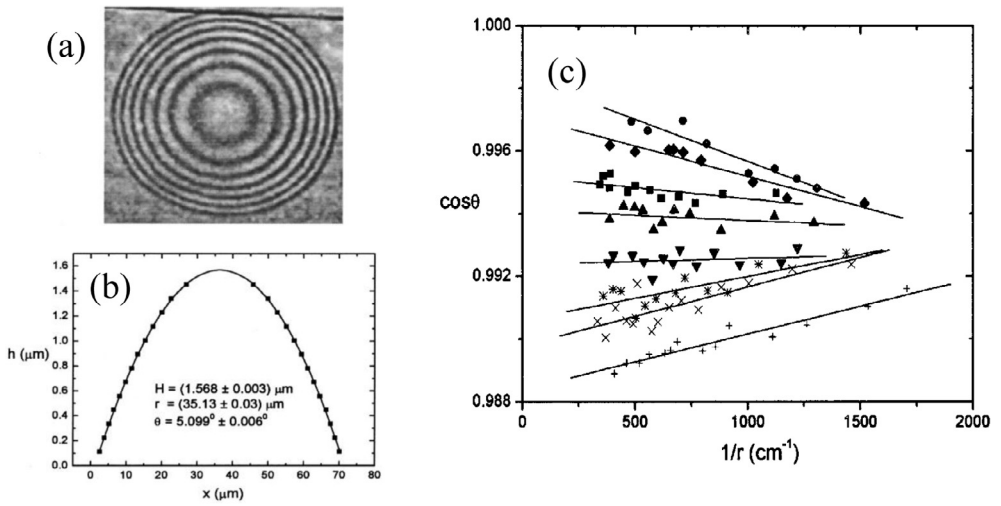

Fig. 18. (a) Optical interference fringes observed within an n-octane droplet deposited upon a hexadecyltrichlorosilane coated silicon wafer. (b) Fit of the maxima and minima interference fringes in deducing the droplet contact angle θ in (a). (c) Plot of $cos\theta$ versus $1/r$ from which the line tension is deduced using Eq. (56a). Reprinted (adapted) with permission from [10], © (2001) American Physical Society.

Eq. (56a) has frequently been used, in the past, to deduce the line tension τ of liquid droplets on solid surfaces by examining the functional dependence of $cos\theta$ with $1/r$ (the inverse droplet radius) using either optical microscopy [10,47] or Atomic Force Microscopy [6,120] techniques. If the contact angle of the droplet is small then (monochromatic) optical interference fringes, observable within the droplet (Fig. 18a and b), can be used to accurately measure θ. For larger contact angle droplets, the contact angle can no longer be deduced using optical interference techniques, thus, alternative (optical) techniques must be used, for example, magnified shadow graphs of the droplet shape [121]. AFM techniques provide higher spatial resolution of the droplet shape but are less frequently used. Optical interference techniques are particularly useful for examining the variation in the line tension, in the vicinity of a wetting transition, where the contact angle is small. Wang, Betelu and Law [9,10] examined the wetting behavior of liquid droplets of n-octane or 1-octene on a n-hexadecane silanated silicon wafer using optical interference. As the droplets were near a wetting transition (Fig. 4a) their contact angle was small and interference rings could be observed when the droplets were viewed using monochromatic light (Fig. 18a). From a fit to the positioning of the interference maxima and minima one can obtain the contact angle θ (Fig. 18b). By condensing more liquid onto the droplet (at fixed silicon wafer temperature) one can study how the contact angle changes as a function of droplet size. According to the modified Young's equation [Eq. (56a)], $cos\theta$ should vary linearly with $1/r$ where the slope is proportional to the line tension τ. This is indeed what is observed in Fig. 18c. By increasing the silicon wafer temperature the droplet contact angle decreases because one is approaching a wetting transition, hence, τ can therefore be studied on approaching a first-order wetting transition. From data such as Fig. 18c one obtains a plot of τ versus $t = (T_w - T)/T_w$ (Fig. 19). As predicted by theory (Sec. 2.3) the line tension τ changes from negative to positive as one approaches a first-order wetting transition. The line tension magnitude ~0.1–0.3 nN is similar in magnitude, or slightly larger, than the largest predictions that arise from theory.

As discussed later (Secs. 3.2.2 and 3.2.3) there is an ongoing debate as to whether or not a droplet possessing a negative line tension can cause the three-phase contact line to become unstable. For a wide temperature range in Fig. 19, liquid droplets possess a negative line tension. Hence, one might wonder about droplet stability in this region. According to Eq. (57b), as $S \sim -2 \times 10^{-4}$ N/m and $\tau \sim -0.4$ nN then the critical radius r_{crit} at which $d^2E/dr^2 = 0$ occurs at

$$r_{crit} = \frac{5\tau}{6S} \sim 2 \times 10^{-6} \text{ m} \tag{58}$$

and, therefore, all of the droplets studied in Fig. 19 are stable (i.e. for all droplets $r > r_{crit}$ and, hence, $d^2E/dr^2 > 0$). However, Eq. (57b) only provides information about the overall droplet stability of spherical capped shaped droplets, rather than the stability of the three-phase contact line to contact line fluctuations. Guzzardi, Rosso, and Virga [29] therefore examined the second variation of the free energy and demonstrated that, for the conditions in Fig. 19, the three-phase contact line is stable to sinusoidal fluctuations of this contact line (see Sec. 3.2.3).

As discussed in Section 2.1 computer simulation studies have followed the experimental approach, discussed above, to compute line tensions of droplets on solid surfaces [61–67]. The simulated line tensions in general involve either simple fluid droplets modeled with the Lennard-Jones potential or water droplets. In the latter case, for water droplets at a carbon surface, the reported line tensions vary in the range 1–100 pN. In several of these investigations the curvature dependence of the surface tension is omitted and the surface tension is assumed to be the same as for a flat interface. This is expected to be a

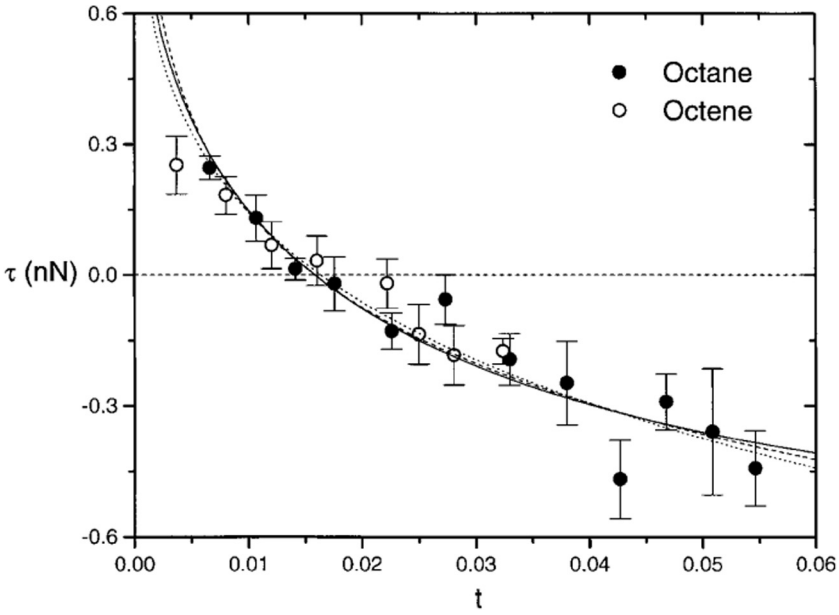

Fig. 19. Line tension τ for *n*-octane or 1-octene droplets on a hexadecyltrichlorosilane coated Si wafer near a first-order wetting transition. Reprinted (adapted) with permission from [9], © (1999) American Physical Society.

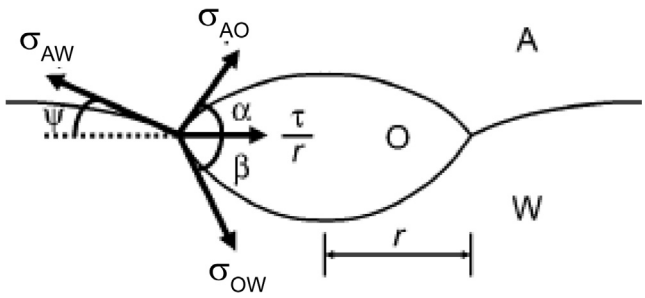

Fig. 20. Oil droplet (O) of lateral radius r at the air(A)/water(W) surface with interfacial tension σ_{ij}, between two phases i and j, and line tension τ. The angles α, β and ψ are defined in the figure.

good approximation for large droplets however, for small droplets with nanometer radii, this approximation should be treated with caution.

3.2.2. Liquid droplets at liquid surfaces

In the previous section, the influence of line tension on a liquid droplet on a molecularly smooth flat solid surface was examined. For liquid droplets on liquid surfaces (e.g., an oil droplet at the air-water surface), the situation is more complicated because of the curvature of the air-liquid surface. In this case, the line tension influences the angles α and β in Fig. 20 according to the Neumann-Young equation [122]

$$\sigma_{AO}\cos\alpha + \sigma_{OW}\cos\beta = \sigma_{AW} - \frac{\tau}{r} \tag{59}$$

where forces parallel to the air-water interface have been accounted for and it is assumed that the angle $\psi \approx 0$. The angles α and β, however, are difficult to measure independently. If these angles are sufficiently small, this equation can be transformed to [4]

$$\sigma_{AO}\cos\left(\frac{\sigma_{OW}\delta}{\sigma_{OW}+\sigma_{AO}}\right) + \sigma_{OW}\cos\left(\frac{\sigma_{AO}\delta}{\sigma_{OW}+\sigma_{AO}}\right) = \sigma_{AW} - \frac{\tau}{r} \tag{60}$$

by taking into account forces normal to the air-water interface where the dihedral angle $\delta = \alpha + \beta$.

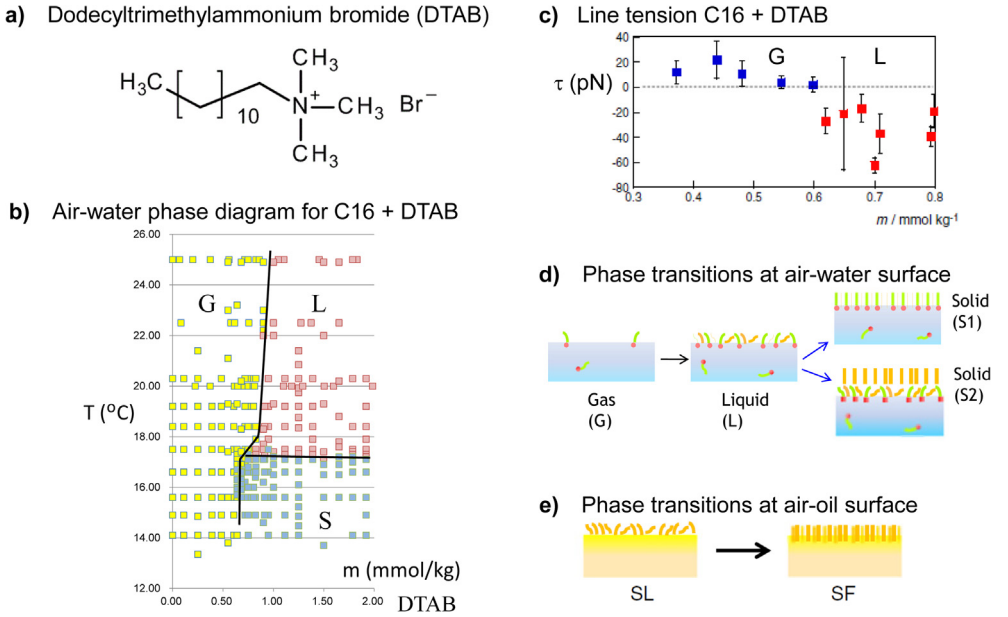

Fig. 21. (a) Chemical structure of cationic surfactant dodecyltrimethylammonium bromide (DTAB), (b) 2D surface phase diagram (molality m of DTAB versus temperature T) for a n-hexadecane oil droplet (C16) at the aqueous surfactant air surface showing the gaseous (G), liquid (L) and solid (S) phases. Reprinted (adapted) with permission from [22], © (2015) American Chemical Society. (c) Variation of line tension with DTAB molality m for the C16 + DTAB system at room temperature, (d) schematic of surface phase transitions that may occur at the air-water interface for varying surfactant concentrations and temperatures, (e) schematic surface phase transitions that may occur at the air-oil surface for varying surfactant concentrations and temperatures where SL (SF) denotes a surface liquid (frozen) state. Reprinted (adapted) with permission from [106], © (2014) Elsevier.

Matsubara and coworkers [106,123–125] used interferometry to measure the dihedral angle δ for n-alkane oil droplets at an aqueous surfactant air surface as a function of droplet radius r; thus, allowing the line tension to be determined using Eq. (60). They used the cationic surfactant alkyltrimethylammonium bromide (Fig. 21a) in their studies. This surfactant possesses a hydrophilic charged head group, which resides in the water phase, as well as, a hydrophobic alkyl tail, which avoids the water phase and protrudes into either the oil or air phase. Hence, this surfactant is found at both the water-air, as well as, water-oil interfaces. As the temperature T or surfactant molality m in the bulk water phase is changed, the two-dimensional (2D) surface film at the air-water surface can exist in either a 2D gaseous (G), liquid (L) or solid (S) state. Fig. 21b provides an example of this 2D surface phase diagram [22] for a n-hexadecane oil droplet (C16) in the presence of the surfactant dodecyltrimethylammonium bromide (DTAB) where the corresponding line tensions in the G and L phases, at room temperature, are shown in Fig. 21c [106]. The 2D film at the air-water interface adjoins the three-phase oil-water-air contact line and therefore has a significant influence on the line tension of this contact line. For example, the results in Fig. 21c demonstrate that when this 2D air-water film is in the G (L) phase the line tension is positive (negative). As discussed later in this section the sign of the line tension may significantly influence the macroscopic behavior of oil droplets at this aqueous surfactant air surface.

At lower temperatures when the 2D surface film freezes, this system develops considerable complexities because surface freezing transitions can occur at the air-water and/or air-oil interfaces depending upon the n-alkane and surfactant chain lengths. Matsubara and coworkers [106] have therefore conducted a systematic study of these effects as a function of both n-alkane and surfactant chain length. They studied the n-alkanes tetradecane (C14), hexadecane (C16) and octadecane (C18) and the alkyltrimethylammonium bromide surfactants DeTAB (C10S, which has an alkyl tail 10 carbons long), DTAB (C12S) and TTAB (C14S). These various choices give rise to differing surface phase transitions at either the water-air and/or oil-air interface. For sufficiently long n-alkane liquids ($n > 14$), the oil droplet undergoes a surface freezing transition at the oil-air surface from a surface liquid state (SL) to a surface frozen state (SF) [126] as the temperature is decreased below the surface freezing transition (Fig. 21e). The presence/absence of this surface freezing necessarily influences the line tension because the oil phase adjoins the three-phase oil-water-air contact line. By selectively choosing differing alkyl surfactant chain lengths, combined with differing n-alkane chain lengths, one can obtain differing solid phases at the water-air surface. For example, for sufficiently short surfactant and n-alkane chain length (eg. TTAB-tetradecane) the mixture alkane/surfactant film transitions from a monomolecular liquid state L to a *monomolecular* solid state (denoted S1 in Fig. 21d) at the air-water surface. However, if the n-alkane is sufficiently long (eg. DTAB-hexadecane) the air-water monomolecular mixed liquid state L now transitions to a *bilayer* solid state, denoted S2, which possesses a solid upper alkane monolayer atop a mixed liquid-like lower layer (Fig. 21d). For the DTAB-hexadecane system the SL → SF transition at the *oil-air surface* occurred at a similar temperature as the L → S2 transition at the *water-air surface*. Hence, it is difficult to separate out the effects of surface freez-

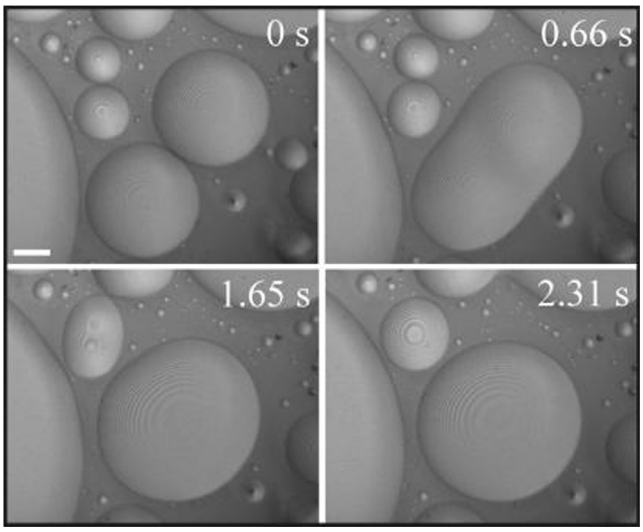

Fig. 22. Coalescence of n-hexadecane oil droplets in the G phase at an aqueous DTAB air surface. Scale bar = 100 μm. Reprinted (adapted) with permission from [22], © (2015) American Chemical Society.

ing at the oil-air surface from the liquid-to-bilayer solid transition happening at the water-air surface and the consequent influence on line tension behavior. Thus, another system was studied (DeTAB-octadecane) where surface freezing occurs at the oil-air surface in the absence of any liquid-to-solid transition at the water-air surface. The influence of these various solid surface phase transitions at both the oil-air and water-air surface and how they impact the line tension has recently been reviewed by Matsubara and coworkers [106] and will not be re-examined here.

A different aspect of this system is examined in the remainder of this section, namely, how the dynamics and stability of oil droplets at the aqueous-air surface are influenced by the *sign* of the line tension. As noted earlier, the line tension is positive (negative) in the G (L) phase (Fig. 21c) where an explanation for the sign of the line tension in the G and L phases is provided in Takata et al. [124]. Droplets always coalesce (fragment) in the G (L) phase. Ushijima et al. [125] have speculated that this coalescence/fragmentation behavior could be caused by the sign of the line tension.

Paneru et al. [22] have probed this coalescence and fragmentation behavior in more depth. Fig. 22 provides an example of coalescence in the G phase. For DTAB + hexadecane the liquid-air surface is approximately flat [117], hence, the theory developed in Sec. 3.2.1 is approximately valid and can be used to understand the observed experimental behavior. For coalescence, both the two smaller pre-coalescence droplets, as well as, the larger post-coalescence droplet must be mechanically stable. In other words, $d^2E/dr^2 > 0$ where the second energy derivative is given in Eq. (57b). This inequality is certainly true in the G phase because τ ($\sim$10 pN) is positive and S (~ -4 mN/m) is negative. A second condition for coalescence is that the total energy decreases upon coalescence where, at the same time, the total oil droplet volume must remain constant. This condition can be encapsulated using the energy difference [22]

$$\Delta E = E_1 - 2E_2 = \pi r_1[3(2^{1/3} - 1)Sr_1 - 4(2^{2/3} - 1)\tau]/2 \tag{61}$$

which is the difference in energy between the larger droplet of energy E_1, volume V_1 and radius r_1 and the two smaller droplets each of energy E_2 and volume $V_1/2$. Therefore, for coalescence, we additionally require that $\Delta E < 0$. As S is negative and τ is positive, in the G phase, this second requirement is also certainly valid. Additionally, as $|S|r \gg \tau$, the surface tension contribution is the primary component, which causes coalescence. In the G phase all oil droplets coalesce such that, at the end of the experiment, one single large oil droplet remains at the aqueous-air surface.

The L phase behavior for DTAB + hexadecane is rather complex (Fig. 23). The hexadecane oil droplet, when first deposited upon the aqueous-air surface in the L phase forms a rather flat oil droplet many millimeters in diameter with an oil film thickness of the order of $\sim$80 nm where the periphery of the oil droplet is decorated with "petals" composed of valleys of oil (Fig. 23a). With increasing time this oil droplet spreads to a much thinner oil film and holes nucleate in this oil film where the periphery of these holes is decorated with petals (Fig. 23b). The hole diameter grows linearly with time at a growth velocity of $\sim$117 μm/s (Fig. 23c). Eventually the holes expand to such a diameter that overlapping holes collide, which leads to the complete destruction of the oil film into much smaller oil droplets, now only a few hundred microns in diameter. These smaller oil droplets are unstable and fluctuate rapidly in time over time scales of a few seconds and they break up into smaller unstable and metastable droplets (Fig. 23d). Unstable droplets either have a "rubber raft" shape, with a thinner central film and a thicker outer rim (Fig. 23d, t = 2.5 s, right droplet), or a non-symmetric shape (Fig. 23e, upper inset). Metastable droplets possess a spherical cap-shape with circular interference rings (Fig. 23e, lower inset). The metastable droplets were used to measure the line tension, in the L phase (Fig. 21c), with use of the Neumann-Young equation [Eq. (60)]. Large

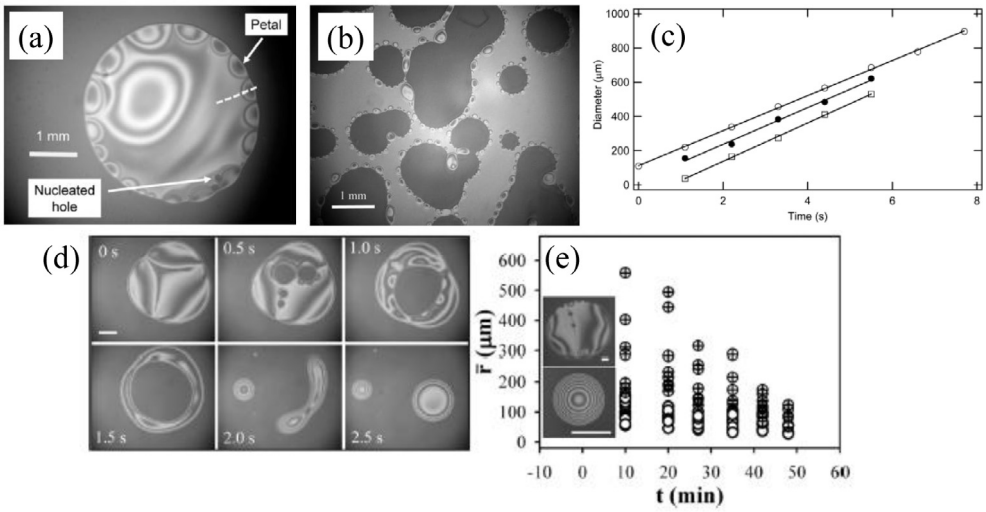

Fig. 23. Fragmentation behavior of hexadecane (C16) oil droplets at the aqueous DTAB air surface in the L phase. (a) Large ~3.5 mm diameter C16 droplet shortly after deposition. Oil "petals" decorate the three-phase contact line. (Scale bar = 1 mm.) (b) C16 droplet in (a) spreads to a thin oil film. (Scale bar = 1 mm.) Petal decorated holes nucleate in this oil film where these holes grow linearly with time as shown in (c). (d) Overlapping holes eventually destroy this oil film and the film breaks up into unstable fragmenting oil droplets. (Scale bar = 100 μm.) (e) Droplet distribution time evolution for unstable (upper inset, crossed circles, $r \geqslant 100$ μm) and metastable droplets (lower inset, open circles, $r \leqslant 100$ μm). Metastable droplets eventually sink further into the water medium, as described in the text. (Scale bar = 100 μm.) Reprinted (adapted) with permission from [22], © (2015) American Chemical Society.

unstable droplets (Fig. 23e, circles with plus signs) evolve over time into metastable droplets (Fig. 23e, circles) where droplets with average radii $\bar{r} > 100$ μm (< 100 μm) are unstable (metastable). Unstable droplets fluctuate rapidly on time scales of seconds (Fig. 23d), whereas, metastable droplets are stable over time scales of many minutes. However, metastable droplets eventually sink below the aqueous-air surface into the water phase. This sinking of droplets into the aqueous phase can be qualitatively understood from Eq. (57b), which defines a critical radius

$$r_{crit} = \frac{5\tau}{6S} \sim 80\ \mu\text{m} \tag{62}$$

with $d^2E/dr^2 = 0$. This estimate was determined using $\tau \sim -55$ pN and $S \sim -5.6 \times 10^{-4}$ mN/m in the L phase. Thus, spherical cap-shaped droplets with $r > r_{crit}$ are mechanically stable as $d^2E/dr^2 > 0$, however, this does not necessarily imply that spherical cap-shaped droplets possess the lowest energy state. The experimental results indicate that "petal shaped" droplets and "rubber raft shaped" droplets must possess a lower energy than spherical cap-shaped droplets. Spherical cap-shaped droplets with $r < r_{crit}$ are mechanically unstable, as $d^2E/dr^2 < 0$, and this will be the reason why the metastable droplets exhibited in Fig. 23e eventually sink into the aqueous liquid phase, driven by line tension effects. {This effect is exactly analogous to the existence of an R_{min} [Eq. (32)] for spherical colloidal particles at the liquid-air surface.} The density of hexadecane ($\rho_H = 0.77$ g/cm^3) is less than that of water ($\rho_W = 1.0$ g/cm^3), hence, although the surface and line tensions cause these droplets to sink into the water phase, this effect is counterbalanced by the buoyancy and gravitational forces whose net effect is to cause these oil droplets to float. Thus, the oil droplet at the aqueous-air surface is somewhat like an iceberg where only a little of the oil protrudes above the liquid surface into the air phase.

The calculations in Sec. 3.1.1, for a spherical particle at a liquid surface, allow one to estimate the protrusion height of the oil droplet into the air phase. As most of the oil is submerged below the water-air surface, this oil droplet can be approximated by a sphere of radius R. Eq. (28) determines the positioning of a spherical object at a liquid-vapor surface if surface and line tension terms are present. If the weight and buoyancy forces, acting on the particle, are included then Eq. (28) is modified to

$$\frac{dE}{dh} = \frac{dE}{d\theta}\frac{d\theta}{dh} = \sigma_{LV}\cos\theta_\infty 2\pi R + \tau 2\pi\cot\theta - \sigma_{LV}2\pi R\cos\theta - \rho_H g\frac{4}{3}\pi R^3 + \rho_W g V_L = 0 \tag{63}$$

where ρ_H and ρ_W are, respectively, the hexadecane and water densities while

$$V_L = \frac{4}{3}\pi R^3 - \frac{1}{3}\pi h^2(3R - h) \tag{64}$$

is the volume of the displaced liquid. A numerical solution of Eq. (63) gives $h \sim 0.4$ μm for a droplet of radius $R = 50$ μm where an estimate for $cos\theta_\infty$ is obtained from the spreading coefficient [Eq. (5b)] while h, R and $cos\theta$ are interrelated via Eq. (37). In this calculation we have assumed that $\rho_H = 0.77$ g/cm^3, $\rho_W = 1.0$ g/cm^3, $\tau = -55 \times 10^{-12}$ N [124], $S = -5.6 \times 10^{-4}$ mN/m [22], and $\sigma_{LV} = 71$ mN/m [117]. This estimate for h (~0.4 μm) agrees approximately with the

experimental observations for the sinking of an oil droplet into the water phase when $r < r_{crit}$ (see the movie "Disappearing single droplet" in Paneru et al. [22]). Note that Eq. (63) determines the mechanical equilibrium for a spherical droplet at the water-air surface in the presence of surface tension, line tension, buoyancy, and gravitational forces. The condition $d^2E/dh^2 = 0$ determines the minimum radius of the droplet R_{min} below which all droplets *detach* from the water surface and become *submerged* within the aqueous phase. Eq. (63), however, does not determine the ultimate size of this oil-in-water micelle (within the bulk water phase). Browne et al. [127] describe a simple model that determines the thermodynamic equilibrium micelle size taking into account surface tension, bending energy, and electrostatic effects.

Finally, before completing this section, we note that the contact angles of cylindrical nanodroplets at liquid-liquid interfaces have been investigated using molecular dynamics computer simulations [128]. The system was modeled using Lennard-Jones fluids, and the spreading of the droplets was investigated by systematically varying the interactions between the droplet and the liquid phases. Computed surface tensions and contact angles were used to test the Neumann triangle construction [53]. It was found that this construction reproduces accurately the spreading behavior inferred from the simulations, without the need for including line tension terms. The lack of an obvious line signature could be connected to the small value of this quantity. The line tension of the non-deformable nanoparticles adsorbed at Lennard-Jones fluid interfaces is of the order of *pN*. From the Neumann-Young equation [Eq. (59)], the influence of the line tension can be estimated by considering $1 - \tau/(r\sigma_{AW})$. For $\tau \sim pN$, $r \sim 1$ nm, and $\sigma_{AW} \sim 20$ mN/m we obtain $\tau/(r\sigma_{AW}) = 0.05$, which is a small correction, and therefore this explains the good agreement between the simulated contact angles and the Neumann construction. It would be very interesting to explore other interfaces (e.g. carbon-water), which involve different type of interactions, and for which larger estimates of the line tension (10–100 pN) have been reported [64–67].

3.2.3. Critique on liquid droplets at surfaces: negative line tensions and contact line stability/instability

In Sec. 3.2.1 the line tension for small (6–30 μm radii) n-octane or 1-octene droplets on a solid surface were observed to change from a negative line tension to a positive line tension on approaching a first-order wetting transition (Fig. 19). These observations confirm the first-order wetting predictions in Sec. 2.3. However, other theoretical predictions in Sec. 2.3 for (i) the variation in the boundary tension on approaching a prewetting transition (Fig. 9) and (ii) the variation in the line tension on approaching a critical wetting transition (Fig. 10) still remain untested.

Sec. 3.2.2 summarizes experimental observations for oil droplets at an aqueous surfactant air surface. In Sec. 3.2.2, oil droplets possessing a positive line tension are stable and coalesce as a function of time (Fig. 22). This behavior should be contrasted with oil droplets possessing a negative line tension. Two types of behavior were observed for negative line tension droplets (Fig. 23e): (a) sufficiently large droplets with average lateral radius $r > 100$ μm were unstable, exhibited "petal" or "rubber raft" shapes and fragmented into smaller droplets, whereas, (b) smaller droplets ($r < 100$ μm) were metastable and eventually sunk into the water medium with only a little of the oil droplet protruding above the water surface where surface tension, line tension, gravitational, and buoyancy forces must be taken into account.

As eluded to earlier (Sec. 1), there has been considerable debate in the theoretical literature as to whether or not a negative line tension can lead to an instability in the three-phase droplet contact line [28,40–44]. Droplets possessing a negative line tension were observed in both Secs. 3.2.1 and 3.2.2. Are these observations consistent with theory? In Eq. (57) the second energy derivative for a spherical cap shaped droplet on a flat surface was determined. This second energy derivative only provides information about the stability of the droplet as a whole, relative to this droplet being submerged in one or other of the bulk phases. In order to understand the stability of the three-phase contact line of a liquid droplet one must consider the second variation of the energy. Rosso and Virga [26] and Brinkmann, Kierfeld and Lipowsky [27] have used the second energy variation to study contact line stability for liquid filaments on a solid substrate where there are regions of stability, as well as, regions of instability when the line tension is negative. Of relevance to the current review, in this regard, is the work of Guzzardi, Rosso and Virga [29] who studied three-phase contact line stability for spherical cap shaped droplets on a solid surface. Fig. 24 is taken from this publication (their Fig. 7) which plots $-\log_{10}|\tau^*|$ versus $\cos\theta_\infty$ where the reduced line tension

$$\tau^* = \frac{\tau}{\sigma_{LV}\sqrt[3]{3V/\pi}} \tag{65}$$

and the lines are residual stability curves with index from $m_{rs} = 2$ (lower curve) to 100 (upper curve) for droplets possessing a negative line tension. The higher the residual stability index, the more stable is the droplet to sinusoidal perturbations of the three-phase contact line. The pluses are experimental data from Wang, Betelu and Law [10] for negative line tension n-octane droplets on a hexadecyltrichlorosilane coated silicon wafer at various temperatures approaching a first-order wetting transition (Sec. 3.2.1 and Fig. 19 in this review). Most of this data lies near a curve with residual stability index $m_{rs} = 50$, hence, these droplets are highly stable to sinusoidal fluctuations of the three-phase contact line.

One might wonder whether or not this contact line instability theory of Guzzardi, Rosso and Virga [29] can qualitatively explain the experimental observations in Fig. 23e where droplets with radii $r > 100$ μm ($r < 100$ μm) are unstable (metastable)? In applying the Guzzardi, Rosso and Virga theory one must keep in mind that their theory is strictly applicable only for liquid droplets situated upon a solid substrate, whereas, the data in Fig. 23e is for an oil droplet at the aqueous-air surface (where this surface is almost flat). We will ignore this technicality here. For this system, $S = -5.6 \times 10^{-4}$ mN/m, $\sigma_{OW} = 30$ mN/m, and $\tau = -55$ pN, therefore,

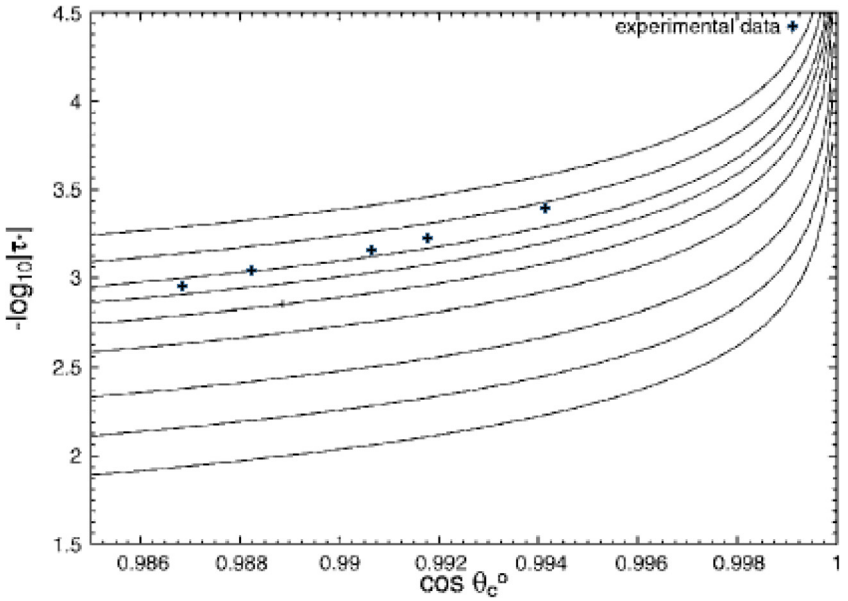

Fig. 24. Stability diagram for liquid droplets on a solid substrate where τ^* is the reduced line tension [Eq. (65)] while the lines correspond to a residual stability index m_{rs} of 2 (lower curve), 5, 10, 20, 30, 40, 50, 70 and 100 (upper curve). The pluses are from experimental data for n-octane droplets on a silane-coated substrate [10]. Reprinted (adapted) with permission from [29], © (2006) American Physical Society.

$$\cos\theta_\infty = 1 + \frac{S}{\sigma_{OW}} \approx 0.99998, \tag{66}$$

the reduced line tension

$$\tau^* = \frac{\tau}{\sigma_{OW}\sqrt[3]{3V/\pi}} = -5.3 \times 10^{-5} \tag{67}$$

for droplets with a radius $r \sim 100$ μm and height $h \sim 2.3$ μm, hence

$$-\log_{10}|\tau^*| \approx +4.3. \tag{68}$$

Eqs. (66) and (68) would correspond to a point lying approximately on the unstable-residual stable boundary on Fig. 24. At fixed $cos\theta_\infty$, if the volume V is increased then $-log_{10}|\tau^*|$ also increases. Hence, the Guzzardi, Rosso and Virga theory seems to indicate that larger droplets are more stable than smaller droplets, which disagrees with the observations in Fig. 23e. The reason for this discrepancy between the Guzzardi, Rosso and Virga theory and experiment is not understood at this time.

A phenomenological theory of Clarke [40,41] considers sinusoidal perturbations of the three-phase contact line, in a manner similar to Guzzardi, Rosso and Virga [29]. The Clarke theory qualitatively explains the contact line instabilities observed in Fig. 23, as described below. Clarke considers sinusoidal contact line fluctuations at a three-phase contact line consisting of either two fluid phases and a solid phase [40], or, three fluid phases [41]. Although the later work [41], involving three fluid phases, is more consistent with the experimental geometry actually used in Sec. 3.2.2 (Fig. 20), this geometry involves experimental parameters which are more difficult to assess. Therefore, akin to the approximation used in Fig. 17b, the earlier Clarke publication [40] (for two fluid phases and a solid phase) is used to estimate the contact line fluctuation wavelengths which are unstable. A contact line fluctuation of wave vector q and amplitude η_q possesses an energy

$$W(q) = W_\tau + W_\sigma + W_g = \frac{1}{2}|\eta_q|^2\sigma_{OW}\theta_\infty^2[\lambda_\tau|q|^2 + |q| + \lambda_g^{-2}|q|^{-1}], \tag{69}$$

where W_τ, W_σ, and W_g are the energies that arise from, respectively, line tension, fringe elasticity [50], and gravitational contributions. Here

$$\lambda_\tau = \frac{\tau}{\sigma_{OW}\theta_\infty^2} \tag{70a}$$

and

$$\lambda_g = \left(\frac{2\sigma_{OW}}{g\Delta\rho}\right)^{1/2}. \tag{70b}$$

Therefore, for a negative line tension τ, fluctuations possessing sufficiently large wave vectors q are unstable and grow because $W(q)$ is negative. [When $W(q)$ is negative, it is energetically favorable to make the amplitude of this fluctuation (η_q) larger because this decreases the overall energy of the system.] As a first approximation, ignoring the gravitational term, there is a critical wave vector

$$|q_{crit}| \equiv \frac{2\pi}{\lambda_{crit}} = -\lambda_\tau^{-1} \tag{71}$$

above which all wave vectors are unstable. Hence, for $\tau = -55$ pN, $S = -5.6 \times 10^{-4}$ mN/m, and $\sigma_{OW} = 45$ mN/m, the critical wavelength $\lambda_{crit} \approx 300$ μm. This critical wavelength is of order the size of the instabilities observed in Fig. 23a and Fig. 23d ($t = 0$ s). Wavelengths λ less than λ_{crit} are unstable (i.e. q larger than q_{crit} are unstable) and the Clarke theory therefore also qualitatively explains the appearance of petals at hole boundaries in Fig. 23b. Inclusion of the gravitational term in Eq. (69) does not significantly alter the magnitude of the critical wavelength λ_{crit}. Unfortunately, a quantitative comparison between experiment and theory is not yet possible because the Clarke theory [40] only considers the *energy* of a fluctuation of wavevector q, where *all* wavevectors q greater than q_{crit} are unstable (and grow). This theory needs to be extended to include fluid transport where this fluid motion is opposed by the fluid viscosity; a "fastest" growing wavevector q_{fast} ($>q_{crit}$), possessing a characteristic time scale, would then arise to dominate the three-phase contact line instability (in analogy to the considerations of Vrij [129] and Vrij and Overbeek [130] who examined the instability process that occurs in thin film rupture). The differing theoretical approaches of Clarke [40,41] and Guzzardi, Rosso and Virga [29] provide valuable insights into how sinusoidal perturbations of the three-phase contact line give rise to a contact line instability when the line tension is negative. An examination of the interconnection, similarities, and differences between these two theoretical approaches would prove useful.

3.3. Droplet nucleation at surfaces

3.3.1. Nucleated wetting

If $\sigma_{SV} > \sigma_{SL} + \sigma_{LV}$ then, at equilibrium, a surface is covered by an equilibrium liquid wetting layer of thickness l_w given by Eq. (17b) where the interfacial potential $V(l)$ is depicted in Fig. 5c. If the system initially starts in the metastable SV state, how does this system evolve to the equilibrium wetting layer? The system must first nucleate droplets at the surface. These droplets eventually coalesce into a liquid layer of thickness l. If $l < l_w$ then one will observe layer growth with time (Fig. 25a) [131]. If, however, $l > l_w$ then this liquid layer must undergo a hydrodynamic instability to reduce its thickness to l_w [132].

The surface nucleation process, at a metastable surface, invariably involves the line tension τ. Law [13,133] studied this surface nucleated wetting process using a critical binary liquid mixture of the two liquids, acetone and hexadecane. This mixture was prepared at the critical composition, which has a hexadecane volume fraction $v_c \approx 0.5$ and critical temperature $T_c = 31.1$ °C. For $T > T_c$ the system is in the one-phase region where acetone and hexadecane are completely miscible. As the temperature T is lowered below T_c the system undergoes a bulk second-order phase transition at T_c and phase separates out into a lighter hexadecane-rich α phase and a heavier acetone-rich β phase. If $T_c > T > T_w$ then, at equilibrium, one will find a β wetting layer at the α-air (αv) surface (Fig. 25b).[1] In order to study the formation of this equilibrium wetting layer, the system was first prepared 10 mK above T_c and then quenched to various temperatures T below T_c, but above the wetting transition temperature T_w. The system phase separates into bulk α and β phases (Fig. 25b) with compositions governed by the reduced temperature $t = (T_c - T)/T_c$. The αv surface is in a metastable ("critical adsorption") state [133] and it remains in this state until a β droplet nucleates at this surface at an incubation or nucleation time T_N. In order to study this surface nucleation process a focused laser beam was reflected off this liquid-air surface and the ellipticity $\bar{\rho}$ was measured. For a uniform film $\bar{\rho}$ provides a measure of the film thickness l. If the surface is decorated with droplets then $\bar{\rho}$ will be very noisy. Fig. 26a and b provide two examples of $\bar{\rho}$ measured as a function of time. In Fig. 26a the system has been quenched 0.013 °C below T_c, into the two-phase region; the surface remains in the metastable critical adsorption surface state until the nucleation time T_N. After time T_N the film thickens continuously where at late times it saturates to a constant film thickness. Rather differing behavior can be observed in Fig. 26b where the system has been quenched 0.668 °C into the two phase region. The systems remains in the metastable critical adsorption state until time T_N (region A). At T_N droplets nucleate on the surface and the ellipticity becomes very, very noisy (region B). At late times these droplets coalesce into a uniform film (region C) and, thus, $\bar{\rho}$ settles down to a constant value. In Fig. 26c the nucleation time T_N is plotted as a function of reduced temperature t for many different quench experiments. In order to interpret this T_N data one must have a model for the surface nucleation process.

The energy for this nucleated droplet is given approximately by [13]

$$E \approx -S\pi r^2 + \tau 2\pi r + A\pi r^2/h^2 + \Delta\rho g H V \tag{72}$$

The first two terms on the right are the well-known surface and line tension contributions while the third and fourth terms are, respectively, a van der Waals estimate and gravitational contribution where H is the height at which the β droplet is above the bulk β phase (i.e. vertical height of α phase). Here $\Delta\rho = \rho_\beta - \rho_\alpha$ is the difference in densities between the β and

[1] The phase diagram for a critical binary liquid mixture is completely analogous to the phase diagram for a critical liquid mixture (Fig. 3a) except that the density ρ is replaced by the volume fraction v of one of the components of the critical binary liquid mixture [73].

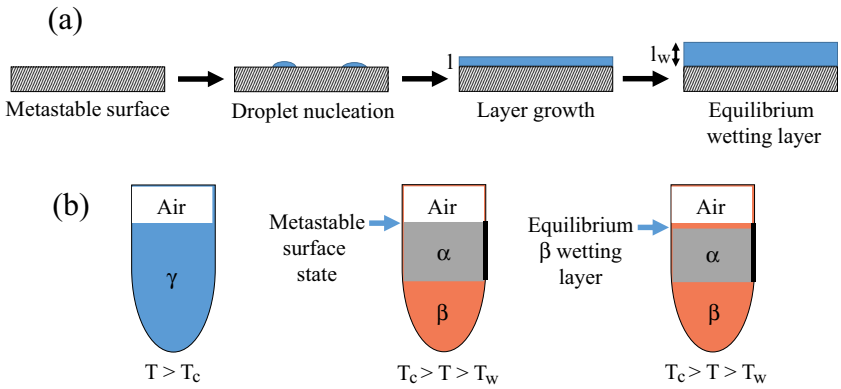

Fig. 25. (a) Schematic evolution of an equilibrium wetting layer on a surface. Droplets nucleate on a metastable surface, coalesce to a layer which then thickens to its equilibrium thickness l_w. (b) In practice, a metastable surface state can be prepared as follows. At a temperature above the critical temperature T_c, a critical binary liquid mixture exists in the one phase region γ (left). This system is quenched into the two phase region, with α and β phases, but above the wetting transition temperature T_w. The surface of this system is metastable (middle). At equilibrium, the surface in contact with the air, evolves to an equilibrium wetting layer with composition β (right).

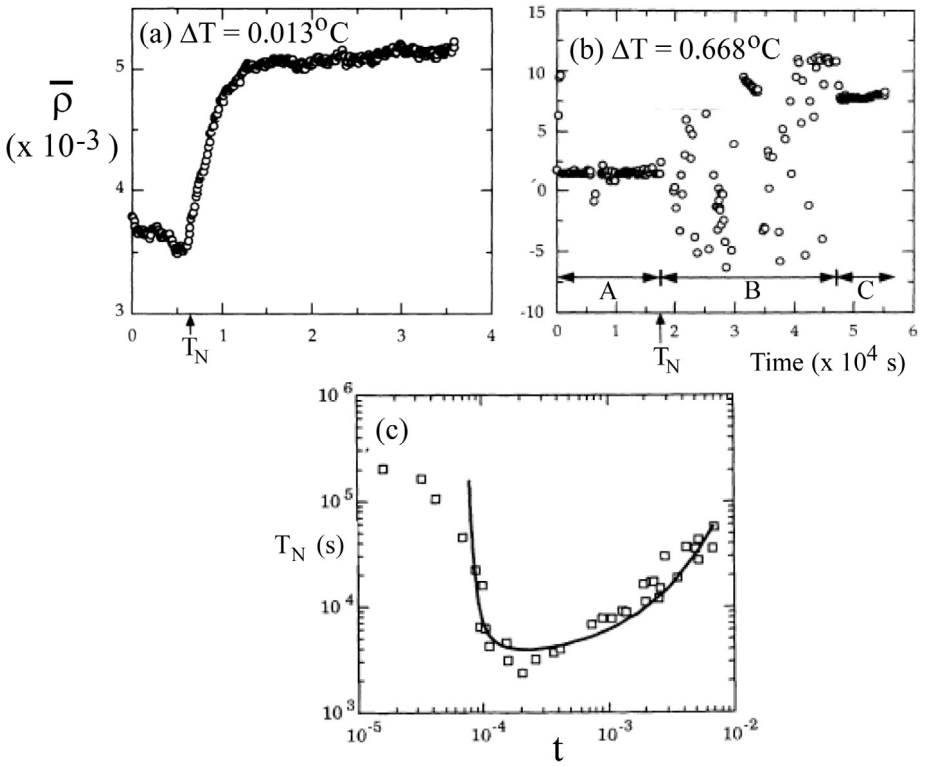

Fig. 26. Nucleated wetting of a critical acetone-hexadecane mixture. (a) Ellipticity $\bar{\rho}$ from the liquid-vapor surface as a function of time. The system is quenched (at time 0 s) from the one-phase into the two-phase region to a temperature $\Delta T = T_c - T = 0.013$ °C below T_c. At nucleation time T_N a uniform film nucleates and grows. Reprinted (adapted) with permission from [133], © (1992) American Physical Society. (b) Corresponding behavior for a quench to a temperature 0.688 °C. A = metastable critical adsorption surface state, B = surface droplets at liquid-air surface, C = droplets have coalesced to a uniform wetting film. (c) Plot of nucleation time T_N versus reduced temperature $t = (T_c - T)/T_c$. Reprinted (adapted) with permission from [13], © (1994) American Physical Society.

α phases while the Hamaker constant A occurred previously in Eq. (9a). Eq. (72) is very similar to Eq. (51) except that in Eq. (72) we have assumed that h is very small because the nucleating droplet is in the wetting region (where the contact angle will be exceptionally small). Of course Eq. (51) describes a macroscopic droplet and, therefore, the van der Waals term can be neglected. For nanoscopic nucleated droplets [Eq. (72)] including a van der Waals term is necessary in order to capture all of the essential physics. The volume of this droplet can be approximated as

$$V \approx \pi r^2 h/2 \tag{73}$$

which corresponds to Eq. (47) with the approximation that $h \ll r$. The analysis for nucleating droplets necessarily closely follows the analysis in Sec. 3.2.1 (for liquid droplets on a solid surface). For a given droplet volume V, the droplet will change its shape at constant V so that the droplet is in mechanical equilibrium and possesses the minimum energy. Hence,

$$dE/dr = 0 \tag{74}$$

where, together with $dV = 0$, from Eqs. (72) and (73) leads to

$$\tau/r - S + 3A/h^2 = 0. \tag{75}$$

Eq. (75) describes how the presence of a line tension τ changes the shape of this nucleating droplet. This equation is completely equivalent to the modified Young's equation [Eq. (52)] for $h \sim 0$ together with a van der Waals contribution. It is important to note that the van der Waals interaction plays a central role in this nucleation process because, as h is small, the van der Waals contribution in Eq. (72) will be large. Any droplet nucleation calculations, which omit this van der Waals interaction term, exclude an essential component of the physics. Various limiting forms of Eq. (75) have appeared in the literature in the past. For example, if $A = 0$, then Eq. (75) reduces to the two-dimensional analogue of the Laplace equation [134,135] which we have already encountered in Eq. (6). By contrast, if $\tau = 0$ in Eq. (75), then the droplet thickness

$$h = \sqrt{\frac{3A}{S}} \tag{76}$$

which has been used to estimate the thickness of mesa shaped droplets spreading upon a surface [50].

Determination of the nucleation time T_N follows from Eqs. (72), (73), and (75). We sketch the essential ideas behind the calculation here where the details are given in Law [13]. Eq. (73) can be used to eliminate r from Eq. (72) so that E can be expressed as a function of h and V, namely, $E(h,V)$. Similarly, but mathematically this is more complicated, Eq. (75) can be used to eliminate h from this equation, thus, now $E(V)$. Physically, $E(V)$ represents the minimum energy for that particular volume V because of the use of Eq. (75). In classical nucleation theory there is a critical volume V_c above which droplets grow (i.e. for $V > V_c$, $dE/dV < 0$) and below which droplets evaporate (i.e. for $V < V_c$, $dE/dV > 0$). Hence, the critical volume V_c is determined by the condition that

$$\left.\frac{dE(V)}{dV}\right|_{Vc} = 0. \tag{77}$$

Eqs. (6) and (7) in Law [13] provide a rather complicated expression for V_c. The energy to nucleate a droplet of volume V_c is therefore determined by substituting this expression for V_c into $E(V)$, specifically,

$$E(V_c) = \frac{\pi \tau_0^2 t^{2x-\beta}}{S_O(t^{\beta_1-\beta} - C_O)} \tag{78}$$

where C_o is a constant given in Law [13], $t = (T_c - T)/T_c$ is the reduced temperature, β (~0.33) and β_1 (~0.83) are critical exponents, while τ_o and x are the amplitude and critical exponent for the line tension. Namely, in Eq. (78) it has been assumed that $\tau = \tau_o t^x$ and $S = S_o t^{\beta_1}$ and, actually, the experimental nucleation data discussed below cannot be explained without these assumptions. The probability for nucleating a droplet of volume V_c is therefore given by

$$p \sim \exp[-E(V_c)/k_B T] \tag{79}$$

where $k_B T$ is the thermal energy at temperature T with k_B the Boltzmann constant. The nucleation time measured in experiments $T_N \sim 1/\mathrm{p}$ and, hence,

$$T_N = A_o \exp[E(V_c)/k_B T] \tag{80}$$

where A_o is a fitting constant (proportional to the inverse attempt frequency for nucleation). The solid line in Fig. 26c is a best fit to the experimental T_N data where $\tau_o \sim 1$ pN and $x = 0.76 \pm 0.02$. The amplitude of the line tension τ_o agrees with theoretical expectations (Sec. 2.3). The value of the critical exponent x still needs a theoretical explanation.

The nucleation of droplets at a surface can occur via either homogeneous or heterogeneous nucleation. In homogeneous nucleation the nucleation process is induced by the underlying thermal fluctuations present in all systems at a finite non-zero temperature T. Heterogeneous nucleation originates from some other system dependent process which influence the attempt rate A_o in Eq. (80). Law and Pak [136] have demonstrated that a small transverse gradient $\nabla T \sim$ mK/cm, which in practice is extremely difficult to eliminate, is the cause for the heterogeneous nucleation of surface droplets. Small transverse thermal gradients give rise to convective flow in the α phase of Fig. 25b, thus, transporting small nuclei of the β phase to the air-liquid surface which in turn influences the attempt rate A_o. Law and Pak [136] found that $A_o \sim (\nabla T)^{-1}$, which supports the idea that it is the surface flow with velocity $v \sim \nabla T$ which is inducing this heterogeneous surface nucleation process.

3.3.2. Critique on the nucleation route to line tension

Blossey and Bausch [137–140] and Blokhuis [134] have considered the nucleation of droplets at a metastable surface from a theoretical perspective. Their considerations are similar to those presented in Sec. 3.3.1 although not necessarily with all of the energy terms considered therein. Interested readers should refer to these authors for their perspective on the nucleation route to line tension.

A line tension contribution has been used to explain the experimental nucleation results for a number of other systems. Hienola et al. [141] studied the heterogeneous nucleation of n-nonane, n-propanol, and their mixtures on silver particles possessing radii in the range 3–13 nm. Their experimental results were explained using classical nucleation theory supplemented with a line tension term. The line tension was negative for all particle sizes varying from $\tau \sim -0.1$ pN, for the smallest particles, and increasing to $\tau \sim -0.4$ nN, for the largest particles. Guillemot et al. [30] studied the drying dynamics of hydrophobic cylindrical porous silica material with radii 1–2 nm filled with liquid water under high pressure. The pores empty when the pressure is lowered. The drying pressure is interpreted via thermally activated vapor bubble nucleation where a line tension is required to quantitatively explain the experimental data with $\tau \sim -0.3$ nN. The presence of a line tension, of this magnitude, may explain the high stability of nanobubbles at the interface between water and a hydrophobic surface [30].

4. Gravitational line tension contribution for millimeter-sized droplets

Perhaps the greatest controversy in this field is the observation of very large *positive* line tension values $\tau_{grav,expt} \sim 1$ μN, measured by Neumann and coworkers [121,142–146] and Drelich and Miller [147,148] (see David and Neumann [38] for a summary), which are at least 4 orders of magnitude larger than the largest values predicted via mean field theory, where $|\tau_{vdW,th}| \sim 1$–100 pN (Sec. 2.1). The line tension subscripts, in the previous sentence, denote the (perceived) origins for each of these line tension contributions. The mean field estimates for the line tension $\tau_{vdW,th}$ originate via consideration of surface tension and van der Waals interactions in the vicinity of an interface (Sec. 2.3). $\tau_{grav,expt}$ has been measured for large millimeter-sized liquid droplets on a solid surface. At such length scales, of order the capillary length $\kappa^{-1} \sim 1$ mm [Eq. (1)], the gravitational potential should be included within the line tension calculation.

De Gennes, Brochard-Wyart and Quéré [50] have estimated the gravitational contribution to the line tension τ_{grav} for liquid *puddles* on a solid substrate using a generalization of the "gradient-squared approximation" [149] contained in Eq. (22). In this generalization, valid for arbitrary sloped droplets, the line tension functional for liquid puddles is

$$\hat{\tau}[l(x)] = \int_{-\infty}^{\infty} dx \left[\sigma_{LV} \left(\sqrt{1 + (dl/dx)^2} - 1 \right) + \frac{1}{2} \rho g (e - l(x)) \right] \tag{81}$$

where the gravitational interaction has been included, whereas, the van der Waals interaction has been omitted (as this later contribution is negligible at millimeter length scales). Here, ρ is the liquid density, g the acceleration due to gravity, and e is the thickness of the puddle. [In the limit of small droplet slopes, $dl/dx \ll 1$, Eq. (81) reverts to the gradient-squared approximation of Eq. (22).] Minimization of Eq. (81), with respect to $l(x)$, provides an estimate for τ_{grav}

$$\tau_{grav}(puddle) = \frac{4}{3} \sigma_{LV} \kappa^{-1} \left(1 - \cos^3 \frac{\theta_\infty}{2} \right) \sim +10 \text{ μN}. \tag{82}$$

However, $\tau_{grav}(puddle)$ should *not* be compared with $\tau_{grav,expt}$, mentioned above, which was measured for ~1–5 mm radii sessile droplets on a solid surface, as these liquid droplets are not strictly puddles. One can obtain an estimate for $\tau_{grav}(droplet)$ by incorporating the gravitational contribution into the squared-gradient expression for the line tension [Eq. (23a)]. Specifically, in this case, the gravitational surface potential [150,151]

$$V_{grav}(droplet) = -S + \frac{1}{2} \rho g l^2 \tag{83}$$

and, therefore, Eq. (23a) becomes

$$\tau_{grav}(droplet) = \sqrt{2\sigma_{LV}} \int_0^{l_{\max}} \left[\sqrt{-S + \frac{1}{2} \rho g l^2} - \sqrt{-S} \right] dl \tag{84a}$$

$$= \kappa^{-1} \rho g l_{\max}^2 C \tag{84b}$$

where the constant of integration

$$C = \frac{1}{2} \sqrt{1 + a^2} + \frac{1}{2} a^2 \ln \left| \frac{1 + \sqrt{1 + a^2}}{a} \right| - a \tag{85}$$

with

$$a^2 = -\frac{2S}{\rho g l_{\max}^2} = 2(1 - \cos \theta_\infty) \left(\frac{\kappa^{-1}}{l_{\max}} \right)^2. \tag{86}$$

Eqs. (1) and (5b) have been used in deriving Eq. (86). Thus, from Eq. (84b),

$$\tau_{grav}(droplet) \sim +10\ \mu N \tag{87}$$

where the capillary length $\kappa^{-1} \sim 1$ mm, droplet height $l_{max} \sim 1$ mm, density $\rho \sim 1$ g/cm^3 and $C \sim 1$ were used in obtaining this estimate.

This squared-gradient estimate for $\tau_{grav}(droplet)$ [Eq. (84b)] is strictly valid only when $dl/dx \ll 1$. This result is in need of generalization to arbitrary dl/dx [akin to Eq. (81)], as the line tension experimental measurements for millimeter-sized droplets, in general, possess large contact angles ($\theta_\infty \sim 90°$). It would be surprising if such a generalization to arbitrary dl/dx changed the order of magnitude of $\tau_{grav} \sim +10\ \mu N$ [Eqs. (82) and (87)] significantly. We note that $\tau_{grav}(droplet)$ [Eq. (84b)] is strictly positive, in agreement with experiments for $\tau_{grav,expt}$. $\tau_{grav}(droplet) \sim +10\ \mu N$ is closer in magnitude to the experimental values measured for millimeter-sized droplets ($\tau_{grav,expt} + 1\ \mu N$) compared with $\tau_{vdW,th}$, however, $\tau_{grav}(droplet)$ and $\tau_{grav,expt}$ still differ by an order of magnitude. We believe this discrepancy may arise from the experimental determination of $\tau_{grav,expt}$ where the authors have used the modified Young's equation given in Eq. (56a) to determine $\tau_{grav,expt}$. Eq. (56a) is strictly valid only for liquid droplets much smaller than the capillary length κ^{-1} [Eq. (1)] where the gravitational energy can be ignored. For large millimeter-sized liquid droplets a gravitational energy should be added to Eq. (44) and the energy minimized. Shapiro et al. [152] have partially carried out this calculation (in the absence of a line tension term and assuming spherical cap shaped droplets). They find that

$$\cos\theta = \cos\theta_\infty - \frac{\rho g R^2}{\sigma_{LV}}\left[\frac{\cos\theta}{3} - \frac{\cos 2\theta}{12} - \frac{1}{4}\right] \tag{88}$$

where R is the radius of the liquid-vapor surface of the droplet. This equation needs to be generalized to include a line tension contribution. A likely generalization is

$$\cos\theta = \cos\theta_\infty - \frac{\rho g R^2}{\sigma_{LV}}\left[\frac{\cos\theta}{3} - \frac{\cos 2\theta}{12} - \frac{1}{4}\right] - \frac{\tau}{\sigma_{LV} r} \tag{89}$$

obtained by combining Eqs. (56a) and (88). Ansatz Eq. (89) reproduces the correct limits when either $g \to 0$ or $\tau \to 0$. The experimental contact angle data for millimeter-sized droplets should be compared with Eq. (89) in order to deduce the line tension τ. However, in doing so, one must keep in mind that Eq. (89) assumes that the spherical cap approximation is valid. Ideally one should derive the correct modified Young's equation for millimeter-sized droplets in the presence of surface tension, line tension, as well as, gravitational contributions without assuming a spherical cap approximation [35].

5. Summary and discussion of line tension effects

This review summarizes our views on the line tension, or, energy per unit length associated with three-phase contact lines, specifically, solid-liquid-vapor and liquid-liquid-vapor contact lines. The traditional view has been that the line tension arises from a functional minimization of surface tension and van der Waals interactions in the vicinity of a three-phase contact line (Sec. 2.3). Such a minimization leads to a line tension of magnitude $|\tau_{vdW}| \sim 1$–100 pN which is important on nanometer length scales. Although a number of experiments have found line tension magnitudes in agreement with these theoretical estimates, numerous other experiments measured significantly larger line tension magnitudes, sometimes, many orders of magnitude larger. This disagreement between theory and experiment has led to significant controversy and debate concerning the reliability of many line tension measurements. Computer simulation studies have also reported values in this range (1–100 pN). Most of the computer simulation data, for nanoparticles at fluid interfaces and droplets at solid surfaces, are in the range 1–10 pN. Larger computer simulation values of up to ~100 pN have been reported for water droplets at a carbon surface.

Recent work, as summarized in this review, indicates that the line tension is far more complex and interesting than this traditional view point. Differing physical phenomena, at differing length scales, contribute to the line tension. At atomic length scales, the re-orientation and re-organization of sub-molecular groups, in order to minimize their energies in the vicinity of a three-phase contact line, contribute to the line tension. This contribution is expected to be particularly important if dissimilar surfaces meet at a three-phase contact line. Atomic force microscopy experiments provide evidence for this atomic scale contribution to the line tension where the magnitude of this contribution $|\tau_{atom}| \sim 1$ nN (Secs. 3.1.1 and 3.1.3). As far as the authors are aware, no theoretical studies of these sub-molecular contributions to the line tension are currently available. If similar surfaces meet at a three-phase contact line then τ_{atom} is expected to be unimportant and the van der Waals contribution to the line tension τ_{vdW}, at nanometer length scales, is expected to play the dominant role provided that the object under study is not too large. τ_{vdW} can be of either sign, determined by the shape of the interfacial potential (Sec. 2.3). For large objects of order the capillary length $\kappa^{-1} \sim 1$ mm [Eq. (1)], the gravitational contribution τ_{grav} (~1–10 μN), which is always positive, dominates the line tension (Sec. 4). Provided that each line tension contribution is independent, the total line tension is

$$\tau_{tot} = \tau_{atom} + \tau_{vdW} + \tau_{grav}. \tag{90}$$

Table 1
Line tension contributions.

	Magnitude τ	Sign τ	Length scale of phenomena	Line tension length, $\xi = \tau/\sigma$	Review sections
Atomic, τ_{atom}	~1 nN		~0.1 nm	$\sim 10^{-7}$ m	3.1.1, 3.1.3
Van der Waals, τ_{vdW}	~1–100 pN	+ or −	~1–100 nm	$\sim 10^{-9}$ m	2.3, 3.1.2, 3.3.1
Gravity, τ_{grav}	~1–10 μN	+	~1 mm	$\sim 10^{-4}$ m	4

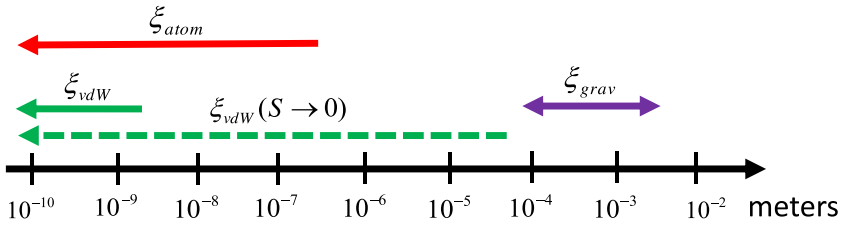

Fig. 27. Pictorial representation of the line tension length ξ [Eq. (2)] for the atomic ξ_{atom}, van der Waals ξ_{vdW}, and gravitational ξ_{grav} contributions to the line tension (solid arrows), far from a wetting transition. Near a wetting transition the "spreading coefficient" line tension length, defined in Eq. (6), must be used and, under these circumstances for example, the van der Waals line tension length $\xi_{vdW}(S \to 0)$ may become very large (dashed line).

Table 1 provides a summary of these various line tension contributions, including their magnitude and sign, the length scale of the respective physical phenomena, as well as, the "line tension length" $\xi = |\tau/\sigma|$ [Eq. (2)] below which the line tension will play a significant role. In this estimate for ξ it is assumed that the surface tension $\sigma \sim 20$ mN/m. Fig. 27 (solid lines) provide a pictorial overview for the various spatial scales at which the line tension lengths ξ_{atom}, ξ_{vdW}, and ξ_{grav} are expected to be important. It is therefore perhaps not so surprising that line tension effects of differing magnitudes (Table 1) measured over many different length scales (Fig. 27) have been observed. One should keep in mind that the line tension length ξ estimates, contained in Table 1, are strictly valid only if one is far from any wetting transition. Near a wetting transition the "spreading coefficient" line tension length $\xi_S = |\tau/S|$ [Eq. (6)] must be used. For example, when $S \to 0$ (eg. $\theta_\infty \sim 1°$ then $S \sim -3$ μN/m), the van der Waals line tension length may become very, very large, as depicted by the dashed line in Fig. 27 [$\xi_{vdW}(S \to 0)$].

A coherent picture of the three-phase line tension magnitude and sign has now emerged. Any physical phenomena which modifies either the interfacial potential $V[l(x)]$ (e.g., van der Waals, electrical double layer, gravitational interactions, or surface phase transitions, such as, the wetting, prewetting, or surface freezing transition) or the local atomic structure at a three-phase contact line will influence the line tension associated with this contact line. In this review we have mainly discussed the influence of the atomic, van der Waals, and gravitational interactions of *uncharged fluids* upon the line tension either near or far from a wetting transition, or, near a bulk critical point. Ions in solution are predicted to influence the line tension at three-phase contact lines [153–155]. Matsubara, Takiue, and Aratono and coworkers [123–125,156] have extensively studied the influence of cationic surfactants on the line tension for n-alkane oil droplets at an aqueous-air surface. They investigated the influence of numerous parameters including surfactant concentration and chain length, n-alkane chain length, temperature, and the presence of surface freezing on the line tension, as summarized in a recent review [106].

A profitable area of continuing theoretical and experimental study would be to obtain a better understanding of τ_{atom}, as only one experiment [85] has quantitatively explored atomic scale contributions to the line tension. Lineactants [157], or line active molecules which preferentially adsorb at a contact line, are expected to form another profitable area for future research. Lineactants are the 1D analog of surfactants; surfactants preferentially adsorb at the surface between two bulk phases and decrease the associated surface tension. Lineactants have primarily been studied at the perimeter of 2D monolayer structures at surfaces [157–159] (Fig. 1e), which possess a "2D line tension". The influence of lineactants upon the line tension at a three-phase contact line has been examined theoretically [160] but, as yet, there are no experiments. Lineactants are expected to decrease the line tension.

The interrelationship between a negative line tension and the stability of a three-phase contact line was discussed in Secs. 3.2.2 and 3.2.3. A negative line tension causes a three-phase contact line to become unstable only for sufficiently small spreading coefficient S. In Sec. 3.2.2 the contact line was unstable for $S = -5.6 \times 10^{-4}$ mN/m, $\sigma_{OW} = 45$ mN/m [corresponding to $\theta_\infty \sim 0.3°$, Eq. (5b)], and $\tau \sim -55$ pN. Larger contact angle droplets ($\theta_\infty > 5°$) may be stable even for negative line tension, as observed in Sec. 3.2.1. The interrelationship between a negative line tension τ, spreading coefficient S, and the onset of a three-phase contact line instability is incompletely understood, at least from an experimental perspective; additional experiments examining this issue would be a profitable area for future research. The phenomenological theory of Clarke [40,41] should provide guidance for how sinusoidal perturbations of the three-phase contact line induce contact line instabilities when the line tension is negative (Sec. 3.2.3).

Acknowledgements

BML thanks colleagues at the University of Kyushu in Fukuoka, Japan and the Institute for Basic Science (IBS) in Ulsan, Korea for their kind hospitality and financial support during the writing of this review. Numerous discussions with colleagues and collaborators have assisted in the clarification of these ideas.

References

[1] D.J. Benvegnu, H.M. McConnell, Line tension between liquid domains in lipid monolayers, J. Phys. Chem. 96 (1992) 6820.
[2] M. Iwamoto, O.-Y. Zhong-can, Shape deformation and circle instability in two-dimensional lipid domains by dipolar force: a shape- and size-dependent line tension model, Phys. Rev. Lett. 93 (2004) 206101.
[3] C. Bauer, S. Dietrich, Shapes, contact angles, and line tensions of droplets on cylinders, Phys. Rev. E 62 (2000) 2428.
[4] R. Aveyard, J.H. Clint, D. Nees, V. Paunov, Size-dependent lens angles for small oil lenses on water, Coll. Surf A 146 (1999) 95.
[5] B. Widom, Line tension and the shape of a sessile drop, J. Phys. Chem. 99 (1995) 2803.
[6] T. Pompe, S. Herminghaus, Three-phase contact line energetics from nanoscale liquid surface topographies, Phys. Rev. Lett. 85 (2000) 1930.
[7] J. Buehrle, S. Herminghaus, F. Mugele, Impact of line tension on the equilibrium shape of liquid droplets on patterned substrates, Langmuir 18 (2002) 9771.
[8] J.O. Indekeu, Line tension at wetting, Int. J. Mod. Phys. B 8 (1994) 309.
[9] J.Y. Wang, S. Betelu, B.M. Law, Line tension effects near first-order wetting transitions, Phys. Rev. Lett. 83 (1999) 3677.
[10] J. Wang, S. Betelu, B.M. Law, Line tension approaching a first-order wetting transition: Experimental results from contact angle measurements, Phys. Rev. E 63 (2001) 031601.
[11] T. Pompe, Line tension behavior of a first-order wetting system, Phys. Rev. Lett. 89 (2002) 076102.
[12] S.K. Das, K. Binder, Simulation of binary fluids exposed to selectively adsorbing walls: a method to estimate contact angles and line tensions, Mol. Phys. 109 (2010) 1043.
[13] B.M. Law, Theory of nucleated wetting, Phys. Rev. Lett. 72 (1994) 1698.
[14] U. Retter, K. Siegler, D. Vollhardt, Determination of the nucleus-to-surroundings interfacial tensions and the line tension of lenticular nuclei formed from insoluble monolayers at the air-water interface, Langmuir 12 (1996) 3976.
[15] B. Lefevre, A. Saugey, J.L. Barrat, L. Bocquet, E. Charlaix, P.F. Gobin, G. Vigier, Intrusion and extrusion of water in hydrophobic mesopores, J. Chem. Phys 120 (2004) 4927.
[16] S. Sharma, P.G. Debenedetti, Evaporation rate of water in hydrophobic confinement, Proc. Natl. Acad. Sci. USA 109 (2012) 4365.
[17] P.M. Winkler, R.L. McGraw, P.S. Bauer, C. Rentenberger, P.E. Wagner, Direct Determination of three-phase contact line properties on nearly molecular scale, Sci. Rep. 6 (2016) 26111.
[18] J. Zhang, F. Leroy, F. Muller-Plathe, Influence of contact-line curvature on the evaporation of nanodroplets from solid substrates, Phys. Rev. Lett. 113 (2014) 046101.
[19] H. Fan, Liquid droplet spreading with line tension effect, J. Phys.: Condens. Matter 18 (2006) 4481.
[20] S. Mechkov, A.M. Cazabat, G. Oshanin, Post-Tanner stages of droplet spreading: the energy balance approach revisited, J. Phys.: Condens. Matter 21 (2009) 464131.
[21] A. Dussaud, M. Vignes-Adler, Wetting transition of n-alkanes on concentrated aqueous salt solutions. Line tension effect, Langmuir 13 (1997) 581.
[22] G. Paneru, B.M. Law, K. Ibi, B. Ushijima, B.N. Flanders, M. Aratono, H. Matsubara, Liquid droplet coalescence and fragmentation at the aqueous-air surface, Langmuir 31 (2015) 132.
[23] J.A. de Feijter, W.G.M. Agterof II., Smallest stable radius of a circular liquid film, J. Electroanal. Chem. 37 (1972) 39.
[24] I.B. Ivanov, A.S. Dimitrov, A.D. Nikolov, N.D. Denkov, P.A. Kralchevsky, Contact angle, film, and line tension of foam films. I. Stationary and dynamic contact angle measurements, J. Colloid Interface Sci. 151 (1992) 446.
[25] A.S. Aronson, V. Bergeron, M.E. Fagan, C.J. Radke, The influence of disjoining pressure on foam stability and flow in porous media, Coll. Surf A 83 (1994) 109.
[26] R. Rosso, E.G. Virga, Sign of line tension in liquid bridge stability, Phys. Rev. E 70 (2004) 031603.
[27] M. Brinkmann, J. Kierfeld, R. Lipowsky, Stability of liquid channels or filaments in the presence of line tension, J. Phys.: Condens. Matter 17 (2005) 2349.
[28] D. Li, D.J. Steigmann, Positive line tension as a requirement of stable equilibrium, Colloids Surf. A 116 (1996) 25.
[29] L. Guzzardi, R. Rosso, E.G. Virga, Residual stability of sessile droplets with negative line tension, Phys. Rev. E 73 (2006) 021602.
[30] L. Guillemot, T. Biben, A. Galarneau, G. Vigier, E. Charlaix, Activated drying in hydrophobic nanopores and the line tension of water, Proc. Natl. Acad. Sci. USA 109 (2012) 19557.
[31] F. Bresme, H. Lehle, M. Oettel, Solvent-mediated interactions between nanoparticles at fluid interfaces, J. Chem. Phys 130 (2009) 214711.
[32] H.S. Wi, S. Cingarapu, K. Klabunde, B.M. Law, Nanoparticle adsorption at liquid-vapor surfaces: influence of nanoparticle thermodynamics, wettability and line tension, Langmuir 27 (2011) 9979.
[33] A. Scheludko, B.V. Toshev, D.T. Bojadjiev, Attachment of particles to a liquid surface (capillary theory of flotation), J. Chem. Soc. Faraday Trans. I (72) (1976) 2815.
[34] I.B. Ivanov, P.A. Kralchevsky, A.D. Nikolov, Film and line tension effects on the attachment of particles to an interface, J. Colloid Interface Sci. 112 (1986) 97.
[35] A.W. Adamson, Physical Chemistry of Surfaces, 4th ed., Wiley, New York, 1982.
[36] J. Drelich, The significance and magnitude of the line tension in three-phase (solid-liquid-fluid) systems, Colloids Surf. A 116 (1996) 43.
[37] F. Bresme, M. Oettel, Nanoparticles at fluid interfaces, J. Phys.: Condens. Matter 19 (2007) 413101.
[38] R. David, A.W. Neumann, Empirical equation to account for the length dependence of line tension, Langmuir 23 (2007) 11999.
[39] J. W. Gibbs, The Scientific Papers of J. Willard Gibbs, Vol. 1, Ox Bow Press, Connecticut, 1961.
[40] A.S. Clarke, Thermal fluctuations of a three phase contact line. I. Two fluid phases and one solid phase, J. Chem. Phys. 96 (1992) 9073.
[41] A.S. Clarke, Thermal fluctuations of a three phase contact line. II. Three fluid phases, J. Chem. Phys. 96 (1992) 9078.
[42] D.J. Steigmann, D.Q. Li, Energy-minimizing states of capillary systems with bulk, surface, and line phases, IMA J. Appl. Math. 55 (1995) 1.
[43] H. Dobbs, The elasticity of a contact line, Phys. A 271 (1999) 36.
[44] A.E. van Giessen, D.J. Bukman, B. Widom, Test of the stability of a three-phase contact line with negative line tension, Mol. Phys. 96 (1999) 1335.
[45] V.G. Babak, Line tension in thin liquid films and layer thermodynamics, Rev. Chem. Eng. 15 (1999) 157.
[46] A.I. Rusanov, Classification of line tension, Coll. Surf A 156 (1999) 315.
[47] A. Amirfazli, A.W. Neumann, Status of the three-phase line tension: a review, Adv. Colloid Interface Sci. 110 (2004) 121.
[48] A.I. Rusanov, Surface thermodynamics revisited, Surf. Sci. Rep. 58 (2005) 111.
[49] B.V. Toshev, Thermodynamic theory of thin liquid films including line tension effects, Curr. Opinion Colloid Interface Sci. 13 (2008) 100.
[50] P.-G. de Gennes, F. Brochard-Wyart, D. Quere, Capillarity and Wetting Phenomena, Springer, New York, 2004.
[51] P.G. De Gennes, Wetting: Statics and dynamics, Rev. Mod. Phys. 57 (1985) 827.
[52] J.A. de Feijter, A. Vrij, Transition regions, line tensions and contact angles in soap films. 1, J. Electroanal. Chem. Interfacial Electrochem. 37 (1972) 9.
[53] J.S. Rowlinson, B. Widom, Molecular Theory of Capillarity, Clarendon, Oxford, 1982.
[54] T. Getta, S. Dietrich, Line tension between fluid phases and a substrate, Phys. Rev. E 57 (1998) 655.
[55] W. Koch, S. Dietrich, M. Napiorkowki, Morphology and line tension of liquid-films adsorbed on chemically structured substrates, Phys. Rev. E 51 (1995) 3300.
[56] I. Ibagon, M. Bauer, S. Dietrich, Three-phase contact line and line tension of electrolyte solutions in contact with charged substrates, J. Phys.: Condens. Matter 28 (2016) 244015.
[57] F. Bresme, N. Quirke, Computer simulation study of the wetting behavior and line tensions of nanometer size particulates at a liquid-vapor interface, Phys. Rev. Lett. 80 (1998) 3791.

[58] F. Bresme, N. Quirke, Computer simulation of wetting and drying of spherical particulates at a liquid–vapor interface, J. Chem. Phys. 110 (1999) 3536.
[59] F. Bresme, N. Quirke, Nanoparticulates at liquid/liquid interfaces, Phys. Chem. Chem. Phys. 1 (1999) 2149.
[60] K.A. Tay, F. Bresme, Wetting properties of passivated metal nanocrystals at liquid-vapor interfaces: a computer simulation study, J. Am. Chem. Soc. 128 (2006) 14166.
[61] J.H. Weijs, A. Marchand, B. Andreotti, D. Lohse, J.H. Snoeijer, Origin of line tension for a Lennard-Jones nanodroplet, Phys. Fluids 23 (2011) 022001.
[62] H. Peng, G.R. Birkett, A.V. Nguyen, The impact of line tension on the contact angle of nanodroplets, Mol. Simul. 40 (2014) 934.
[63] M. Schneemilch, N. Quirke, Effect of oxidation on the wettability of poly(dimethylsiloxane) surfaces, J. Chem. Phys. 127 (2007) 114701.
[64] J.T. Hirvi, T.A. Pakkanen, Molecular dynamics simulations of water droplets on polymer surfaces, J. Chem. Phys. 125 (2006) 144712.
[65] T. Werder, J.H. Walther, R.J. Jaffe, T. Halicioglu, P. Koumoutsakos, On the water-carbon interactions for use in molecular dynamics simulations of graphite and carbon nanotubes, J. Phys. Chem. B 107 (2003) 1345.
[66] R.C. Dutta, S. Khan, J.K. Singh, Wetting transition of water on graphite and boron-nitride surfaces: a molecular dynamics study, Fluid Phase Equilib. 302 (2011) 310.
[67] R. Ramirez, J.K. Singh, F. Muller-Plathe, M.C. Bohm, Ice and water droplets on graphite: a comparison of quantum and classical simulations, J. Chem. Phys. 141 (2014) 204701.
[68] Y. Djikaev, Histogram analysis as a method for determining the line tension of a three-phase contact region by Monte Carlo simulations, J. Chem. Phys. 123 (2005) 184704.
[69] B.J. Block, S. Kim, P. Virnau, K. Binder, Anisotropic interfacial tension, contact angles, and line tensions: a graphics-processing-unit-based Monte Carlo study of the Ising model, Phys. Rev. E 90 (2014) 062106.
[70] J.N. Israelachvili, Intermolecular and Surface Forces, 3rd ed., Academic Press, London, 2011.
[71] I.E. Dzyaloshinskii, E.M. Lifshitz, L.P. Pitaevskii, The general theory of van der Waals forces, Adv. Phys. 10 (1961) 165.
[72] D.B. Hough, L.R. White, The calculation of Hamaker constants from Lifshitz theory with application to wetting phenomena, Adv. Colloid Interface Sci. 14 (1980) 3.
[73] H.E. Stanley, Introduction to Phase Transitions and Critical Phenomena, Oxford University Press, New York, 1971.
[74] I.M. Tidswell, T.A. Rabedeau, P.S. Pershan, S.D. Kosowsky, Complete wetting of a rough surface: an X-ray study, Phys. Rev. Lett. 66 (1991) 2108.
[75] I.M. Tidswell, T.A. Rabedeau, P.S. Pershan, J.P. Folkers, M.V. Baker, G.M. Whitesides, Wetting films on chemically modified surfaces: an X-ray study, Phys. Rev. B 44 (1991) 10869.
[76] D. Beaglehole, E.Z. Radlinska, B.W. Ninham, H.K. Christenson, Inadequacy of Lifshitz theory for thin liquid-films, Phys. Rev. Lett. 66 (1991) 2084.
[77] E. Cheng, M.W. Cole, W.F. Saam, J. Treiner, Helium prewetting and nonwetting on weak-binding substrates, Phys. Rev. Lett. 67 (1991) 1007.
[78] J.E. Rutledge, P. Taborek, Prewetting phase diagram for ^{4}He on Cesium, Phys. Rev. Lett. 69 (1992) 937.
[79] H. Kellay, D. Bonn, J. Meunier, Prewetting in a binary liquid mixture, Phys. Rev. Lett. 71 (1993) 2607.
[80] W.A. Zisman, in Contact angle, wettability and adhesion, in: R.F. Gould (Ed.), American Chemical Society, Washington, D. C., 1964, pp. 1–51.
[81] B.M. Law, A. Mukhopadhyay, J.R. Henderson, J.Y. Wang, Wetting of silicon wafers by n-alkanes, Langmuir 19 (2003) 8380.
[82] K. Ragil, J. Meunier, D. Broseta, J.O. Indekeu, D. Bonn, Experimental observation of critical wetting, Phys. Rev. Lett. 77 (1996) 1532.
[83] J.O. Indekeu, Line tension near the wetting transition: results from an interface displacement model, Physica (Amsterdam) 183A (1992) 439.
[84] H. Dobbs, Line tension of n-alkanes on water from a Cahn-type theory, Langmuir 15 (1999) 2586.
[85] S.P. McBride, B.M. Law, Influence of line tension on spherical colloidal particles at liquid-vapor interfaces, Phys. Rev. Lett. 109 (2012) 196101.
[86] R. Aveyard, J.H. Clint, Particle wettability and line tension, J. Chem. Soc. Faraday Trans. 92 (1996) 85.
[87] R. Aveyard, B.D. Beake, J.H. Clint, Wettability of spherical particles at liquid surfaces, J. Chem. Soc. Faraday Trans. 92 (1996) 4271.
[88] J. Mingins, A. Scheludko, Attachment of spherical particles to the surface of a pendant drop and the tension of the wetting parameter, J. Chem. Soc. Faraday Trans. 75 (1979) 1.
[89] J. Aveyard, J.H. Clint, New method for the measurement of line tensions at the solid/liquid/air three-phase contact line, J. Chem. Soc. Faraday Trans. 91 (1995) 175.
[90] N.I.D. Fenwick, F. Bresme, N. Quirke, Computer simulation of a Langmuir trough experiment carried out on a nanoparticulate array, J. Chem. Phys. 114 (2001) 7274.
[91] C. Powell, N. Fenwick, F. Bresme, N. Quirke, Wetting of nanoparticles and nanoparticle arrays, Colloids Surf. A 206 (2002) 241.
[92] R. Aveyard, J.H. Clint, D. Nees, Small solid particles and liquid lenses at fluid/fluid interfaces, Colloid Polym. Sci. 278 (2000) 155.
[93] D.O. Grigoriev, J. Krägel, V. Dutschk, R. Miller, H. Möhwald, Contact angle determination of micro- and nanoparticles at fluid/fluid interfaces: the excluded area concept, Phys. Chem. Chem. Phys. 9 (2007) 6447.
[94] A. Maestro, E. Guzmán, F. Ortega, R.G. Rubio, Contact angle of micro- and nanoparticles at fluid interfaces, Curr. Opinion Colloid Interface Sci. 19 (2014) 355.
[95] M. Zanini, L. Isa, Particle contact angles at fluid interfaces: pushing the boundary beyond hard uniform spherical colloids, J. Phys.: Condens. Matter 28 (2016) 313002.
[96] J. Reguera, E. Ponomarev, T. Gaue, F. Stellaci, F. Bresme, M. Moglianetti, Contact angle and adsorption energies of nanoparticles at the air-liquid interface determined by neutron reflectivity and molecular dynamics, Nanoscale 7 (2015) 5665.
[97] V.N. Paunov, Novel method for determining the three-phase contact angle of colloid particles adsorbed at air-water and oil-water interfaces, Langmuir 19 (2003) 7970.
[98] L.N. Arnaudov, O.J. Cayre, M.A. Cohen Stuart, S.D. Stoyanov, V.N. Paunov, Measuring the three-phase contact angle of nanoparticles at fluid interfaces, Phys. Chem. Chem. Phys. 12 (2010) 328.
[99] A. Maestro, L.J. Bonales, H. Ritacco, R.G. Rubio, F. Ortega, Effect of the spreading solvent on the three-phase contact angle of microparticles attached at fluid interfaces, Phys. Chem. Chem. Phys. 12 (2010) 14115.
[100] L. Isa, F. Lucas, R. Wepf, E. Reimhult, Measuring single-nanoparticle wetting properties by freeze-fracture shadow-casting cryo-scanning electron microscopy, Nat. Commun. 2 (2011) 438.
[101] B.P. Binks, L. Isa, A.T. Tyowua, Direct measurement of contact angles of silica particles in relation to double inversion of pickering emulsions, Langmuir 29 (2013) 4923.
[102] C. Stefaniu, M. Chanana, H. Ahrens, D.Y. Wang, G. Brezesinski, H. Mohwald, Conformational induced behaviour of copolymer-capped magnetite nanoparticles at the air/water interface, Soft Matter 7 (2011) 4267.
[103] D.C.E. Calzolari, D. Pontoni, M. Deutsch, H. Reichert, J. Daillant, Nanoscale structure of surfactant-induced nanoparticle monolayers at the oil-water interface, Soft Matter 8 (2012) 11478.
[104] L. Isa, D.C.E. Calzolari, D. Pontoni, T. Gillich, A. Nelson, R. Zirbs, A. Sanchez-Ferrer, R. Mezzenga, E. Reimhult, Core-shell nanoparticle monolayers at planar liquid-liquid interfaces: effects of polymer architecture on the interface microstructure, Soft Matter 9 (2013) 3789.
[105] I. Prigogine, J. Marechal, The influence of differences in molecular size on the surface tension of solutions. IV, J. Colloid Sci. 7 (1952) 122.
[106] H. Matsubara, B. Ushijima, B.M. Law, T. Takiue, M. Aratono, Line tension of alkane lenses on aqueous surfactant solutions at phase transitions of coexisting interfaces, Adv. Colloid Interface Sci. 206 (2014) 186.
[107] K. Du, J.A. Liddle, A.J. Berglund, Three-dimensional real-time tracking of nanoparticles at an oil-water interface, Langmuir 28 (2012) 9181.
[108] A.I. Rusanov, A.K. Shchekin, D.V. Tatyanenko, The line tension and the generalized Young equation: the choice of dividing surface, Colloid Surf. A 250 (2004) 263.
[109] L. Schimmele, M. Napiorkowki, S. Dietrich, Conceptual aspects of line tension, J. Chem. Phys. 127 (2007) 164715.
[110] J.M.D. Lane, G.S. Grest, Spontaneous asymmetry of coated spherical nanoparticles in solution and at liquid-vapor interfaces, Phys. Rev. Lett. 104 (2010) 235501.

[111] N.N. Poddar, J.G. Amar, Adsorption and diffusion of colloidal Au nanoparticles at a liquid-vapor interface, J. Chem. Phys. 140 (2014) 244702.
[112] J. Faraudo, F. Bresme, Stability of particles adsorbed at liquid-fluid interfaces: Shape effects induced by line tension, J. Chem. Phys. 118 (2003) 6518.
[113] J. Faraudo, F. Bresme, Interplay between thermodynamics and geometry in the adsorption of non-spherical nanoparticles at liquid/liquid interfaces, J. Non-equilib. Thermodyn. 29 (2004) 397.
[114] F. Bresme, J. Faraudo, Orientational transitions of anisotropic nanoparticles at liquid–liquid interfaces, J. Phys.: Condens. Matter 19 (2007) 375110.
[115] S. Coertjens, P. Moldenaers, J. Vermant, L. Isa, Contact angles of microellipsoids at fluid interfaces, Langmuir 30 (2014) 4289.
[116] B.P. Binks, S.O. Lumsdon, Influence of particle wettability on the type and stability of surfactant-free emulsions, Langmuir 16 (2000) 8622.
[117] H. Matsubara, N. Ikeda, T. Takiue, M. Aratono, C.D. Bain, Interfacial films and wetting behavior of hexadecane on aqueous solutions of dodecyltrimethylammonium bromide, Langmuir 19 (2003) 2249.
[118] B.A. Pethica, Rep. Prog. Appl. Chem. 46 (1961) 14.
[119] B.A. Pethica, The contact angle equilibrium, J. Colloid Interface Sci. 62 (1977) 567.
[120] J.K. Berg, C.M. Weber, H. Riegler, Impact of negative line tension on the shape of nanometer-size sessile droplets, Phys. Rev. Lett. 105 (2010) 076103.
[121] A. Amirfazli, S. Haenig, A. Mueller, A.W. Neumann, Measurements of line tension for solid-liquid-vapor systems using drop size dependence of contact angles and its correlation with solid-liquid interfacial tension, Langmuir 16 (2000) 2024.
[122] L. Boruvka, A.W. Neumann, Generalization of the classical theory of capillarity, J. Chem. Phys. 66 (1977) 5464.
[123] Y. Takata, H. Matsubara, Y. Kikuchi, N. Ikeda, T. Matsuda, T. Takiue, M. Aratono, Line tension and wetting behavior of an air/hexadecane/aqueous surfactant system, Langmuir 21 (2005) 8594.
[124] Y. Takata, H. Matsubara, T. Matsuda, Y. Kikuchi, T. Takiue, B. Law, M. Aratono, Study on line tension of air/hexadecane/aqueous surfactant system, Colloid Polym. Sci. 286 (2008) 647.
[125] Y. Ushijima, B. Ushijima, E. Ohtomi, Y. Takata, T. Takiue, M. Aratono, H. Matsubara, Line tension at freezing transition of alkane wetting film on aqueous surfactant solutions, Colloids Surf. A 33 (2011) 390.
[126] X.Z. Wu, B.M. Ocko, E.B. Sirota, S.K. Sinha, M. Deutsch, B.H. Cao, M.W. Kim, Surface tension measurements of surface freezing in liquid normal alkanes, Science 261 (1993) 1018.
[127] K.P. Browne, D.A. Walker, K.J.M. Bishop, B.A. Grzybowski, Self-division of microscopic droplets: partitioning of nanosized cargo into nanoscale micelles, Angew. Chem. Int. Ed. 49 (2010) 6756.
[128] F. Bresme, N. Quirke, Computer simulation studies of liquid lenses at a liquid-liquid interface, J. Chem. Phys. 112 (2000) 5985.
[129] A. Vrij, Possible mechanism for the spontaneous rupture of thin, free liquid films, Discuss. Faraday Soc. 42 (1966) 23.
[130] A. Vrij, J.T.G. Overbeek, Rupture of thin liquid films due to spontaneous fluctuations in thickness, J. Am. Chem. Soc. 20 (1968) 3074.
[131] H.K. Pak, B.M. Law, Dynamic scaling of wetting layer growth, Europhys. Lett. 31 (1995) 19.
[132] B.M. Law, Nucleated wetting films: the late-time behavior, Phys. Rev. E 50 (1994) 2827.
[133] B.M. Law, Nucleated wetting layers, Phys. Rev. Lett. 69 (1992) 1781.
[134] E.M. Blokhuis, Nucleation of wetting layers, Phys. Rev. E 51 (1995) 4642.
[135] E.M. Blokhuis, B. Widom, Wetting, Curr. Opinion Colloid Interface Sci. 1 (1996) 424.
[136] B.M. Law, H.K. Pak, Influence of hydrodynamic flow on nucleated wetting, J. Chem. Phys. 106 (1997) 301.
[137] R. Bausch, R. Blossey, Critical droplets on a wall near a first-order wetting transition, Phys. Rev. E 48 (1993) 1131.
[138] R. Blossey, R. Bausch, Dynamics of first-order wetting transitions, Phase Transitions 50 (1994) 113.
[139] R. Blossey, Nucleation at first-order wetting transitions, Int. J. Mod. Phys. B 9 (1995) 3489.
[140] R. Bausch, R. Blossey, G. Floltin, Decay of metastable state in wetting and dewetting transitions, Phys. A 224 (1996) 93.
[141] A.I. Hienola, P.M. Winkler, P.E. Wagner, H. Vehkamaki, A. Lauri, I. Napari, M. Kulmala, Estimation of line tension and contact angle from heterogeneous nucleation experimental data, J. Chem. Phys. 126 (2007) 094705.
[142] D. Li, A.W. Neumann, Determination of line tension from the drop size dependence of contact angles, Colloid Surf. 43 (1990) 195.
[143] D. Duncan, D. Li, J. Gaydos, A.W. Neumann, Correlation of line tension and solid-liquid interfacial tension from the measurement of drop size dependence of contact angles, J. Colloid Interface Sci. 169 (1995) 256.
[144] A. Amirfazli, D. Chatain, A.W. Neumann, Drop size dependence of contact angles for liquid tin on silica surface: line tension and its correlation with solid-liquid interfacial tension, Colloid Surface A 142 (1998) 183.
[145] A. Amirfazli, D.Y. Kwok, J. Gaydos, A.W. Neumann, Line tension measurements through drop size dependence of contact angle, J. Colloid Interface Sci. 205 (1998) 1.
[146] A. Amirfazli, A. Keshavarz, L. Zhang, A.W. Neumann, Determination of line tension for systems near wetting, J. Colloid Interface Sci. 265 (2003) 152.
[147] J. Drelich, J.D. Miller, The line/pseudo-line tension in three-phase systems, Particulate Sci. Technol. 10 (1992) 1.
[148] J. Drelich, J.D. Miller, J. Hupka, The effect of drop size on contact angle over a wide range of drop volumes, J. Colloid Interface Sci. 155 (1993) 379.
[149] H.T. Dobbs, J.O. Indekeu, Line tension at wetting: interface displacement model beyond the gradient-squared approximation, Phys. A 201 (1993) 457.
[150] S. Herminghaus, F. Brochard, Dewetting through nucleation, C. R. Phys. 7 (2006) 1073.
[151] S. Herminghaus, F. Brochard, Erratum to the article, Dewetting through nucleation, C. R. Phys. 8 (2007) 86 [C. R. Phys. 7 (9–10) (2006) 1073–1081].
[152] B. Shapiro, H. Moon, R.L. Garrell, C.-J. Kim, Equilibrium behavior of sessile drops under surface tension, applied external fields, and material variations, J. Appl. Phys. 93 (2003) 5794.
[153] T. Chou, Geometry-dependent electrostatics near contact lines, Phys. Rev. Lett. 87 (2001) 106101.
[154] K.H. Kang, I.S. Kang, C.M. Lee, Electrostatic contribution to line tension in a wedge-shaped contact region, Langmuir 19 (2003) 9334.
[155] A. Doerr, S. Hardt, Line tension and reduction of apparent contact angle associated with electric double layers, Phys. Fluids 26 (2014) 082105.
[156] H. Matsubara, Y. Ikebe, Y. Ushijima, Y. Takata, T. Takiue, M. Aratono, First-order wetting transition and line tension of hexadecane lens at air/water interface assisted by surfactant adsorption, Bull. Chem. Soc. Jpn. 83 (2010) 1198.
[157] S. Trabelsi, S. Zhang, T.R. Lee, D.K. Schwartz, Lineactants: Surfactant analogues in two dimensions, Phys. Rev. Lett. 100 (2008) 037802.
[158] C. Bernardini, S.D. Stoyanov, L.N. Arnaudov, M.A. Cohen Stuart, Colloids in Flatland: a perspective on 2D phase-separated systems, characterisation methods, and lineactant design, Chem. Soc. Rev. 42 (2013) 2100.
[159] B. Palmieri, M. Grant, S.A. Safran, Prediction of the dependence of the line tension on the composition of linactants and the temperature in phase separated membranes, Langmuir 30 (2014) 11734.
[160] B. Widom, Adsorption at a line of three-phase contact, Colloid Surf. A 239 (2004) 141.